Human Engineered Heart Tissues as an In Vitro Model of Duchenne Muscular Dystrophy

Samantha Bremner

A dissertation

submitted in partial fulfillment of the

requirements for the degree of

Doctor of Philosophy

University of Washington

2022

Reading Committee:

Nathan J Sniadecki, Co-chair

David L Mack, Co-chair

Michael Regnier

Program Authorized to Offer Degree:

Bioengineering

University of Washington

Abstract

Human Engineered Heart Tissues as an In Vitro Model of Duchenne Muscular Dystrophy

Samantha Bremner

Chairs of the supervisory committee:

Nathan J Sniadecki

Mechanical Engineering

David L Mack

Rehabilitation Medicine

Cardiomyopathy is the leading cause of death for patients with Duchenne muscular dystrophy (DMD), a severe, degenerative muscular disorder. This disease results from the lack of functional dystrophin, a protein that localizes to the plasma membrane of cardiomyocytes to form a mechanically strong link between the extracellular matrix and the intracellular cytoskeleton, and its absence has detrimental effects on contractile, calcium, and metabolic regulation. The development of novel treatments for DMD has been hampered by the shortcomings of commonly used animal models to replicate all aspects of the disease, prompting the need for human in vitro models of dystrophic cardiomyopathy for preclinical studies. To date, human induced pluripotent

stem cell-derived cardiomyocytes (hiPSC-CMs) have been an invaluable source with which to study DMD, as they have been shown to replicate many relevant disease phenotypes. However, the utility of hiPSC-CMs is limited by their relative immaturity and the biological irrelevance of traditional two-dimensional cell culture. To address these shortcomings, we have developed engineered heart tissues (EHTs) from dystrophic hiPSC-CMs as an in vitro, preclinical model of DMD. This EHT model better mimics the native cardiac microenvironment, providing extracellular matrix cues of a relevant stiffness, cell-cell communication, and uniaxial force development promoting proper cellular alignment and hypertrophy. We have shown that dystrophic EHTs present relevant functional deficiencies, including decreased contractile performance and altered calcium transients. Additionally, we have demonstrated the ability of a miniaturized EHT platform to evaluate the efficiency and cardioprotective effect of novel microdystrophin gene therapies for DMD. Through the studies described herein, we have validated the promise of three-dimensional engineered cardiac tissues as a preclinical screening model of dystrophic cardiomyopathy.

Table of Contents

List of Figures

Acknowledgements

I would first like to thank my advisors, Dr. David Mack and Dr. Nathan Sniadecki, who took a chance on not only a new student, but a new collaboration. Thank you for your infectious enthusiasm and for giving me the support needed to grow into the scientist I am today. I will be forever grateful for your immeasurable impact on my scientific career and beyond.

I also owe many thanks to the other members of my supervisory committee, Dr. Michael Regnier, Dr. Jen Davis, and Dr. Julie Mathieu, for their significant role in my graduate experience. Thank you for your tough questions and for challenging me as a thinker and a scientist.

I have been very fortunate to be surrounded by an exceptional research community, members of which have been invaluable sources of collaboration, mentorship, and friendship. The following is an incomplete list of individuals who have had such an impact on my time here at UW: Dr. Alec Smith, Dr. Mark Bothwell, Dr. Christian Mandrycky, Dr. SiWei Luo, Saffie Mohran, Changho Chun, Dr. Shawn Luttrell, Dr. Jordan Klaiman, Elisa Clark, Alex Goldstein, Ty Higashi, Ruby Padgett, Dr. Andrea Leonard, Dr. Danny El-Nachef, Dr. Kevin Beussman, Dr. Molly Mollica, Dr. Josè Manuel Pioner, Dr. Jeffrey Chamberlain, Dr. Hichem Tasfaout, and Dr. Dale Hailey.

I would like the many undergraduate students that I have had the pleasure of working with and who have contributed to the work presented herein: Karen Gaffney, Alan Levinson, Jessica Okolo, Naveen Arunachalam, Aniruddh Saxena, and Ethan Rehn. Thank you for teaching me to be a mentor and for your excitement and enthusiasm for science, which made all of this worthwhile.

Lastly, I need to thank my friends and family for their love and support, without which none of this would have been possible.

Chapter 1. Introduction

1.1 Cardiomyopathy in Duchenne Muscular Dystrophy

Duchenne muscular dystrophy (DMD) is a severe, degenerative neuromuscular disorder affecting 1 in 3,500-5,000 males born in the United States resulting from a lack of functional dystrophin protein [1,2]. DMD patients experience progressive muscle weakness, atrophy, and fibrosis affecting the skeletal, respiratory, and cardiac muscle systems. With the advent of improved respiratory support, dilated cardiomyopathy and congestive heart failure have emerged as the leading cause of death for DMD patients [3]. Given the central role of dystrophin in stabilizing the sarcolemma of the myocyte, DMD causes myocyte fragility and contraction-induced cell damage, leading to cardiac degeneration and replacement with fibrotic tissue. At the cellular level, the lack of dystrophin has pleiotropic effects on calcium regulation [4, 5], nitric oxide regulation [6, 7], and mitochondrial function [8, 9], all of which contribute to the disease phenotype, although the mechanisms bridging the gap from cellular dysfunction to muscle wasting are not well understood.

To date, there is no cure for DMD and current standard of care relies on pharmacological intervention to decrease cardiac load [10]. More recently, there have been great efforts toward developing novel therapies. These include drugs that target membrane fragility [11], oxidative damage [12, 13], calcium channels [14], and fibrosis [47,48]. In addition to these efforts, there is significant interest in rescuing dystrophin expression, either through read-through therapy [17], exon skipping [18], or exogenous gene replacement therapy [19]. Further clinical studies are needed to fully evaluate these promising emerging therapies.

1.1.1 Duchenne muscular dystrophy

DMD is inherited as a recessive X-linked mutation in the dystrophin gene, a protein expressed in striated muscle cells Male children with DMD typically begin presenting symptoms

of muscle weakness at 3-5 years of age, eventually becoming nonambulatory around the age of 12 years [20]. While skeletal muscle degeneration may be more evident, there is also severe cardiomyopathy associated with DMD as a result of progressive cardiac muscle degeneration and fibrosis. With the advent of improved medical treatment, life expectancy has improved, and males affected by DMD live on average into their mid to late twenties.

The lack of dystrophin causes a loss of muscle cell membrane integrity, eventually resulting in cell death and gradual muscle weakening. There are a variety of disease-causing mutations that result in the lack of dystrophin or the expression of a truncated dystrophin. As such, there is significant variation in the severity and progression of the disease as a result of different mutations, ranging from less severe conditions known as Becker muscular dystrophy (BMD) to the most severe cases of DMD [21]. It is worth noting that different dystrophin mutations often yield different presentations of cardiomyopathy, and that there has been no correlation found between the severity and progression of skeletal myopathy and the degree and onset of cardiomyopathy in DMD patients [22].

Beyond skeletal muscle, the heart is also severely affected by the lack of functional dystrophin. Those affected with DMD typically exhibit an onset of cardiomyopathy at age 16-18 [20]. The incidence of cardiomyopathy increases with age, and it has been predicted that 25% of males aged 6 years have some degree of cardiomyopathy, and this incidence increases to 90% by 18 years of age [23]. Historically, DMD began with the loss of ambulation and resulted in death early in the second decade of life, most often due to respiratory failure. However, with the improvement of ventilation therapies, spinal stabilization, and treatments for muscle weakness, the life expectancy of DMD has risen, and cardiomyopathy has emerged as the leading cause of death [6,7].

1.1.2 Clinical presentation of cardiomyopathy

Symptoms of Duchenne muscular dystrophy first appear in early childhood, predominantly as progressive muscle weakness, eventually leading to muscle atrophy [2]. The increased amount of muscle damage occurring in DMD can be detected as exceedingly high levels of creatine kinase in the blood, an enzyme that is released upon the death of muscle cells [24]. A more definitive diagnosis requires either a muscle biopsy proving the lack of functional dystrophin or genetic testing to determine the specific mutation.

While skeletal muscle abnormalities are often the first visible symptom of DMD, cardiac disease becomes a prominent symptom for most DMD patients within their first decade of life. Broadly, the progression of DMD-cardiomyopathy first presents as diastolic dysfunction, fibrosis in the left ventricular wall, and ECG abnormalities. Gradually, as cardiac damage continues, the fibrosis accumulates, causing left ventricular systolic dysfunction and dilation [25]. This dilation continues until dilated cardiomyopathy and eventual end-stage heart failure occurs.

Once a child is diagnosed, it is recommended that they receive cardiac screening at the time of diagnosis and from then on every two years until ten years of age, at which point yearly screening is recommended [10]. The most common techniques used to assess cardiac function in patients with DMD are electrocardiography (ECG) and echocardiography. However, it is worth noting that diagnosis cardiomyopathy is DMD patients can be challenging due to respiratory problems, scoliosis, lack of physical activity, and deformation of the chest wall that complicate these procedures [21]. These challenges may limit the diagnostic accuracy of these techniques.

The left ventricular fibrosis associated with DMD impairs the electrical conductivity of the heart, and as a result, most patients with DMD present abnormal EGC tracings. Characteristic DMD-related EGC patterns include tall R waves and increased R/S amplitudes in lead VI, short PR interval, right axis deviation, and deep Q waves [26]. More broadly, DMD patients have higher heart rates than other types of muscular dystrophies [27]. ECG tracings also often yield evidence

of arrhythmia, a common event in patients with DMD due to the fibrotic myocardium. Specific forms of arrhythmia that are often seen are sinus tachycardia, atrial fibrillation, atrial flutter, and atrial and ventricular tachycardia [26]. As diffuse fibrosis is the first stage of DMD-cardiomyopathy, ECG abnormalities are often detectable before echocardiographic abnormalities.

The standard imaging technique used in DMD patients is echocardiography, facilitating the assessment of heart dilation and systolic function. Most patients with DMD present with left ventricular dilation, wall movement abnormalities, and impaired systolic function, resulting in low ejection fraction values [25]. While echocardiography is often a relatively simple and low-cost cardiac imaging modality, it can be difficult to perform on DMD patients due to physical deficiencies, as previously discussed. To circumvent this issue and achieve more accurate results, some have turned to cardiac magnetic resonance [28]. Despite the increased accuracy in assessing ventricular size and function, cardiac magnetic resonance has some drawbacks, specifically that it is more expensive, less widely accessible, and young children often require sedation, making this imaging technique more applicable to older patients.

1.1.3 The role of dystrophin and the dystroglycan complex

The dystrophin gene (*dmd*) is the largest gene in the human genome, spanning 2.5 Mb on chromosome Xp21.1 [29]. The gene contains 79 exons, and the produced transcript reaches 14 kb in length. The encoded protein is comparably large, weighing 427 kDa [30]. Dp427m is the full-length isoform expressed in skeletal and cardiac muscle, while other isoforms are expressed in the brain and Purkinje cells [31]. Dystrophin is a long, rod-shaped protein containing spectrin repeats with interspaced hinge regions that localizes to the sarcolemma (**Fig. 1.1**) [32]. As part of the dystroglycan complex (DGC), dystrophin is tasked with connecting the sarcolemma to the cytoskeleton. This is accomplished through connections to sarcolemma-bound glycoproteins at the C-terminus of dystrophin and to actin fibers at the N-terminus [33].

The DGC, also known as the dystrophin-associated protein complex, contains sarcoplasmic membrane proteins, as well as transmembrane and extracellular proteins in addition to dystrophin (**Fig. 1.1**). The DGC localizes to sarcomeric z-disks and adhesive costamere complexes in the myocyte. Most notably, the DGC provides a strong connection between the extracellular matrix and the intracellular cytoskeleton [34]. Through this connection, the DGC stabilizes the sarcolemma, allowing for the accumulation of ion gradients necessary for proper excitation-contraction coupling. The DGC also utilizes dystrophin as a shock absorber, protecting the sarcolemma from stress due to cell contraction. DGC dysfunction causes a loss of sarcolemmal integrity, making the muscle cell more susceptible to damage. Consequently, mutations in other components of the DGC can cause symptoms similar to DMD. Lastly, the DGC provides a critical hub for the recruitment of signaling proteins involved in mechanotransduction, namely nitric oxide synthase (nNOS), the importance of which will be discussed in later sections.

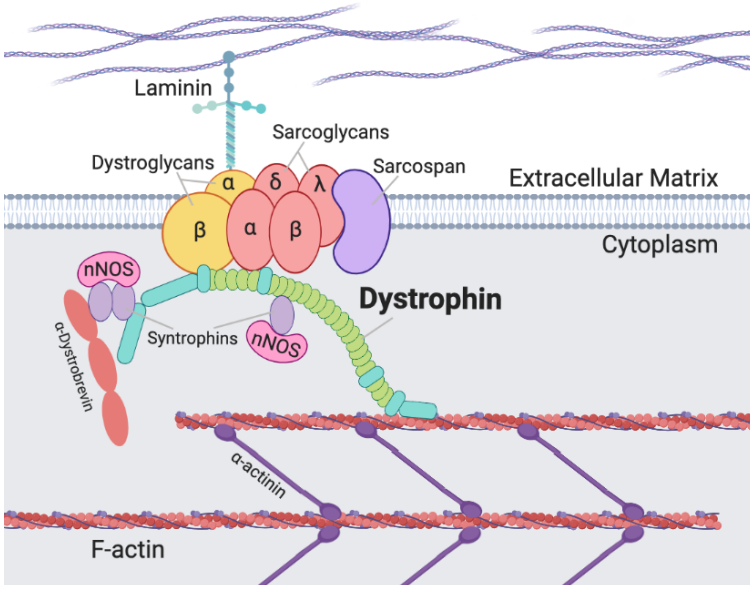

Figure 1.1. Dystrophin and the dystroglycan complex (DGC) connect the cytoskeleton to the extracellular matrix. The DGC is found at the sarcolemma, localized to z-disks, and in addition to dystrophin, contains sarcoplasmic proteins (neuronal nitric oxide synthase (nNOS), the syntrophins, and α-dystrobrevin), transmembrane proteins (sarcospan, caveolin-3, the sarcoglycans, and β-dystroglycan), and extracellular proteins (α-dystroglycan and laminin). Made with Biorender.com.

1.1.4 Molecular mechanisms of dystrophic cardiomyopathy

There is a vast complexity of molecular events that are disturbed by the lack of functional dystrophin that ultimately result in the observed cardiac pathology. At the core of this cardiomyopathy is an increase in intracellular calcium, resulting from strain-induced damage to the sarcolemma. This rise of cytosolic calcium has been shown to adversely affect a variety of downstream events, including expression and function of ion channels, membrane stability, calcium storage in the sarcoplasmic reticulum, mitochondrial function, and nitric oxide signaling (**Fig. 1.2**).

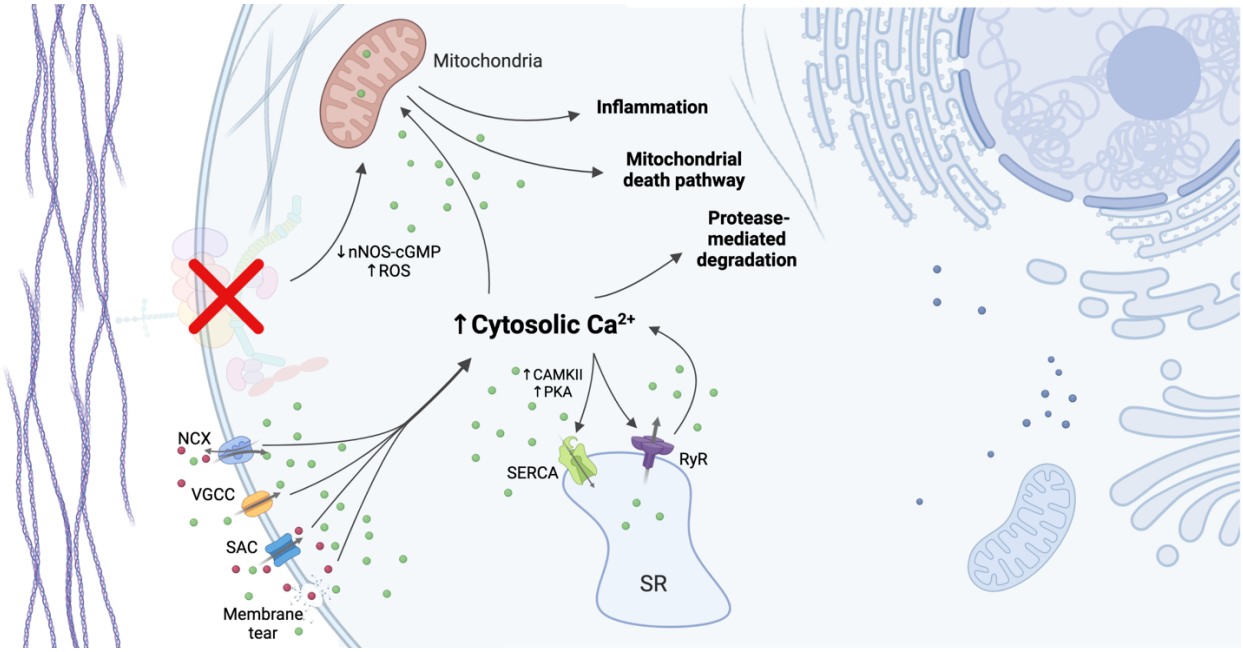

Figure 1.2. Molecular mechanisms of dystrophic cardiomyopathy. In the absence of dystrophin, the DGC is unable to properly form at the sarcolemma, resulting in membrane fragility, nitric oxide signaling (nNOS-cGMP) dysfunction, and an increase in intracellular Ca^{2+}. This is followed by mitochondrial and sarcoplasmic reticulum (SR) dysfunction, which eventually culminate in inflammation, protease-mediated degradation, and mitochondrial death pathway activation resulting in cell death and muscle wasting. Made with Biorender.com. NCX: Na+-Ca2+ exchanger; VGCC: Voltage-gated Ca2+ channels; SAC: stretched-activated channel; nNOS: neuronal nitric oxide synthase; cGMP: cyclic guanosine monophosphate; SERCA: Sarcoplasmic/endoplasmic reticulum Ca2+-ATPase; RyR: ryanodine receptor; CaMKII: calmodulin-kinase II; PKA: protein kinase A.

Increased cytosolic calcium

At the center of DMD-related cardiac pathology is an increase in intracellular calcium, the ion responsible for proper excitation-contraction coupling and various other signaling cascades in the myocyte. Despite the heart's lower calcium influx compared to skeletal muscle, cardiac cells show a greater response to this influx, suggesting more sensitive calcium-induced calcium release from the sarcoplasmic reticulum [35]. Increased cytosolic calcium causes activation of protein kinase A (PKA), calcium/Calmodulin (CaM), and CaM kinase II (CaMKII), all of which hyper-phosphorylate calcium channels on the sarcoplasmic reticulum, causing further sensitization [36]. Additionally, mitochondrial function is impaired, leading to nuclear factor-κB (NF-κB) induced inflammation and subsequent necrosis [37].

While the consequences of increased cytosolic calcium may be clear, it is less evident how this elevation initially occurs. Many studies point to membrane tears and stretch-activated channels (SACs) as the principal sources of intracellular calcium increase. Other ion channels are thought to also have an effect, namely voltage-gated calcium channels (VGCCs). This initial rise in intracellular calcium activates channels on the sarcoplasmic reticulum, further exacerbating the elevated intracellular calcium levels.

Under healthy conditions, the sarcolemma is largely impermeable to ions and proteins. As previously discussed, a significant role of dystrophin is stabilizing the sarcolemma and acting as a shock absorber to protect it from damage during cellular contraction. In dystrophic cardiomyocytes, it has been predicted that the lack of dystrophin results in tears in the sarcolemma after repeated contractions, allowing for the unregulated entry of extracellular calcium [38]. To test this hypothesis, membrane sealant poloxamer 188, a polymer known to insert into lipid bilayers and repair membrane damage, was applied to isolated *mdx* mouse cardiomyocytes [39]. When mechanically stretched, dystrophic cells treated with poloxamer 188 exhibited decreased intracellular calcium. However, there was still a relative increase in

intracellular calcium as compared to healthy cells, indicating that other mechanisms for calcium entry are likely involved as well.

Other identified points of entry for extracellular calcium have been stretch-activated channels (SACs) and voltage-gated calcium channels (VGCCs). SACs are non-specific, mechanosensitive channels found on the sarcolemma that open in response to contraction-induced stress, allowing for the entry of cations into the cardiomyocyte [40]. Under healthy conditions, SACs allow for the modulation of cardiac electrophysiology in response to varying mechanical loads. SACs have been investigated as a potential source for the initial increase in intracellular calcium. When SACs were inhibited in isolated cardiomyocytes which were subsequently exposed to a mechanical load, the rise of intracellular calcium was decreased [41]. However, given the non-specific nature of the inhibitor used, it is possible that a variety of other ion channels were blocked.

There are multiple mechanosensitive channels and subunits that make up SACs, a family of which are transient receptor potential cation (TRPC) channels. Specific TRPC channels have been investigated for their role in dystrophic cardiomyopathy, namely TRPV2, TRPC1, and TRPC6. TRPV2 is usually localized to intracellular membranes; however, when exposed to stimuli, such as insulin growth factor-1, TRPV2 will translocate to the sarcolemma. Cardiomyocytes from *mdx* mice have been shown to overexpress TRPV2, and the inhibition of these channels was shown to reduce the increase in intracellular calcium in response to osmotic stress [42]. Similarly, TRPC1 has also been found to be overexpressed in *mdx* mice [41]. TRPC1 is activated by reactive oxygen species (ROSs), the level of which is increased in DMD cells. Thus, it has been hypothesized that the overabundance of both TRPC1 and reactive oxygen species could contribute to increased intracellular calcium when subjected to mechanical loads. Lastly, the inhibition of TRPC6 channels in *mdx* mouse hearts has been shown to normalize

contractions and decrease the incidence of arrhythmias [43]. Further work is needed to evaluate the efficacy of targeting TRPC channels as a potential therapy for DMD-cardiomyopathy.

Voltage-gated calcium channels (VGCCs) have been suggested as another potential source for the initial rise in intracellular calcium. VGCCs open in response to the initial membrane depolarization during the cardiac action potential, providing the positive feedback necessary for excitation-contraction coupling [44]. L-type VGCCs have been investigated for their role in DMD-cardiomyopathy. This specific VGCC is closely tied to dystrophin, as it is linked to the cytoskeleton through its involvement with dystrophin and α-actinin [45]. It was seen that in *mdx* mouse hearts, L-type VGCCs had a decreased inactivation rate which led to abnormal EGC tracings. It is thus predicted that this delayed inactivation contributes to the increased levels of intracellular calcium.

A downstream effect of the increase in intracellular calcium is dysfunctional calcium release from the sarcoplasmic reticulum. The sarcoplasmic reticulum functions as storage for the majority of the calcium required for the activation of contractile machinery [46]. Chiefly responsible for calcium release from the sarcoplasmic reticulum is the ryanodine receptor (RyR). RyR is activated by calcium binding in the sarcoplasm, and in DMD, RyR becomes sensitive to the increased level of intracellular calcium, resulting in excessive calcium release from the sarcoplasmic reticulum [47]. Additionally, RyR can be phosphorylated by protein kinase A (PKA) or calcium/Calmodulin kinase II (CaMKII) and hyper-phosphorylation of RyR makes it more sensitive to calcium activation and causes dissociation of stabilizing protein calstabin 2 [36]. These changes drastically impede proper RyR function, resulting in a leaky sarcoplasmic reticulum, further exacerbating the abnormally high level of intracellular calcium [48]. RyR involvement in *mdx* mouse cardiomyopathy was indirectly assessed through the measurement of sarcoplasmic reticulum leak, which was seen to increase with age in *mdx* mice [49].

Also responsible for regulation of calcium storage in the sarcoplasmic reticulum is the sarcoplasmic/endoplasmic reticulum calcium ATPase (SERCA). After cellular contraction,

SERCA actively pumps calcium from the sarcoplasm back into the sarcoplasmic reticulum to prepare the cardiomyocyte for the next contraction [50]. It is not clear whether SERCA plays a significant role in dystrophic cardiomyopathy, as one report found down-regulation of SERCA in *mdx* mice [5], whereas another more recent study found no significant difference in expression level and believe that any observed decrease may be merely due to aging as opposed to DMD-related cardiac pathology [51].

It is evident that calcium signaling plays a significant role in cardiac function in relation to DMD-related cardiomyopathy. The role of several different regulators of calcium levels have been investigated, indicating that a variety of mechanisms are likely involved.

Nitric oxide signaling

Nitric oxide (NO) is signaling molecule important for cell physiology that is dysregulated in dystrophic cardiomyopathy. The production of NO is controlled by nitric oxide synthase (NOS), which has three isoforms, neuronal NOS (nNOS), endothelial NOS (eNOS), and inducible NOS (iNOS). Cardiac cells constitutively express both nNOS and eNOS, and their localization is paramount to their proper function, as NO has a short life span and thus needs to be produced in close proximity to its target [52]. nNOS localizes to the dystroglycan complex (DGC) via syntrophins in close proximity to calcium channels on the sarcoplasmic reticulum, SERCA and RyR. Similarly, eNOS also localizes to the DGC and associates with calveolin-3. The remaining isotope, iNOS, is only expressed in cardiac tissue during inflammation.

In the absence of dystrophin, the DGC does properly organize or localize to the sarcolemma, inhibiting the proper localization of NOS. The role of nNOS in the heart has not yet been completely elucidated; however, several have characterized the effect of its removal and its expression in *mdx* mice. Removal of nNOS has been shown to affect downstream pathways of mitochondrial function also affected in DMD, including RyR regulation, ROS control, and the mitochondrial respiratory chain [53]. In the *mdx* mouse, transgenic nNOS overexpression has

been shown to partially rescue cardiac phenotypes, with a decrease in inflammatory markers and fibrosis [54]. Significant work remains in order to elucidate the role of NO signaling in dystrophic cardiomyopathy.

Mitochondrial dysfunction

Muscle cells, both skeletal and cardiac, require vast amounts of energy to support proper contraction. In these cells, the bulk of energy production and metabolic regulation occurs in the mitochondria. Beyond the production of energy, mitochondria play a role in the regulation of the intracellular balance of calcium and reactive oxygen species (ROS) and in the more general regulation of metabolic function. It has been shown that *mdx* mice hearts have abnormal mitochondrial function, indicating the existence of a role for this organelle in DMD-cardiomyopathy.

Mitochondria participate in the removal of calcium from the sarcoplasm through the mitochondrial calcium uniporter [46]. This removal accounts for only 1% of intracellular calcium and is thus inconsequential for sarcomere relaxation; however, rising amounts of intra-mitochondrial calcium can cause an increase in the rate of energy production in order to meet the perceived increasing energy demands of the cell. With a calcium-triggered increase in energy production comes increased generation of ROS, a by-product of aerobic metabolism. While ROS are involved in a variety of signaling pathways in healthy cells, their accumulation can be cytotoxic [55]. In anticipation of increased intra-mitochondrial ROS, an increase of calcium stimulates the opening of the voltage-sensitive mitochondrial permeability transition pore (mPTP). Ordinarily, the opening of mPTP allows for the release of ROS from the mitochondria and causes mitochondrial swelling [56]. However, long-term opening of mPTP is damaging, eventually resulting in mitochondrial necrosis, which contributes to cardiomyocyte apoptosis. Increased duration of mPTP opening has been observed in both murine *mdx* isolated cardiomyocytes [49] as well as in induced pluripotent stem cell-derived cardiomyocytes (iPSC-CMs) obtained from human DMD

patients [57], indicating that this process may play a role in DMD-associated cardiomyocyte degeneration.

A broad metabolic shift is seen in *mdx* mice. Healthy cardiac muscle uses mostly fatty acids for energy consumption; however, pre-cardiomyopathic *mdx* mice exhibited a shift toward metabolic consumption of carbohydrates [8]. The oxidative stress associated with DMD-cardiomyopathy has also been shown to reduce the oxidative capacity of the mitochondria in the *mdx* mouse [9]. Oxidative stress was shown to reduce the rate of oxidative phosphorylation, resulting in an overall decrease in energy production. This conflict of the increasing need for energy in the weakened cardiomyocyte with the inability of the mitochondria to fulfill this energy demand contributes to further cellular damage. It remains unclear whether the metabolic changes discussed occur as a compensatory mechanism or whether they are a direct, detrimental result of the dystrophin mutation.

1.1.5 Standard of care

There is currently no cure for DMD. Current approaches focus on slowing the progression of the disease and alleviating symptoms. Accordingly, currently treatments fail to target any DMD-specific mechanisms of disease.

Non-cardiac treatment

Beyond cardiomyopathy, DMD patients suffer from progressive skeletal muscle deterioration. Non-cardiac treatments for DMD focus on improving muscle strength and function as well as treating associated pulmonary and spinal deficiencies. Steroids have been used extensively to treat DMD-related muscle weakness. Specifically, corticosteroids have been shown to improve not only skeletal muscle strength and function as related to mobility, but also as related to pulmonary function [58].

Respiratory difficulties continue to amount in patients with DMD due to the loss of diaphragm and other respiratory muscle strength. Historically, respiratory failure was most often the cause of death of DMD patients; however, the implementation of noninvasive nocturnal ventilation has greatly improved the efficacy of hypoventilation treatment and the average life span of those affected by DMD [3]. Scoliosis and kyphosis are other common symptoms developed in DMD patients. Spinal stabilization surgery is often recommended to alleviate discomfort and difficulty breathing [59]. In addition to these treatments, significant effort is put into rehabilitation through diet, exercise, and counseling.

Cardiac treatment

To a large extent, the treatment of DMD-cardiomyopathy relies on long-standing pharmaceuticals and surgical interventions to improve cardiac systolic function and heart rate regulation used in other forms of dilated cardiomyopathy. Frequently used pharmaceuticals include corticosteroids, angiotensin-converting enzyme (ACE) inhibitors and angiotensin receptor blockers (ARBs), beta-adrenergic receptor blockers (beta-blockers), and aldosterone antagonists.

As previously described, the use of corticosteroids, such as prednisone and deflazacort, is almost ubiquitous in the treatment of DMD patients. These steroid molecules are known to delay the rate of muscle degeneration, and they are believed to act by reducing the inflammatory response in muscle cells that is often responsible for myocyte necrosis [58]. In addition to treating skeletal muscle and pulmonary deficiencies, corticosteroid treatment has been shown to also improve cardiac function in DMD patients [60]. A variety of retrospective studies examining the efficacy of corticosteroid treatment in DMD have seen an increase in the age at onset of cardiomyopathy, an increase in fractional shortening, a decrease in cardiac dilation and systolic dysfunction, and an overall decrease in the incidence of cardiomyopathic mortality when patients are treated with deflazacort or prednisone.

Another pharmaceutical approach to treating DMD-cardiomyopathy is the use of ACE

inhibitors and ARBs, long-standing neurohormonal cardiac treatments. ACE inhibitors and ARBs are similar in their effects, they both inhibit sympathetic adrenergic stimulation and cause vasodilation. These vasodilators are widely used in the treatment of heart failure for their ability to decrease blood pressure and protect the damaged heart by decreasing the pressure loading on the heart. In patients with DMD, treatment with ACE inhibitors and ARBs have been shown to be equally efficacious in long-term preservation of left ventricular function [61]. Following these promising results, it has been suggested that DMD patients begin ACE inhibitor or ARB treatment before the onset of left ventricular dysfunction [20].

Current guidelines recommend that DMD patients with left ventricular dysfunction also be treated with beta-blockers [62]. However, there are conflicting results as to whether there is any improvement in cardiac function when beta-blockers are used in combination with ACE inhibitors as compared to the use of ACE inhibitors alone. Similarly to ACE inhibitors, beta-blockers inhibit sympathetic adrenergic stimulation in the heart. By blocking the binding of epinephrine to beta adrenergic receptors, beta-blockers decrease the heart rate, thereby decreasing cardiac work and blood pressure. A variety of other beneficial effects contributing to the treatment of heart failure have been described, including the reduction of arrhythmic events and improvement of diastolic function [63]. Given the increased occurrence of elevated heart rates and arrhythmic events in patients with DMD, it is a reasonable hypothesis that treatment with beta-blockers would yield beneficial preservation of cardiac function. A commonly used beta-blocker studied in DMD patients is carvedilol, which has additional vasodilating and antioxidant effects [63]. While it has been long established to treat cases of heart failure with a combination of ACE inhibitors and beta-blockers, it has yet to be definitively proven whether the addition of a beta-blocker regimen improves cardiac function in patients with DMD.

Lastly, aldosterone antagonists have been used to treat cardiomyopathy in DMD patients, as they are another standard treatment for heart failure when decreased left ventricular ejection

fraction is presented. Aldosterone inhibitors like eplerenone act as weak diuretics, resulting in decreased blood pressure. A double-blinded clinical trial was conducted to assess the effect of eplerenone treatment for DMD when administered in conjunction with ACE inhibitors or ARBs [64]. The endpoint measured in this study was left ventricular circumferential strain, an indicator of ventricular contractility. It was observed that the patients treated with eplerenone for 12 months showed a lower decrease in ventricular contractility as compared to placebo groups, although no significant differences in overall left ventricular function were observed.

The pharmacological treatment of DMD-cardiomyopathy has largely relied on existing treatments for general heart failure. While there has been significant success in this field regarding the preservation of cardiac function, further studies remain to assess the efficacy of these drugs and to determine the most efficient pharmacological regimen. It is worth mentioning that given the variation of presentations of DMD-cardiomyopathy as determined by the specific *dmd* mutation, it is likely that one drug regimen will not work for all patients, and that a case-by-case evaluation will be necessary.

Beyond pharmacological treatment, a variety of surgical techniques have been evaluated for their efficacy in treating DMD-cardiomyopathy, including orthotopic cardiac transplantation [65] and implantation of left ventricular assist devices [66] and implantable cardioverter-defibrillators [62]. While these procedures have often been implemented in patients with heart failure, their use in DMD patients is not widespread and further evaluation of their efficacy is needed. As compared to pharmaceutical treatment, surgical intervention may be less accessible in the treatment of DMD-cardiomyopathy due to the overall poor health of the patient. However, it may be worth evaluating the potential of such approaches on a case-to-case basis.

1.1.6 Emerging therapies

To date, there is no cure for DMD or its associated cardiomyopathy, and treatment is limited to palliative pharmacological treatment. Current treatment plans have three aims, namely,

corticosteroid treatment of skeletal muscle weakness, ventilatory support, and cardiac screening and treatment. As heart function deteriorates, DMD patients are put on regimens including combinations of angiotensin-converting enzyme (ACE) inhibitors, beta-blockers, and diuretics [67]. These are standard treatments for heart failure that reduce the pre-load on the heart, thus protecting it from further damage.

These standard-of-care cardiac treatments certainly promote cardiac protection and prolong the lives of DMD patients; however, there is nothing about these cardiac regimens that is specific to the molecular pathology of DMD. Thus, there is a need for the development of novel treatments for DMD-cardiomyopathy. Subsequent sections describe current efforts underway to identify novel pharmaceuticals that may be beneficial as well as the development of more modern treatment platforms including gene and cell therapies.

Novel pharmacological treatments

There are a variety of commercially available drugs that have been investigated for their potentially beneficial effects in treating DMD-cardiomyopathy. Poloxamer 188 is a synthetic polymer known to seal membrane tears and thus stabilize the sarcolemma [39]. When administered to *mdx* mice, poloxamer 188 was shown to improve cardiac function and protect dystrophic hearts from isoproterenol-induced damage [11]. However, when cultured with isolated *mdx* cardiomyocytes, poloxamer 188 was not able to fully reverse the increase in cytoplasmic calcium levels, indicating the complexity of the dystrophic molecular pathology. This treatment has not yet been translated to other animal models or human clinical trials.

Another target of pharmaceutical innovation has been in modulation of nitric oxide (NO)-cyclic GMP (cGMP) signaling, a pathway crucial for many cellular activities, including mitochondrial function and reactive oxygen species (ROS) balance. NO-cGMP signaling is decreased in *mdx* mice. Sildenafil, a phosphodiesterase 5 (PDE5) inhibitor, acts as a NO donor, stimulating NO-cGMP signaling. When used to treat *mdx* mice, sildenafil was seen to improve

cardiac systolic function and metabolism [68]. It was also shown to improve diaphragm strength and respiratory function [69]. However, no improvement in cardiac function was observed upon translation to human clinical trials [12]. Alternate efforts have proposed nicorandil as a pleiotropic, cardio-protective drug for DMD-cardiomyopathy. Nicorandil acts similarly to sildenafil in that it is an NO donor; however, it has additional effects as a potassium channel opener and an antioxidant. When used to treat *mdx* mouse hearts prior to ischemic stress, nicorandil promoted an increased recovery of left ventricular developed pressure (LVDP) [13]. Additional studies were conducted with dystrophic human hiPSC-derived cardiomyocytes, where pretreatment with nicorandil was shown to prevent cardiac injury, ROS generation, and cellular apoptosis upon induction of oxidative stress. Investigators hypothesize that nicorandil will translate to human subjects better than sildenafil due to its pleiotropic effects.

Voltage-gated L-type calcium channels have been hypothesized to contribute to dystrophic cardiomyopathy, as they are linked to the cytoskeleton in part by dystrophin and α-actinin [70]. Accordingly, increased L-type calcium channel currents and slowed channel inactivation has been observed in *mdx* mice [71]. More recently, a preliminary drug screening experiment using DMD human stem cell-derived cardiomyocytes identified 39 compounds out of a panel of 2,000 that had a cardioprotective effect against hypotonic stress, of which 9 were classified as calcium channel blockers [72]. These results give further credence to the possible utility of calcium channel blockers in the treatment of dystrophic cardiomyopathy, although further clinical studies are needed.

Given the severe cardiac fibrosis characteristic of DMD-cardiomyopathy, losartan and pirfenidone, TGF-β inhibitors, have been evaluated as potential treatments [47,48]. Both drugs were seen to reduce fibrosis and improve cardiac function in *mdx* mice. Further studies in human patients remain to be seen.

It is evident that a variety of commercially available drugs may be beneficial in treating specific mechanisms involved in the cardiomyopathy of DMD patients, either alone or in combination with current treatments. Further studies will need to be conducted before these treatments can be evaluated in human clinical trials.

Gene repair therapy

The majority of DMD mutations occur as either a large exon deletion or point mutation resulting in a frameshift or premature stop codon. In the majority of patients, some form of dystrophin expression could be reintroduced if the reading frame could be restored at the level of DNA or RNA. Current technologies have the potential to achieve this, including read-through therapy and exon skipping.

Roughly 10-15% of DMD patients have a nonsense mutation, resulting in a premature stop codon [73]. To reverse this, several compounds have been assessed for their ability to read through premature stop codons [17]. Gentamycin [74] and PTC124 [75–77] have been tested in *mdx* mice and DMD patients, however clinical trials were inconclusive with very low treatment efficacy shown. RTC13 has shown promising results in studies in *mdx* mice, yet further studies will be required to evaluate the applicability of this promising therapeutic to human patients [78].

A larger proportion of DMD patients, roughly 80%, have a frameshift mutation due to a larger deletion or duplication that results in a null phenotype. Exon skipping is being developed as a strategy to treat this category of patients. Exon skipping employs antisense oligonucleotides (AONs), which are short, single-stranded DNA sequences that are targeted to the splice site of the damaged exon [79]. Upon binding, the AON prevents proper splicing, resulting in the damaged exon being spliced out of the mRNA transcript, and restoring the proper reading frame. Upon the translation of the newly spliced mRNA, a slightly shorter, but hopefully functional, dystrophin is expressed. Theoretically, a library of AONs could be generated to facilitate exon skipping in a wide array of DMD mutations. Exon skipping, thus far, has been shown to be very effective in

restoring dystrophin expression and improving skeletal muscle function in both *mdx* mice and CXMD dogs [80]. Eteplirsen is the first exon skipping drug approved by the FDA, despite only being shown to restore ~1% of normal dystrophin expression after a year of systemic dosing [81, 82]. However, these initial studies have been done using AONs based on 2′-O-methylated phosphorothioate (2OMe-PS) or phosphorodiamidate morpholino oligomers (PMOs), which are unable to reach the heart. To overcome this, a variety of modified PMOs have been developed that are linked to proteins facilitating cell-penetration [83]. These novel modified AONs have been shown to restore dystrophin expression and cardiac function in the *mdx* mouse.

Gene editing

Recent advances in CRIPR-Cas9 gene editing are being explored as potential treatments for DMD. By generating guide RNAs that target the sites of *dmd* mutations, a patient's DNA can be cleaved and repaired in such a way that the proper reading frame is restored [84]. This technique is applicable for DMD due to the modular structure of dystrophin, which can retain near-normal function when truncated internally, and the existence of only one allele on the X chromosome of affected males. Many studies have shown the success of this strategy in restoring dystrophin expression in *mdx* mice [85–90], a canine model of DMD [91], and hiPSC-CMs [86, 92–96]. Further studies are needed to show that this restoration of dystrophin expression is sufficient to correct skeletal and cardiac muscle phenotypes. A limitation of this technique is the large variety of DMD mutations, many of which would require specific gene editing designs, and the existence of mutations which are not amenable to gene editing. Challenges remaining include the efficiency of CRISPR-Cas9 delivery and gene editing, concerns of possible off-target effects, and general popular concern regarding the safety and ethics of gene editing.

Gene replacement therapy

Another promising approach to treating DMD and its associated cardiomyopathy is to

deliver a viral vector with exogenous DNA to expressing dystrophin. Delivery of full-length dystrophin can be problematic because the dystrophin gene is extremely large, containing 79 exons in a 14-kb cDNA transcript [30]. This is too large to be contained within most viral delivery vectors. Other methods are to engineer synthetic, truncated dystrophin constructs that maintain full functionality of endogenous dystrophin.

Delivery of full-length dystrophin transcripts has been attempted using non-viral delivery methods. Direct plasmid injection in mdx mice was first evaluated in 1991, where only 1% of myofibers were observed to express dystrophin [97]. Following these studies, direct plasmid injection has been evaluated in GRMD dogs and in Phase 1 clinical trials [98]. Other attempts have used non-viral DNA delivery methods, including electroporation, microspheres, and liposomes. Overall, these efforts have yielded low delivery and expression efficiencies, which has limited the further development of plasmid-based therapies.

The most effective systemic muscle gene-delivery method to date is using an adeno-associated virus (AAV). AAVs, to date, are the most desirable viral delivery method for skeletal and cardiac muscle, as they are able to transfect post mitotic cells, do not integrate into the host genome, and illicit minimal immune response compared to other viral methods. However, AAVs have a packaging limit of 5-kb, severely limiting the size of transgenes that can be delivered. Inspired by the smaller dystrophin isoforms expressed endogenously and in less severe cases of Becker muscular dystrophy, groups have worked on evaluating the crucial parts of dystrophin needed for proper function. It has been shown that while the N-terminus domain and the R16/17 region of the rod domain (necessary for NO synthase localization) are necessary for proper function, the rest of the rod domain and most of the C-terminus domain may not be required for proper function [99]. With this in mind, a variety of micro-dystrophins compatible with AAV delivery have been engineered (Figure 3) [100–105]. When delivered via a serotype-9 AAV, these micro-dystrophins have enabled whole body gene transfer in mdx mice with high delivery and

expression efficiency [106, 107]. These constructs have also been shown to induce whole body gene transfer in neonatal dogs [108, 109]. Three clinical trials are currently underway to evaluate the efficacy of micro-dystrophin treatment. These micro-dystrophin constructs are currently at the cutting edge of DMD gene therapy due to their high delivery and expression efficiencies; however, their therapeutic benefit in humans remains to be fully demonstrated.

Other groups have tried to circumvent the low packing limit of AAVs through engineered tri-AAV vector systems [110, 111]. In these systems, the 14-kb dystrophin transcript is split into three pieces, each piece containing either an overlapping region or a splicing signal. Each piece is packed into an individual AAV, and the expression of all three components results in transcript reconstitution and full-length dystrophin expression. This approach has been tested in mdx mice, but low transfection efficiencies and subsequently low dystrophin expression has hindered a full analysis of the therapeutic benefits of this system.

Despite the promising developments in DMD gene therapy, significant challenges currently prevent this technology from being used to treat human patients. The first challenge is to ensure proper levels of dystrophin expression, as low expression may not be beneficial, and over expression may be toxic. In *mdx* mice, it has been seen that expressing dystrophin at a 20% level was sufficient to mitigate skeletal muscle symptoms [112], and that even 5% expression could delay the progression of muscle degeneration and prolong the lifespan of affected mice [113]. Currently, it does not seem like overexpression will be a concern, as 50-fold overexpression in *mdx* mice was not seen to be toxic in skeletal muscle [114]. However, these dosages have yet to be evaluated in cardiac muscle or in large animal or human models. Another concern is the applicability of using dystrophin gene therapy to treat DMD-cardiomyopathy, as initial studies have largely focused on the transduction of skeletal muscle. Beyond the high incidence of cardiomyopathy in DMD patients as motivation, there is evidence that treating skeletal muscle while ignoring the heart actually accelerates the development of cardiomyopathy [115]. While

these findings have been contested, gene therapy should treat both skeletal and cardiac muscle. Lastly, new challenges have emerged upon translation to large animal cDMD models. Whereas initial gene therapy studies were largely conducted on immune-deficient *mdx* mice, it was soon realized that intramuscular AAV injection elicits a strong immune response in dogs [116]. If this is the case in humans, long-term immune suppression could be required to ensure transgene expression.

Cell therapy

The aim of cell therapies for DMD is to supplement dystrophic muscle with healthy, dystrophin-expressing cells. More promising approaches use cells taken from the patient that have been subsequently genetically altered in vitro and differentiated into muscle precursor cells. Initial studies used isolated adult stem cells, such as bone-marrow stem cells or CD133+ cells [117, 118]. More recent studies have shifted toward the use of hiPSCs, thus increasing the availability of donor cells. Efforts to this end have taken human embryonic stem cells (hECSs) and human hiPSCs, differentiated them into muscle precursor cells, and injected them into the tibialis anterior muscle of immune-deficient *mdx* mice [119]. These cells were seen to fuse with existing muscle cells, restoring dystrophin expression. Similar studies have employed similar methods and observed an increase in skeletal muscle force generation [120].

The development of modern gene editing techniques has facilitated the development of therapies where cells would be taken from a DMD patient, reprogrammed into hiPSCs, genetically modified to correct the dystrophin mutation, differentiated into muscle precursor cells, and reintroduced into the patient's muscle. This approach is advantageous in that there is a much lower risk of immune response and rejection. TALENs and CRISPR-Cas9 have been successfully used to correct dystrophic hiPSCs by knock-in with the correct exon [94]. When differentiated toward skeletal muscle, expression of full-length dystrophin was observed. These cells hold great promise for treating DMD patients using autologous cell therapy.

There remain several limitations with cell-based therapies. Producing sufficient numbers of cells remains a challenge, especially considering the large scale-up required when moving from animal models to human patients. Currently, cell therapy for DMD has been shown to be most effective when cells are injected intramuscularly, which would require that every muscle be injected individually [121]. Currently, this type of treatment has not been evaluated for diaphragm or cardiac muscle, which limits its utility in treating the entire dystrophic phenotype.

1.2 Disease Models for Studying DMD: Advantages and Limitations

1.2.1 Animal models of DMD

Animal models of DMD have been an invaluable resource, granting insight into the mechanisms of the pathology as well as providing a platform for preclinical trials. However, no one animal is capable of perfectly emulating the human progression of DMD, warranting a discussion of the advantages and limitations of different models. In evaluating the usefulness, one should consider the similarity of the animal model to human DMD patients regarding progression and severity of skeletal muscle degeneration and cardiomyopathy.

Mouse models

The *mdx* mouse is the most commonly used animal model for DMD [122]. This colony of C57BL/10ScSn mice, first described in 1984, harbors a nonsense point mutation in exon 23 that prevents the expression of dystrophin. Despite their lack of dystrophin, *mdx* mice present minimal symptoms of DMD. Severe symptoms are not observed until 15 months of age, at which point *mdx* mice present with severe muscle degeneration, scoliosis, and heart failure [123]. The life span of *mdx* mice is only reduced by 25%, whereas the life span of human DMD patients is reduced by 75% [124]. Despite the advantages of mice models with respect to size, cost, and turnover rate, there are clearly significant shortcomings of the *mdx* mouse as related to clinical relevance.

A possible reason for the minimal disease phenotype seen in *mdx* mouse strains is the upregulation of compensatory mechanisms. Specifically, utrophin and α7β1-integrin function similarly to dystrophin, strengthening the sarcolemma through interactions with the cytoskeleton and the extracellular matrix, and these two proteins are known to be upregulated in *mdx* mice [80]. It was hypothesized that the creation of a double-knockout (*dko*) mouse, either utrophin/dystrophin or α7β1/dystrophin *dko*, would worsen the presented phenotype [18,19]. These *dko* models are smaller than their wildtype counterparts and do present with more severe muscle degeneration at levels comparable or perhaps exceeding that presented by humans; however, they are increasingly difficult to maintain, and their lifespan is diminished more significantly than that of human patients. More recent studies have presented an *mdx* strain with a heterozygous utrophin knockout as a potential intermediate between *dko* mice and *mdx* mice [127].

Another reason for the relatively mild DMD phenotype presented by *mdx* mice is robust muscle regeneration, a trait not observed in human DMD patients. Double-mutant mice targeting myogenic regulators have been bred to address this. *Mdx* mice harboring MyoD/dystrophin double-knockouts showed increased myopathy, premature death, and importantly, dilated cardiomyopathy, despite the fact that MyoD is only expressed in skeletal muscle [128]. Another approach targeted telomere length, as it was hypothesized that the long telomere length found in mouse myogenic stem cells is responsible for their increased regenerative capacity. Telomerase RNA (mTR) is required for telomere maintenance, and when it was removed from *mdx* mice, the resultant strain demonstrated marked skeletal wasting and cardiomyopathy [129]. A variety of other mechanisms have been targeted in double-knock out mice lines to produce a severe dystrophic phenotype, including cytoskeleton-extracellular matrix interactions (desmin and laminin), the DGC (dystrobrevin and sarcoglycan), muscle repair, and inflammation and fibrosis [80].

Thus, it can be seen that while advantageous with regard to ease of maintenance and cost, the *mdx* mouse model alone is insufficient to fully emulate the severity of the human DMD phenotype, particularly with regard to dystrophic cardiomyopathy. However, it has been shown that the addition of other mutations can worsen the disease phenotype, perhaps improving the relevancy of disease phenotypes. This improvement comes with additional limitations, as these double-knockout lines harbor mutations not found in human DMD patients which may contribute irrelevant, off-target effects.

Canine models

While mouse models may be sufficient for initial studies and preclinical trials, their differing physiology and presentation of only mild symptoms presents the need for a larger, more relevant animal model. Naturally occurring X-linked muscular dystrophy in canines has long been reported, and dystrophin deficiency has since been confirmed in roughly 20 different breeds [130]. The disease associated with this collection of mutations has come to be known as canine Duchenne muscular dystrophy (cDMD). The clinical presentations of cDMD are more severe than the presentations of *mdx* mice, and thus, they are considered a more relevant model of human DMD.

cDMD dogs present clinical symptoms and histology very similar to that of human DMD patients at analogous time points [80]. Both present with early signs of muscle weakness and exercise intolerance, followed by continued muscle wasting, joint contracture and abnormal gait, difficulty swallowing, and early signs of cardiomyopathy. The average lifespan of cDMD dogs is roughly 3 years, which corresponds to the 75% reduction in life expectancy seen in human DMD patients. Histologically, cDMD dogs exhibit marked fibrosis in limb muscles, a trait also seen in humans but not in *mdx* mice. Whereas high levels of muscle regeneration is seen in *mdx* mice, as evidenced by centrally nucleated myofibers, this is seen in neither cDMD dogs nor humans.

However, the pathology of cDMD is not identical to that of human DMD. Notably, 20-30% of cDMD puppies die shortly after birth due to diaphragm failure, whereas this incidence of

neonatal death is not observed in humans [131]. Additionally, shortcomings in growth and body weight are increasingly pronounced in cDMD dogs, and these dogs rarely experience the complete loss of ambulatory function seen in humans [132].

Ultimately, cDMD dogs share many similarities with human DMD patients, making them better models for preclinical studies. While many varieties of cDMD have been identified, few have been sufficiently characterized and only a few breeds have been established as experimental colonies. However, the *mdx* mouse remains the most widely used model of DMD due to its advantages of low cost and high accessibility.

Rat models

More recently, a rat model for DMD has emerged, promising more relevant phenotypes, while maintaining the ease of use and low cost associated with murine models [133]. This rat line, referred to as *Dmd*^{mdx}, was created using a pair of TALENs targeting exon 23 to generate mutations similar to that seen in the *mdx* mouse. The *Dmd*^{mdx} rat has an 11-bp deletion in exon 23, resulting in a frameshift mutation, premature stop codon, and ultimately a dystrophin-null phenotype. Only male *Dmd*^{mdx} rats are affected while female littermates show no symptoms, indicating the X-linked recessive nature of this mutation.

As compared to the *mdx* mouse, *Dmd*^{mdx} rats display a disease phenotype and progression similar to that of human DMD patients. As early as 3 months after birth, *Dmd*^{mdx} rats display severe degeneration of skeletal and diaphragm muscles. By 7 months of age, these muscles also display severe fibrosis and even adipose tissue deposition, a DMD trait not observed in the *mdx* or cDMD models. The *Dmd*^{mdx} rat also presents gradual development of dilated cardiomyopathy, as evidenced by histological analysis and echocardiography revealing cardiac remodeling and decreased systolic function. The severity of cardiomyopathy seen in the *Dmd*^{mdx} rat is more severe than other DMD animal models.

There are additional benefits that the *Dmd*^{mdx} model presents as a small animal model due to inherent differences between mice and rats. Rats are roughly ten times larger than mice, making them easier to handle and characterize while being sufficiently small to facilitate studies with high sample sizes. With this increase in size comes an increase in behavioral displays. Rats have finer and more controlled motor skills than mice, facilitating the development of gait analysis, a measure crucial to understanding DMD development previously inaccessible in mice. The *Dmd*^{mdx} rat has yet to be used in gene therapy studies. However, given the marked improvements over the *mdx* mouse model, the *Dmd*^{mdx} rat is a promising new small animal model of DMD.

1.2.2 Use of human induced pluripotent stem cells for modeling DMD

Despite any level of phenotypic representation seen in DMD animal models, there will always be inherent species differences that will affect the molecular pathology and progression of disease. This could be at fault for the low efficiency in the translation of experimental treatments to human patients. As such, it is necessary to develop representative human in vitro disease models for preliminary studies using human cells.

The isolation and in vitro culture of primary human cardiac cells is often infeasible. Thus, the advent of induced pluripotent stem cell (iPSC) technologies has revolutionized the field of in vitro disease modeling [134]. Since then, robust differentiation protocols have been developed that utilize small molecules to drive differentiation of stem cells toward cardiac progenitors and cardiomyocytes [135]. Thus, it is now possible to isolate somatic cells from DMD patients, reprogram them into hiPSCs, which serve as a renewable source to differentiate into cardiomyocytes or theoretically any cell type [136]. Additionally, with the advent of CRISPR-Cas9 gene editing, it has become increasingly common to generate DMD mutations in healthy control lines or correct DMD mutations such that isogenic-matched cell lines can be used.

There has been increasing interest in using hiPSCs to model and study DMD in vitro, to which end several hiPSC lines with different dystrophin exon deletions and point mutations have

been developed [137]. These studies have produced known dystrophic phenotypes in vitro as well as elucidated novel consequences downstream of absent dystrophin. As hypothesized, many groups have found that dystrophic hiPSC-CMs exhibit increased membrane fragility and susceptibility to stretch-induced damage [138–140]. With regard to electrophysiology and calcium handling, many have shown DMD hiPSC-CMs to display increased L-type calcium channel currents [141] and spontaneous electrical activity or arrhythmic events [95, 138, 140, 142], slower calcium transients [95, 143], and increased resting intracellular calcium [138, 139]. With regard to mitochondrial function, it has been shown that DMD hiPSC-CMs display increased mitochondrial damage and ROS production [139, 144, 145]. Initial studies have used hiPSC-CMs to evaluate novel therapeutic approaches for their ability to restore dystrophin expression and reverse observed phenotypes, including CRISPR-Cas9 correction [86, 92, 93, 95] and exon skipping [140, 146]. Of note, micro-dystrophin gene therapy has not yet been tested in hiPSC-CMs.

Our group has previously developed novel hiPSC lines isolated from urine samples of a DMD patient with an exon 50 deletion and a healthy control [57]. This method promises to increase the ease of obtaining patient samples, due to the non-invasive nature of sample collection, as compared to other methods requiring skin biopsy or blood samples. These urine-derived hiPSCs were differentiated into cardiomyocytes, which maintain the dystrophin mutation present in the donor. These dystrophic hiPSC-derived cardiomyocytes display a disease phenotype in vitro, as the dystrophic cells were seen to have impaired calcium handling, altered mitochondrial function and oxygen consumption, and increased expression of cardiac injury markers upon hypotonic stress, as compared to the healthy control [57].

More recently, we have made use of CRISPR-Cas9 gene editing to generate a dystrophin-mutant hiPSC line from an isogenic healthy control [14, 72, 147]. In this line, a single base pair deletion (263delG) was made in the first exon of dystrophin, which resulted in the truncation of exons 1-6 in the actin-binding domain [147]. When cultured on anisotropic nanotopographic

substrates, it was shown that DMD hiPSC-CMs exhibited a diminished response to the topographic cues, in part due to slower actin cytoskeleton turnover [72]. In a follow up study, it was shown that providing DMD hiPSC-CMs with a combination of maturational cues revealed further dystrophic phenotypes, including increased resting cytosolic calcium content and increased propensity for arrhythmia [14]. This cell line was also shown to display disease phenotypes at the myofibril level, as it was demonstrated that isolated myofibrils from DMD hiPSC-CMs produced lower contractile force, slower kinetics of relaxation, altered expression of sarcomere proteins, and increased calcium sensitivity [147]. What has become apparent from these studies is that advanced maturation techniques are likely required to expose dystrophic phenotypes in DMD hiPSC-CMs, as these studies only observed differences after culture on anisotropic nanotopography [72], a combination of nanotopographic substrates, thyroid hormone, and miRNA overexpression cues [14], or long-term culture (80-100 days) [147].

1.2.3 Addressing limitations of hiPSC-CMs

Challenges remain in the development of relevant in vitro models of DMD-cardiomyopathy. Notably, the relative immaturity of hiPSC-derived cardiomyocytes remains a hurdle in recapitulating the pathology experienced by teenagers and young adults. In early stages after differentiation with no intervention, hiPSC-CMs display only fetal transcriptomes [148], ion channel expression [149], metabolic function [150], and contractility [151]. This is a struggle encountered by the entire field surrounding stem cell-derived cardiomyocytes, and significant efforts have been devoted to identify cues and develop protocols to promote the maturation of these cells [152–154]. These include providing topographical cues in the form of relevant substrate stiffness [155–157] and patterned substrates [72, 158–160] encouraging proper uniaxial cellular and sarcomeric alignment. Other studies have identified benefits in maturation after supplementing cells with thyroid hormone [161] or fatty acid energy sources [162–164]. Further studies have shown increased maturation when hiPSC-CMs are cultured with other cell types,

including endothelial cells [165, 166] and mesenchymal stem cells [167]. Equally important, biophysical cues in the form of electrical and mechanical stimulation have been shown to drive hiPSC-CM maturity [168, 169]. Lastly, as will be further discussed in the following section, many are looking to three-dimensional culture as a method to better emulate the native myocardium. This is by no means an exhaustive review of hiPSC-CM maturation methods, but what is evident is that a multifaceted approach is necessary to push hiPSC-CM maturation to its fullest extent.

An additional challenge is that current in vitro models are unable to represent an entire patient, which is limiting in terms of evaluating delivery efficiency as well as host response and systemic toxicity of treatments. Thus, while human stem cell-derived dystrophic cardiomyocytes promise a useful intermediate in the study of DMD, animal models will remain the gold standard for evaluation of novel treatments until suitable in vitro replacements are developed.

1.3 Human Engineered Heart Tissues

In an effort to advance in vitro cardiac disease modeling and drug testing, many have turned to three-dimensional tissue culture platforms to provide biophysical cues that are difficult to emulate in traditional two-dimensional culture, as described in Chapter 2 [170]. The various methods described yield cardiac tissues that generate synchronous, measurable contractions, facilitating the measurement of force production, a valuable metric for assessing cardiac function.

1.3.1 Platforms for 3D cardiac tissue engineering

These engineered heart tissue (EHT) platforms consist of cardiac and other cell types embedded in a scaffold matrix, most often a hydrogel consisting of fibrin, collagen, decellularized primary extracellular matrix, and/or Matrigel. Initial EHT platforms used primary neonatal rodent cardiomyocytes [171], but more recently, groups have turned to using hiPSC-CMs for fully human in vitro models. Most often, another cell type is added to support tissue compaction and cohesion, often these are fibroblasts, HS27a bone marrow stromal cells, or the non-myocyte population

derived from cardiac directed differentiation. There is great variety in EHT platform shape and size, ranging from smaller spheroids [172, 173] and micro tissues [174, 175] to larger cardiac strips [176], rings [177], biowires [178, 179], and cardiac sheets and patches cast on PDMS frames [180–182]. These platforms can be used to measure contractile force, either directly via force transducer or indirectly by the measured deflection of cantilever posts, and calcium transients using calcium dyes or genetically encoded calcium sensors.

We have previously utilized this technology to develop an EHT platform that consists of hiPSC-CMs and stromal cells embedded in a fibrin matrix suspended between two polydimethylsiloxane (PDMS) posts, one flexible and one rigid [183–185] (**Fig. 1.3**). These EHTs generate synchronous contractions, the force of which can be measured via optical tracking of the flexible post, or by magnetic tracking of a small magnet embedded in the tip of the flexible post [184]. In previous studies, we have demonstrated that EHTs exhibit relevant responses to isoproterenol and verapamil [184], and we have used this platform widely to investigate the effect of afterload on hiPSC-CM maturation [183], the function of full-length and Cronos titin [186], the effect of lamin A/C haploinsufficiency [187], and the development of electroconductive EHTs [188]. Here, we describe a novel application of this EHT platform in generating a disease model to study dystrophic cardiomyopathy.

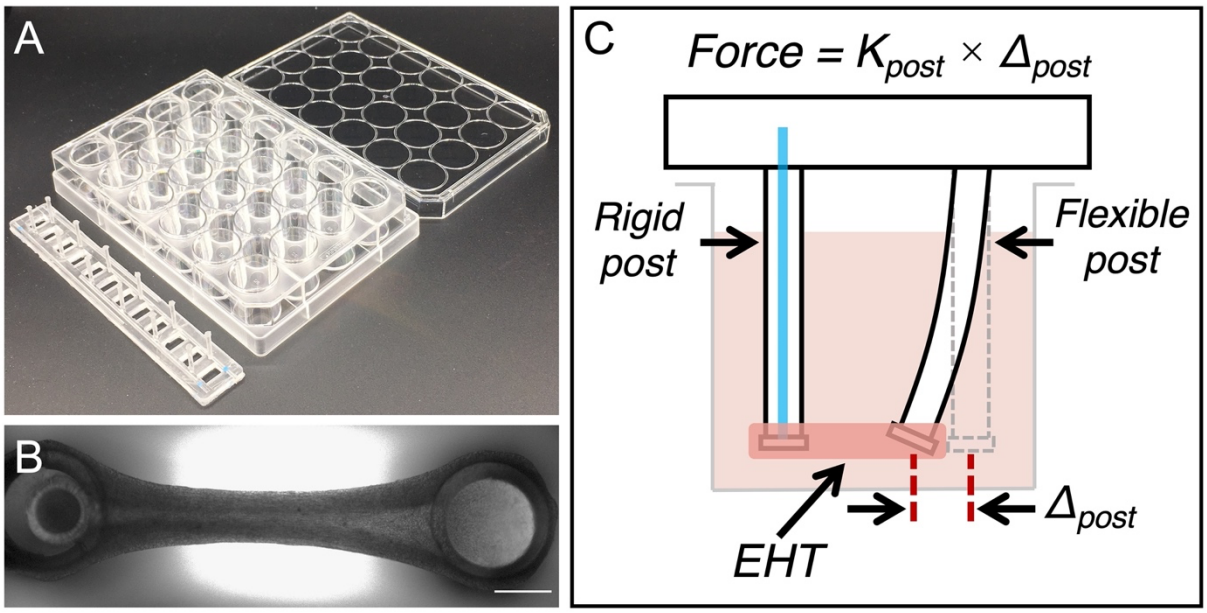

Figure 1.3. Engineered heart tissue platform. (A) Array of six pairs of PDMS posts that fit a standard 24-well cell culture dish. (B) Representative image of an EHT suspended between the rigid post (left) and flexible post (right). Scale bar is equal to 1 mm. (C) Schematic of an EHT in culture, where force of contraction is calculated using the stiffness of the flexible post (K_{post}) and its measured deflection (Δ_{post}).

1.3.2 Advantages of 3D in vitro cardiac models

Compared to two-dimensional culture platforms, EHTs are advantageous in that they better replicate the native cardiac microenvironment. As such, they have been shown to promote advanced hiPSC-CM maturation [189–193]. As a multicellular tissue with ample scaffolding proteins, EHTs provide cell-cell and cell-matrix interactions. With the use of hydrogels, material stiffnesses are achieved that are much closer to the mechanical moduli of native cardiac tissue as compared to rigid tissue culture plastic. This is especially important when attempting to recapitulate membrane protein complexes such as the DGC, as myocytes grown on rigid surfaces form focal adhesions rather than the physiologically relevant costameres found *in vivo.* Native cardiomyocytes exhibit anisotropic cellular and sarcomeric alignment, something that is not recapitulated in standard 2D culture. Thus, topographical cues are required to promote alignment

of 2D hiPSC-CMs, which requires methods such as micro-contact printing [194] or nano-topographical surfaces [72]. In EHTs, the applied anisotropic force gradient produces uniaxially-aligned cells without the need for intervention. Force production is a critical measure of cardiac function, yet measuring contractile function of 2D hiPSC-CMs requires methodologically and computationally intensive techniques such as atomic force microscopy or traction force microscopy. Comparatively, force production in EHTs can easily be measured, as they can be embedded on elastomeric posts and their larger size allows for them to be mounted to standard force transducers. Advanced engineering approaches have been employed to further increase the maturity achieved in EHTs. There approaches include electrical stimulation [195], increasing afterload [183], and the addition of preload or passive stretch [196, 197]. Given these advantages, EHTs have been enthusiastically received by cardiac researchers, and have begun to be widely used for drug testing and disease modeling [176, 198–201].

1.3.3 Dystrophic engineered heart tissues

To date, little work has been done to model human DMD in three-dimensional culture. As of this writing, dystrophic EHTs have only been reported in one publication, where it was briefly shown that DMD EHTs produced less contractile force, and this phenotype was partially rescued with three CRISPR-Cas9 gene editing approaches [95]. Of note, this study performed the gene editing on undifferentiated hiPSCs, before differentiating to cardiomyocytes. To our knowledge, the work described herein is the first to thoroughly characterize a dystrophic phenotype in a three-dimensional EHT in vitro model. Additionally, the future work presented in Aim 2 will be the first to evaluate the efficacy of novel micro-dystrophin gene therapies in dystrophic hiPSC-CMs and EHTs.

1.4 Unmet needs

As has been discussed, there currently is no cure for DMD or dystrophic cardiomyopathy. While disease progression in the DMD patient is well described, we ultimately lack a thorough understanding of the importance of dystrophin during cardiac development, and how pleiotropic cellular defects downstream of dystrophin deficiency culminate in organ-level dysfunction and disease. The relative importance of the various roles of dystrophin, i.e., membrane stabilization, calcium regulation, regulation of reactive oxygen species, and mitochondrial regulation, as they relate to disease progression is not well understood. Thus, targets for potential novel therapies are widespread, and progress toward clinical use has been slow.

This progress has been hampered by the shortcomings of common DMD disease models. The *mdx* mouse presents only mild disease phenotypes and little to no signs of cardiomyopathy until much later in their lifespan. Canine models present a more severe disease phenotype, but this phenotype is often extremely variable, and experiments and colony maintenance require considerable financial and temporal resources. The newer *Dmd*^{mdx} rat model appears to offer the disease severity required while still remaining a relatively small animal model; however, experiments still require timepoints of up to twelve months to fully capture disease progression and ultimately, no animal model is able to fully capture human physiology. What's needed is a fully human, preclinical model capable of providing relevant readouts of cardiac function with a fast turnaround time. We propose to address this gap by developing an engineered cardiac model of DMD from human stem cell-derived cardiomyocytes.

In the field of emerging therapies for DMD, AAV-microdystrophin gene replacement therapy is quickly progressing through multiple clinical trials. However, despite the significant contribution of cardiomyopathy to disease morbidity and mortality, comparatively little has been done to assess the effect of these therapies on cardiac function. The lack of this information is in no small part due to shortcomings of commonly used animal models, which require significant

time commitment to expose even a minor cardiac phenotype. Additionally, the seemingly endless microdystrophin designs make it difficult to develop the optimal gene therapy vector. Thus, the development of more suitable in vitro models of dystrophic cardiomyopathy will enable rapid screening and functional evaluation of various microdystrophins as they affect cardiac function.

1.5 Dissertation Specific Aims

Aim 1: To establish a three-dimensional model of Duchenne muscular dystrophy with a robust, multifaceted disease phenotype

Given the lack of cardiac treatments specific to DMD and the shortcomings of animal models commonly used, there is a need to develop human in vitro models of dystrophic cardiomyopathy. Human stem cell-derived models have been shown to replicate a variety of known DMD phenotypes in vitro, but traditional two-dimensional cell culture platforms are limited by cellular immaturity and physiologically irrelevant culture environments and lack relevant functional readouts. More recently, cardiac tissue engineering has produced three-dimensional engineered heart tissue (EHT) models that more accurately recapitulate the native cardiac microenvironment and promote cellular maturation. We hypothesized that hiPSC-CMs generated with a truncating dystrophin mutation cultured as EHTs would promote a robust dystrophic phenotype in vitro. And indeed, we validated that dystrophic EHTs presented many relevant functional deficits, including decreased contractile performance, impaired sarcomere structure, altered calcium transients, and increased beat rate irregularity, as described in Chapter 3. The findings of this study were recently published in a first-author manuscript [202].

Aim 2: To determine the therapeutic effect of microdystrophin gene therapies for Duchenne muscular dystrophy in an in vitro engineered heart tissue model

There have been significant efforts to identify novel, specific therapies to treat DMD. There is great excitement surrounding the development of microdystrophin (μDys) gene therapies;

however, it is not as well understood how these novel proteins will affect cardiac function. Additionally, the need for improved preclinical models has become evident following serious adverse effects reported in multiple clinical trials. Our novel DMD EHTs provide the ideal platform by which to assess the effects of these novel treatments. The development of a miniaturized EHT (mEHT) platform that conforms to a 96-well plate further promises to increase the throughput of the platform. Described in Chapter 4, We have demonstrated that mEHTs are a suitable platform for testing adeno-associated virus (AAV) gene delivery and future studies will assess the effect of AAV-μDys therapies varying in capsid and vector design on dystrophin-null mEHT function.

1.6 References

1. Finsterer J, Stöllberger C (2008) Cardiac involvement in Becker muscular dystrophy. Can J Cardiol 24:786–92

2. Emery AEH (2002) The muscular dystrophies. Lancet (London, England) 359:687–95. https://doi.org/10.1016/S0140-6736(02)07815-7

3. Eagle M, Baudouin S V, Chandler C, et al (2002) Survival in Duchenne muscular dystrophy: improvements in life expectancy since 1967 and the impact of home nocturnal ventilation. Neuromuscul Disord 12:926–9. https://doi.org/10.1016/S0960-8966(02)00140-2

4. Fanchaouy M, Polakova E, Jung C, et al (2009) Pathways of abnormal stress-induced Ca2+ influx into dystrophic mdx cardiomyocytes. Cell Calcium 46:114–121. https://doi.org/10.1016/j.ceca.2009.06.002

5. Rohman MS, Emoto N, Takeshima Y, et al (2003) Decreased mAKAP, ryanodine receptor, and SERCA2a gene expression in mdx hearts. Biochem Biophys Res Commun 310:228–35. https://doi.org/10.1016/J.BBRC.2003.09.005

6. Chang WJ, Iannaccone ST, Lau KS, et al (1996) Neuronal nitric oxide synthase and dystrophin-deficient muscular dystrophy. Proc Natl Acad Sci U S A 93:9142–9147. https://doi.org/10.1073/pnas.93.17.9142

7. Rando TA (2001) Role of nitric oxide in the pathogenesis of muscular dystrophies: A “two hit” hypothesis of the cause of muscle necrosis. Microsc Res Tech 55:223–235. https://doi.org/10.1002/jemt.1172

8. Khairallah M, Khairallah R, Young ME, et al (2007) Metabolic and signaling alterations in dystrophin-deficient hearts precede overt cardiomyopathy. J Mol Cell Cardiol 43:119–129. https://doi.org/10.1016/j.yjmcc.2007.05.015

9. Percival JM, Siegel MP, Knowels G, Marcinek DJ (2013) Defects in mitochondrial localization and ATP synthesis in the mdx mouse model of Duchenne muscular dystrophy are not alleviated by PDE5 inhibition. Hum Mol Genet 22:153–167. https://doi.org/10.1093/hmg/dds415

10. Bushby K, Finkel R, Birnkrant DJ, et al (2010) Diagnosis and management of Duchenne muscular dystrophy, part 1: diagnosis, and pharmacological and psychosocial management. Lancet Neurol 9:77–93. https://doi.org/10.1016/S1474-4422(09)70271-6

11. Spurney CF, Guerron AD, Yu Q, et al (2011) Membrane Sealant Poloxamer P188 Protects Against Isoproterenol Induced Cardiomyopathy in Dystrophin Deficient Mice. BMC Cardiovasc Disord 11:20. https://doi.org/10.1186/1471-2261-11-20

12. Leung DG, Herzka DA, Thompson WR, et al (2014) Sildenafil does not improve cardiomyopathy in Duchenne/Becker muscular dystrophy. Ann Neurol 76:541–549. https://doi.org/10.1002/ana.24214

13. Afzal MZ, Reiter M, Gastonguay C, et al (2016) Nicorandil, a Nitric Oxide Donor and ATP-Sensitive Potassium Channel Opener, Protects Against Dystrophin-Deficient

Cardiomyopathy. J Cardiovasc Pharmacol Ther 21:549–562. https://doi.org/10.1177/1074248416636477

14. Macadangdang JR, Miklas JW, Smith AST, et al (2018) Engineered developmental niche enables predictive phenotypic screening in human dystrophic cardiomyopathy. bioRxiv 456301. https://doi.org/10.1101/456301

15. Spurney CF, Sali A, Guerron AD, et al (2011) Losartan decreases cardiac muscle fibrosis and improves cardiac function in dystrophin-deficient mdx mice. J Cardiovasc Pharmacol Ther 16:87–95. https://doi.org/10.1177/1074248410381757

16. Van Erp C, Irwin NG, Hoey AJ (2006) Long-term administration of pirfenidone improves cardiac function inmdx mice. Muscle Nerve 34:327–334. https://doi.org/10.1002/mus.20590

17. Finkel RS (2010) Read-through strategies for suppression of nonsense mutations in Duchenne/ Becker muscular dystrophy: aminoglycosides and ataluren (PTC124). J Child Neurol 25:1158–64. https://doi.org/10.1177/0883073810371129

18. Hoffman EP, McNally EM (2014) Exon-Skipping Therapy: A Roadblock, Detour, or Bump in the Road? Sci Transl Med 6:230fs14-230fs14. https://doi.org/10.1126/scitranslmed.3008873

19. Chamberlain JR, Chamberlain JS (2017) Progress toward Gene Therapy for Duchenne Muscular Dystrophy. Mol Ther 25:1125–1131

20. Kamdar F, Garry DJ (2016) Dystrophin-Deficient Cardiomyopathy. J Am Coll Cardiol 67:2533–2546. https://doi.org/10.1016/j.jacc.2016.02.081

21. Romfh A, McNally EM (2010) Cardiac Assessment in Duchenne and Becker Muscular Dystrophies. Curr Heart Fail Rep 7:212–218. https://doi.org/10.1007/s11897-010-0028-2

22. Jefferies JL, Eidem BW, Belmont JW, et al (2005) Genetic Predictors and Remodeling of Dilated Cardiomyopathy in Muscular Dystrophy. Circulation 112:2799 LP – 2804

23. Nigro G, Comi LI, Politano L, Bain RJ (1990) The incidence and evolution of cardiomyopathy in Duchenne muscular dystrophy. Int J Cardiol 26:271–7. https://doi.org/10.1016/0167-5273(90)90082-G

24. Konagaya M, Takayanagi T (1986) Regularity in the change of serum creatine kinase level in duchenne muscular dystrophy - A study with long-term follow-up cases. Jpn J Med 25:2–8. https://doi.org/10.2169/internalmedicine1962.25.2

25. Rapezzi C, Leone O, Biagini E, Coccolo F (2007) Echocardiographic clues to diagnosis of dystrophin related dilated cardiomyopathy. Heart 93:10. https://doi.org/10.1136/hrt.2006.087643

26. Thrush PT, Allen HD, Viollet L, Mendell JR (2009) Re-examination of the electrocardiogram in boys with Duchenne muscular dystrophy and correlation with its dilated cardiomyopathy. Am J Cardiol 103:262–5. https://doi.org/10.1016/j.amjcard.2008.08.064

27. Kovick RB, Fogelman AM, Abbasi AD, et al (1975) Echocardiographic evaluation of posterior left ventricular wall motion in muscular dystrophy. Circulation 52:447–54. https://doi.org/10.1161/01.CIR.52.3.447

28. Silva MC, Meira ZMA, Gurgel Giannetti J, et al (2007) Myocardial Delayed Enhancement by Magnetic Resonance Imaging in Patients With Muscular Dystrophy. J Am Coll Cardiol 49:1874–1879. https://doi.org/10.1016/j.jacc.2006.10.078

29. Koenig M, Hoffman EP, Bertelson CJ, et al (1987) Complete cloning of the Duchenne muscular dystrophy (DMD) cDNA and preliminary genomic organization of the DMD gene in normal and affected individuals. Cell 50:509–17. https://doi.org/10.1016/0092-8674(87)90504-6

30. Hoffman EP, Brown RH, Kunkel LM (1987) Dystrophin: the protein product of the Duchenne muscular dystrophy locus. Cell 51:919–28. https://doi.org/10.1016/0092-8674(87)90579-4

31. Ahn AH, Kunkel LM (1993) The structural and functional diversity of dystrophin. Nat Genet 3:283–291. https://doi.org/10.1038/ng0493-283

32. Davies KE, Nowak KJ (2006) Molecular mechanisms of muscular dystrophies: old and new players. Nat Rev Mol Cell Biol 7:762–773. https://doi.org/10.1038/nrm2024

33. Rybakova IN, Patel JR, Ervasti JM (2000) The dystrophin complex forms a mechanically strong link between the sarcolemma and costameric actin. J Cell Biol 150:. https://doi.org/10.1083/JCB.150.5.1209

34. Ehmsen J, Poon E, Davies K (2002) The dystrophin-associated protein complex. J Cell Sci 115:2801 LP – 2803

35. Jung C, Martins AS, Niggli E, Shirokova N (2008) Dystrophic cardiomyopathy: amplification of cellular damage by Ca2+ signalling and reactive oxygen species-generating pathways. Cardiovasc Res 77:766–773. https://doi.org/10.1093/cvr/cvm089

36. Wehrens XHT, Lehnart SE, Reiken SR, Marks AR (2004) Ca2+/Calmodulin-Dependent Protein Kinase II Phosphorylation Regulates the Cardiac Ryanodine Receptor. Circ Res 94:e61–e70. https://doi.org/10.1161/01.RES.0000125626.33738.E2

37. Altamirano F, López JR, Henríquez C, et al (2012) Increased Resting Intracellular Calcium Modulates NF-κB-dependent Inducible Nitric-oxide Synthase Gene Expression in Dystrophic *mdx* Skeletal Myotubes. J Biol Chem 287:20876–20887. https://doi.org/10.1074/jbc.M112.344929

38. Petrof BJ, Shrager JB, Stedman HH, et al (1993) Dystrophin protects the sarcolemma from stresses developed during muscle contraction. Proc Natl Acad Sci U S A 90:3710–4

39. Yasuda S, Townsend D, Michele DE, et al (2005) Dystrophic heart failure blocked by membrane sealant poloxamer. Nature 436:1025–1029. https://doi.org/10.1038/nature03844

40. Youm JB, Han J, Kim N, et al (2005) Role of Stretch-activated Channels in the Heart: Action Potential and Ca(2+) Transients. Academia

41. Ward M-L, Williams IA, Chu Y, et al (2008) Stretch-activated channels in the heart: Contributions to length-dependence and to cardiomyopathy. Prog Biophys Mol Biol 97:232–249. https://doi.org/10.1016/j.pbiomolbio.2008.02.009

42. Lorin C, Vögeli I, Niggli E (2015) Dystrophic cardiomyopathy: role of TRPV2 channels in stretch-induced cell damage. Cardiovasc Res 106:153–162. https://doi.org/10.1093/cvr/cvv021

43. Seo K, Rainer PP, Lee D -i., et al (2014) Hyperactive Adverse Mechanical Stress Responses in Dystrophic Heart Are Coupled to Transient Receptor Potential Canonical 6 and Blocked by cGMP-Protein Kinase G Modulation. Circ Res 114:823–832. https://doi.org/10.1161/CIRCRESAHA.114.302614

44. Catterall WA (2011) Voltage-Gated Calcium Channels. Cold Spring Harb Perspect Biol 3:a003947–a003947. https://doi.org/10.1101/cshperspect.a003947

45. Hohaus A, Person V, Behlke J, et al (2002) The carboxyl-terminal region of ahnak provides a link between cardiac L-type Ca2+ channels and the actin-based cytoskeleton. FASEB J 16:1205–16. https://doi.org/10.1096/fj.01-0855com

46. Bers DM (2002) Cardiac excitation–contraction coupling. Nature 415:198–205. https://doi.org/10.1038/415198a

47. Niggli E, Ullrich ND, Gutierrez D, et al (2013) Posttranslational modifications of cardiac ryanodine receptors: Ca(2+) signaling and EC-coupling. Biochim Biophys Acta 1833:866–

75. https://doi.org/10.1016/j.bbamcr.2012.08.016

48. Shan J, Betzenhauser MJ, Kushnir A, et al (2010) Role of chronic ryanodine receptor phosphorylation in heart failure and β-adrenergic receptor blockade in mice. J Clin Invest 120:4375–4387. https://doi.org/10.1172/JCI37649

49. Kyrychenko S, Poláková E, Kang C, et al (2013) Hierarchical accumulation of RyR post-translational modifications drives disease progression in dystrophic cardiomyopathy. Cardiovasc Res 97:666–675. https://doi.org/10.1093/cvr/cvs425

50. Woodcock EA, Matkovich SJ (2005) Cardiomyocytes structure, function and associated pathologies. Int J Biochem Cell Biol 37:1746–1751. https://doi.org/10.1016/j.biocel.2005.04.011

51. Li Y, Zhang S, Zhang X, et al (2014) Blunted cardiac beta-adrenergic response as an early indication of cardiac dysfunction in Duchenne muscular dystrophy. Cardiovasc Res 103:60–71. https://doi.org/10.1093/cvr/cvu119

52. Zhang YH, Casadei B (2012) Sub-cellular targeting of constitutive NOS in health and disease. J Mol Cell Cardiol 52:341–350. https://doi.org/10.1016/j.yjmcc.2011.09.006

53. van Westering T, Betts C, Wood M (2015) Current Understanding of Molecular Pathology and Treatment of Cardiomyopathy in Duchenne Muscular Dystrophy. Molecules 20:8823–8855. https://doi.org/10.3390/molecules20058823

54. Lai Y, Zhao J, Yue Y, et al (2014) Partial restoration of cardiac function with PDZ nNOS in aged mdx model of Duchenne cardiomyopathy. Hum Mol Genet 23:. https://doi.org/10.1093/hmg/ddu029

55. Zorov DB, Juhaszova M, Sollott SJ (2014) Mitochondrial Reactive Oxygen Species (ROS) and ROS-Induced ROS Release. Physiol Rev 94:909–950. https://doi.org/10.1152/physrev.00026.2013

56. Bernardi P, Lisa F Di (2015) The mitochondrial permeability transition pore: Molecular nature and role as a target in cardioprotection. J Mol Cell Cardiol 78:100–106. https://doi.org/10.1016/j.yjmcc.2014.09.023

57. Guan X, Mack DL, Moreno CM, et al (2014) Dystrophin-deficient cardiomyocytes derived from human urine: New biologic reagents for drug discovery. Stem Cell Res 12:467–480. https://doi.org/10.1016/j.scr.2013.12.004

58. Angelini C (2007) The role of corticosteroids in muscular dystrophy: A critical appraisal. Muscle Nerve 36:424–435. https://doi.org/10.1002/mus.20812

59. Bushby K, Finkel R, Birnkrant DJ, et al (2010) Diagnosis and management of Duchenne muscular dystrophy, part 2: implementation of multidisciplinary care. Lancet Neurol 9:177–89. https://doi.org/10.1016/S1474-4422(09)70272-8

60. Dec GW (2013) Steroid Therapy Effectively Delays Duchenne's Cardiomyopathy. JAC 61:955–956. https://doi.org/10.1016/j.jacc.2012.12.011

61. Allen HD, Flanigan KM, Thrush PT, et al (2013) A randomized, double-blind trial of lisinopril and losartan for the treatment of cardiomyopathy in duchenne muscular dystrophy. PLoS Curr 5:. https://doi.org/10.1371/currents.md.2cc69a1dae4be7dfe2bcb420024ea865

62. Yancy CW, Jessup M, Bozkurt B, et al (2013) 2013 ACCF/AHA Guideline for the Management of Heart Failure: A Report of the American College of Cardiology Foundation/American Heart Association Task Force on Practice Guidelines. Circulation 128:e240–e327. https://doi.org/10.1161/CIR.0b013e31829e8776

63. Kajimoto H, Ishigaki K, Okumura K, et al (2006) Beta-Blocker Therapy for Cardiac Dysfunction in Patients With Muscular Dystrophy. Circ J 70:991–994. https://doi.org/10.1253/circj.70.991

64. Raman S V, Tran TB, Smart SB, et al (2015) Eplerenone for early cardiomyopathy in

Duchenne muscular dystrophy: a randomised, double-blind, placebo-controlled trial. Lancet Neurol 14:153–161. https://doi.org/10.1016/S1474-4422(14)70318-7

65. Wu RS, Gupta S, Brown RN, et al (2010) Clinical outcomes after cardiac transplantation in muscular dystrophy patients. J Hear Lung Transplant 29:432–438. https://doi.org/10.1016/j.healun.2009.08.030

66. Amodeo A, Adorisio R (2012) Left ventricular assist device in Duchenne Cardiomyopathy: Can we change the natural history of cardiac disease? Int J Cardiol 161:e43. https://doi.org/10.1016/j.ijcard.2012.04.009

67. Viollet L, Thrush PT, Flanigan KM, et al (2012) Effects of Angiotensin-Converting Enzyme Inhibitors and/or Beta Blockers on the Cardiomyopathy in Duchenne Muscular Dystrophy. Am J Cardiol 110:98–102. https://doi.org/10.1016/j.amjcard.2012.02.064

68. Adamo CM, Dai D-F, Percival JM, et al (2010) Sildenafil reverses cardiac dysfunction in the mdx mouse model of Duchenne muscular dystrophy. Proc Natl Acad Sci 107:19079–19083. https://doi.org/10.1073/pnas.1013077107

69. Percival JM, Whitehead NP, Adams ME, et al (2012) Sildenafil reduces respiratory muscle weakness and fibrosis in the mdx mouse model of Duchenne muscular dystrophy. J Pathol 228:n/a-n/a. https://doi.org/10.1002/path.4054

70. Sadeghi A, Doyle AD, Johnson BD (2002) Regulation of the cardiac L-type Ca 2+ channel by the actin-binding proteins α-actinin and dystrophin. Am J Physiol Physiol 282:C1502–C1511. https://doi.org/10.1152/ajpcell.00435.2001

71. Koenig X, Rubi L, Obermair GJ, et al (2014) Enhanced currents through L-type calcium channels in cardiomyocytes disturb the electrophysiology of the dystrophic heart. Am J Physiol - Hear Circ Physiol 306:H564. https://doi.org/10.1152/ajpheart.00441.2013

72. Macadangdang J, Guan X, Smith AST, et al (2015) Nanopatterned Human iPSC-Based

Model of a Dystrophin-Null Cardiomyopathic Phenotype. Cell Mol Bioeng 8:320–332. https://doi.org/10.1007/s12195-015-0413-8

73. Flanigan KM, Dunn DM, von Niederhausern A, et al (2009) Mutational Spectrum of DMD Mutations in Dystrophinopathy Patients: Application of Modern Diagnostic Techniques to a Large Cohort. Hum Mutat 30:1657–1666. https://doi.org/10.1002/humu.21114

74. Malik V, Rodino-Klapac LR, Viollet L, et al (2010) Gentamicin-induced readthrough of stop codons in Duchenne muscular dystrophy. Ann Neurol 67:NA-NA. https://doi.org/10.1002/ana.22024

75. Welch EM, Barton ER, Zhuo J, et al (2007) PTC124 targets genetic disorders caused by nonsense mutations. Nature 447:87–91. https://doi.org/10.1038/nature05756

76. Hirawat S, Welch EM, Elfring GL, et al (2007) Safety, Tolerability, and Pharmacokinetics of PTC124, a Nonaminoglycoside Nonsense Mutation Suppressor, Following Single- and Multiple-Dose Administration to Healthy Male and Female Adult Volunteers. J Clin Pharmacol 47:430–444. https://doi.org/10.1177/0091270006297140

77. Finkel RS, Flanigan KM, Wong B, et al (2013) Phase 2a Study of Ataluren-Mediated Dystrophin Production in Patients with Nonsense Mutation Duchenne Muscular Dystrophy. PLoS One 8:e81302. https://doi.org/10.1371/journal.pone.0081302

78. Kayali R, Ku J-M, Khitrov G, et al (2012) Read-through compound 13 restores dystrophin expression and improves muscle function in the mdx mouse model for Duchenne muscular dystrophy. Hum Mol Genet 21:4007–4020. https://doi.org/10.1093/hmg/dds223

79. Cartegni L, Chew SL, Krainer AR (2002) Listening to silence and understanding nonsense: exonic mutations that affect splicing. Nat Rev Genet 3:285–298. https://doi.org/10.1038/nrg775

80. McGreevy JW, Hakim CH, McIntosh MA, Duan D (2015) Animal models of Duchenne

muscular dystrophy: from basic mechanisms to gene therapy. Dis Model Mech 8:195–213. https://doi.org/10.1242/dmm.018424

81. Lim KRQ, Maruyama R, Yokota T (2017) Eteplirsen in the treatment of Duchenne muscular dystrophy. Drug Des Devel Ther 11:533–545

82. Aartsma-Rus A, Krieg AM (2017) FDA Approves Eteplirsen for Duchenne Muscular Dystrophy: The Next Chapter in the Eteplirsen Saga. Nucleic Acid Ther 27:1–3. https://doi.org/10.1089/nat.2016.0657

83. Wu B, Xiao B, Cloer C, et al (2011) One-year Treatment of Morpholino Antisense Oligomer Improves Skeletal and Cardiac Muscle Functions in Dystrophic mdx Mice. Mol Ther 19:576–583. https://doi.org/10.1038/mt.2010.288

84. Chemello F, Bassel-Duby R, Olson EN (2020) Correction of muscular dystrophies by CRISPR gene editing. J Clin Invest 130:2766–2776

85. Amoasii L, Long C, Li H, et al (2017) Single-cut genome editing restores dystrophin expression in a new mouse model of muscular dystrophy. Sci Transl Med 9:. https://doi.org/10.1126/scitranslmed.aan8081

86. Min YL, Li H, Rodriguez-Caycedo C, et al (2019) CRISPR-Cas9 corrects Duchenne muscular dystrophy exon 44 deletion mutations in mice and human cells. Sci Adv 5:eaav4324. https://doi.org/10.1126/sciadv.aav4324

87. Min YL, Chemello F, Li H, et al (2020) Correction of Three Prominent Mutations in Mouse and Human Models of Duchenne Muscular Dystrophy by Single-Cut Genome Editing. Mol Ther 28:2044–2055. https://doi.org/10.1016/j.ymthe.2020.05.024

88. Long C, Amoasii L, Mireault AA, et al (2016) Postnatal genome editing partially restores dystrophin expression in a mouse model of muscular dystrophy. Science (80-) 351:400–403. https://doi.org/10.1126/science.aad5725

89. Young CS, Mokhonova E, Quinonez M, et al (2017) Creation of a Novel Humanized Dystrophic Mouse Model of Duchenne Muscular Dystrophy and Application of a CRISPR/Cas9 Gene Editing Therapy. J Neuromuscul Dis 4:139–145. https://doi.org/10.3233/JND-170218

90. Bengtsson NE, Hall JK, Odom GL, et al (2017) Muscle-specific CRISPR/Cas9 dystrophin gene editing ameliorates pathophysiology in a mouse model for Duchenne muscular dystrophy. Nat Commun 8:1–10. https://doi.org/10.1038/ncomms14454

91. Amoasii L, Hildyard JCW, Li H, et al (2018) Gene editing restores dystrophin expression in a canine model of Duchenne muscular dystrophy. Science (80-) 362:86–91. https://doi.org/10.1126/science.aau1549

92. Young CS, Hicks MR, Ermolova N V., et al (2016) A Single CRISPR-Cas9 Deletion Strategy that Targets the Majority of DMD Patients Restores Dystrophin Function in hiPSC-Derived Muscle Cells. Cell Stem Cell 18:533–540. https://doi.org/10.1016/j.stem.2016.01.021

93. Long C, Li H, Tiburcy M, et al (2018) Correction of diverse muscular dystrophy mutations in human engineered heart muscle by single-site genome editing. Sci Adv 4:eaap9004. https://doi.org/10.1126/sciadv.aap9004

94. Li HL, Fujimoto N, Sasakawa N, et al (2015) Precise correction of the dystrophin gene in duchenne muscular dystrophy patient induced pluripotent stem cells by TALEN and CRISPR-Cas9. Stem cell reports 4:143–54. https://doi.org/10.1016/j.stemcr.2014.10.013

95. Kyrychenko V, Kyrychenko S, Tiburcy M, et al (2017) Functional correction of dystrophin actin binding domain mutations by genome editing. JCI insight 2:. https://doi.org/10.1172/jci.insight.95918

96. Zhang Y, Long C, Li H, et al (2017) CRISPR-Cpf1 correction of muscular dystrophy

mutations in human cardiomyocytes and mice. Sci Adv 3:e1602814. https://doi.org/10.1126/sciadv.1602814

97. Acsadi G, Dickson G, Love DR, et al (1991) Human dystrophin expression in mdx mice after intramuscular injection of DNA constructs. Nature 352:815–818. https://doi.org/10.1038/352815a0

98. Braun S (2004) Naked plasmid DNA for the treatment of muscular dystrophy. Curr Opin Mol Ther 6:499–505

99. Harper SQ, Hauser MA, DelloRusso C, et al (2002) Modular flexibility of dystrophin: Implications for gene therapy of Duchenne muscular dystrophy. Nat Med 8:253–261. https://doi.org/10.1038/nm0302-253

100. Ramos JN, Hollinger K, Bengtsson NE, et al (2019) Development of Novel Micro-dystrophins with Enhanced Functionality. Mol Ther 27:623–635. https://doi.org/10.1016/j.ymthe.2019.01.002

101. Wang B, Li J, Xiao X (2000) Adeno-associated virus vector carrying human minidystrophin genes effectively ameliorates muscular dystrophy in mdx mouse model. Proc Natl Acad Sci 97:13714–13719. https://doi.org/10.1073/pnas.240335297

102. Yuasa K, Miyagoe Y, Yamamoto K, et al (1998) Effective restoration of dystrophin-associated proteins in vivo by adenovirus-mediated transfer of truncated dystrophin cDNAs. FEBS Lett 425:329–336. https://doi.org/10.1016/S0014-5793(98)00251-8

103. Sakamoto M, Yuasa K, Yoshimura M, et al (2002) Micro-dystrophin cDNA ameliorates dystrophic phenotypes when introduced into mdx mice as a transgene. Biochem Biophys Res Commun 293:1265–1272. https://doi.org/10.1016/S0006-291X(02)00362-5

104. Gregorevic P, Allen JM, Minami E, et al (2006) rAAV6-microdystrophin preserves muscle function and extends lifespan in severely dystrophic mice. Nat Med 12:787–789.

https://doi.org/10.1038/nm1439

105. Hakim CH, Wasala NB, Pan X, et al (2017) A Five-Repeat Micro-Dystrophin Gene Ameliorated Dystrophic Phenotype in the Severe DBA/2J-mdx Model of Duchenne Muscular Dystrophy. Mol Ther - Methods Clin Dev 6:216–230. https://doi.org/10.1016/J.OMTM.2017.06.006

106. Yue Y, Li Z, Harper SQ, et al (2003) Microdystrophin Gene Therapy of Cardiomyopathy Restores Dystrophin-Glycoprotein Complex and Improves Sarcolemma Integrity in the Mdx Mouse Heart. Circulation 108:1626–1632. https://doi.org/10.1161/01.CIR.0000089371.11664.27

107. Bostick B, Ghosh A, Yue Y, et al (2007) Systemic AAV-9 transduction in mice is influenced by animal age but not by the route of administration. Gene Ther 14:1605–1609. https://doi.org/10.1038/sj.gt.3303029

108. Pacak CA, Mah CS, Thattaliyath BD, et al (2006) Recombinant Adeno-Associated Virus Serotype 9 Leads to Preferential Cardiac Transduction In Vivo. Circ Res 99:e3–e9. https://doi.org/10.1161/01.RES.0000237661.18885.f6

109. Kornegay JN, Li J, Bogan JR, et al (2010) Widespread Muscle Expression of an AAV9 Human Mini-dystrophin Vector After Intravenous Injection in Neonatal Dystrophin-deficient Dogs. Mol Ther 18:1501–1508. https://doi.org/10.1038/mt.2010.94

110. Lostal W, Kodippili K, Yue Y, Duan D (2014) Full-Length Dystrophin Reconstitution with Adeno-Associated Viral Vectors. Hum Gene Ther 25:552–562. https://doi.org/10.1089/hum.2013.210

111. Koo T, Popplewell L, Athanasopoulos T, Dickson G (2014) Triple Trans-Splicing Adeno-Associated Virus Vectors Capable of Transferring the Coding Sequence for Full-Length Dystrophin Protein into Dystrophic Mice. Hum Gene Ther 25:98–108.

https://doi.org/10.1089/hum.2013.164

112. Phelps SF, Hauser MA, Cole NM, et al (1995) Expression of full-length and truncated dystrophin mini-genes in transgenic mdx mice. Hum Mol Genet 4:1251–8

113. van Putten M, Hulsker M, Young C, et al (2013) Low dystrophin levels increase survival and improve muscle pathology and function in dystrophin/utrophin double-knockout mice. FASEB J 27:2484–2495. https://doi.org/10.1096/fj.12-224170

114. Cox GA, Cole NM, Matsumura K, et al (1993) Overexpression of dystrophin in transgenic mdx mice eliminates dystrophic symptoms without toxicity. Nature 364:725–729. https://doi.org/10.1038/364725a0

115. Townsend D, Yasuda S, Li S, et al (2008) Emergent Dilated Cardiomyopathy Caused by Targeted Repair of Dystrophic Skeletal Muscle. Mol Ther 16:832–835. https://doi.org/10.1038/mt.2008.52

116. Ohshima S, Shin J-H, Yuasa K, et al (2009) Transduction Efficiency and Immune Response Associated With the Administration of AAV8 Vector Into Dog Skeletal Muscle. Mol Ther 17:73–80. https://doi.org/10.1038/mt.2008.225

117. Gussoni E, Soneoka Y, Strickland CD, et al (1999) Dystrophin expression in the mdx mouse restored by stem cell transplantation. Nature 401:390–394. https://doi.org/10.1038/43919

118. Torrente Y, Belicchi M, Marchesi C, et al (2007) Autologous transplantation of muscle-derived CD133+ stem cells in Duchenne muscle patients. Cell Transplant 16:563–577. https://doi.org/10.3727/000000007783465064

119. Goudenege S, Lebel C, Huot NB, et al (2012) Myoblasts Derived From Normal hESCs and Dystrophic hiPSCs Efficiently Fuse With Existing Muscle Fibers Following Transplantation. Mol Ther 20:2153–2167. https://doi.org/10.1038/mt.2012.188

120. Darabi R, Arpke RW, Irion S, et al (2012) Human ES- and iPS-Derived Myogenic Progenitors Restore DYSTROPHIN and Improve Contractility upon Transplantation in Dystrophic Mice. Cell Stem Cell 10:610–619. https://doi.org/10.1016/j.stem.2012.02.015

121. Konieczny P, Swiderski K, Chamberlain JS (2013) Gene and cell-mediated therapies for muscular dystrophy. Muscle Nerve 47:649–663. https://doi.org/10.1002/mus.23738

122. Bulfield G, Siller WG, Wight PAL, Moore KJ (1984) X chromosome-linked muscular dystrophy (mdx) in the mouse. Proc Natl Acad Sci U S A 81:1189–1192. https://doi.org/10.1073/pnas.81.4.1189

123. Pastoret C, Sebille A (1995) mdx mice show progressive weakness and muscle deterioration with age. J Neurol Sci 129:97–105. https://doi.org/10.1016/0022-510X(94)00276-T

124. Chamberlain JS, Metzger J, Reyes M, et al (2007) Dystrophin-deficient mdx mice display a reduced life span and are susceptible to spontaneous rhabdomyosarcoma. FASEB J 21:2195–2204. https://doi.org/10.1096/fj.06-7353com

125. Deconinck AE, Rafael JA, Skinner JA, et al (1997) Utrophin-dystrophin-deficient mice as a model for Duchenne muscular dystrophy. Cell 90:717–27

126. Rooney JE, Welser J V, Dechert MA, et al (2006) Severe muscular dystrophy in mice that lack dystrophin and 7 integrin. J Cell Sci 119:2185–2195. https://doi.org/10.1242/jcs.02952

127. Zhou L, Rafael-Fortney JA, Huang P, et al (2008) Haploinsufficiency of utrophin gene worsens skeletal muscle inflammation and fibrosis in mdx mice. J Neurol Sci 264:106–111. https://doi.org/10.1016/j.jns.2007.08.029

128. Megeney LA, Kablar B, Garrett K, et al (1996) MyoD is required for myogenic stem cell function in adult skeletal muscle. Genes Dev 10:1173–83

129. Sacco A, Mourkioti F, Tran R, et al (2010) Short Telomeres and Stem Cell Exhaustion Model Duchenne Muscular Dystrophy in mdx/mTR Mice. Cell 143:1059–1071. https://doi.org/10.1016/j.cell.2010.11.039

130. Yu X, Bao B, Echigoya Y, Yokota T (2015) Dystrophin-deficient large animal models: translational research and exon skipping. Am J Transl Res 7:1314–31

131. Valentine BA, Cooper BJ, de Lahunta A, et al (1988) Canine X-linked muscular dystrophy. An animal model of Duchenne muscular dystrophy: clinical studies. J Neurol Sci 88:69–81

132. West NA, Yang ML, Weitzenkamp DA, et al (2013) Patterns of Growth in Ambulatory Males with Duchenne Muscular Dystrophy. J Pediatr 163:1759-1763.e1. https://doi.org/10.1016/j.jpeds.2013.08.004

133. Larcher T, Lafoux A, Tesson L, et al (2014) Characterization of Dystrophin Deficient Rats: A New Model for Duchenne Muscular Dystrophy. PLoS One 9:e110371. https://doi.org/10.1371/journal.pone.0110371

134. Takahashi K, Yamanaka S (2006) Induction of pluripotent stem cells from mouse embryonic and adult fibroblast cultures by defined factors. Cell 126:663–676. https://doi.org/10.1016/j.cell.2006.07.024

135. Lian X, Hsiao C, Wilson G, et al (2012) Robust cardiomyocyte differentiation from human pluripotent stem cells via temporal modulation of canonical Wnt signaling. Proc Natl Acad Sci U S A 109:. https://doi.org/10.1073/pnas.1200250109

136. Park I-H, Arora N, Huo H, et al (2008) Disease-Specific Induced Pluripotent Stem Cells. Cell 134:877–886. https://doi.org/10.1016/j.cell.2008.07.041

137. Pioner JM, Fornaro A, Coppini R, et al (2020) Advances in Stem Cell Modeling of Dystrophin-Associated Disease : Implications for the Wider World of Dilated Cardiomyopathy. Front Physiol 11:368. https://doi.org/10.3389/fphys.2020.00368

138. Farini A, Gowran A, Bella P, et al (2019) Fibrosis Rescue Improves Cardiac Function in Dystrophin-Deficient Mice and Duchenne Patient–Specific Cardiomyocytes by Immunoproteasome Modulation. Am J Pathol 189:339–353. https://doi.org/10.1016/j.ajpath.2018.10.010

139. Lin B, Li Y, Han LL, et al (2015) Modeling and study of the mechanism of dilated cardiomyopathy using induced pluripotent stem cells derived from individuals with Duchenne muscular dystrophy. Dis Model Mech 8:457–466. https://doi.org/10.1242/dmm.019505

140. Sato M, Shiba N, Miyazaki D, et al (2019) Amelioration of intracellular Ca2+ regulation by exon-45 skipping in Duchenne muscular dystrophy-induced pluripotent stem cell-derived cardiomyocytes. Biochem Biophys Res Commun 520:179–185. https://doi.org/10.1016/j.bbrc.2019.09.095

141. Eisen B, Ben Jehuda R, Cuttitta AJ, et al (2019) Electrophysiological abnormalities in induced pluripotent stem cell-derived cardiomyocytes generated from Duchenne muscular dystrophy patients. J Cell Mol Med 23:2125–2135. https://doi.org/10.1111/jcmm.14124

142. Caluori G, Pribyl J, Pesl M, et al (2019) Non-invasive electromechanical cell-based biosensors for improved investigation of 3D cardiac models. Biosens Bioelectron 124–125:129–135. https://doi.org/10.1016/j.bios.2018.10.021

143. Moretti A, Fonteyne L, Giesert F, et al (2020) Somatic gene editing ameliorates skeletal and cardiac muscle failure in pig and human models of Duchenne muscular dystrophy. Nat Med 26:207–214. https://doi.org/10.1038/s41591-019-0738-2

144. Jelinkova S, Fojtik P, Kohutova A, et al (2019) Dystrophin Deficiency Leads to Genomic Instability in Human Pluripotent Stem Cells via NO Synthase-Induced Oxidative Stress. Cells 8:53. https://doi.org/10.3390/cells8010053

145. Gartz M, Darlington A, Afzal MZ, Strande JL (2018) Exosomes exert cardioprotection in dystrophin-deficient cardiomyocytes via ERK1/2-p38/MAPK signaling. Sci Rep 8:1–14. https://doi.org/10.1038/s41598-018-34879-6

146. Dick E, Kalra S, Anderson D, et al (2013) Exon skipping and gene transfer restore dystrophin expression in human induced pluripotent stem cells-cardiomyocytes harboring dmd mutations. Stem Cells Dev 22:2714–2724. https://doi.org/10.1089/scd.2013.0135

147. Pioner JM, Guan X, Klaiman JM, et al (2019) Absence of full-length dystrophin impairs normal maturation and contraction of cardiomyocytes derived from human-induced pluripotent stem cells. Cardiovasc Res 116:368–382. https://doi.org/10.1093/cvr/cvz109

148. Van Den Berg CW, Okawa S, Chuva De Sousa Lopes SM, et al (2015) Transcriptome of human foetal heart compared with cardiomyocytes from pluripotent stem cells. Dev 142:3231–3238. https://doi.org/10.1242/dev.123810

149. Davis RP, van den Berg CW, Casini S, et al (2011) Pluripotent stem cell models of cardiac disease and their implication for drug discovery and development. Trends Mol Med 17:475–484

150. Ulmer BM, Eschenhagen T (2020) Human pluripotent stem cell-derived cardiomyocytes for studying energy metabolism. Biochim Biophys Acta - Mol Cell Res 1867:118471

151. Pioner JM, Racca AW, Klaiman JM, et al (2016) Isolation and mechanical measurements of myofibrils from human induced pluripotent stem cell-derived cardiomyocytes. Stem Cell Reports 6:885–896. https://doi.org/10.1016/j.stemcr.2016.04.006

152. Scuderi GJ, Butcher J (2017) Naturally Engineered Maturation of Cardiomyocytes. Front Cell Dev Biol 5:1–28. https://doi.org/10.3389/fcell.2017.00050

153. Smith AST, Macadangdang J, Leung W, et al (2017) Human iPSC-derived cardiomyocytes and tissue engineering strategies for disease modeling and drug screening. Biotechnol Adv

35:77–94

154. Ahmed RE, Anzai T, Chanthra N, Uosaki H (2020) A Brief Review of Current Maturation Methods for Human Induced Pluripotent Stem Cells-Derived Cardiomyocytes. Front Cell Dev Biol 8:178

155. Martewicz S, Serena E, Zatti S, et al (2017) Substrate and mechanotransduction influence SERCA2a localization in human pluripotent stem cell-derived cardiomyocytes affecting functional performance. Stem Cell Res 25:107–114. https://doi.org/10.1016/j.scr.2017.10.011

156. Feaster TK, Cadar AG, Wang L, et al (2015) A method for the generation of single contracting human-induced pluripotent stem cell-derived cardiomyocytes. Circ Res 117:995–1000. https://doi.org/10.1161/CIRCRESAHA.115.307580

157. Herron TJ, Da Rocha AM, Campbell KF, et al (2016) Extracellular matrix-mediated maturation of human pluripotent stem cell-derived cardiac monolayer structure and electrophysiological function. Circ Arrhythmia Electrophysiol 9:. https://doi.org/10.1161/CIRCEP.113.003638

158. Ribeiro AJS, Ang YS, Fu JD, et al (2015) Contractility of Single cardiomyocytes differentiated from pluripotent stem cells depends on physiological shape and substrate stiffness. Proc Natl Acad Sci U S A 112:12705–12710. https://doi.org/10.1073/pnas.1508073112

159. Rao C, Prodromakis T, Kolker L, et al (2013) The effect of microgrooved culture substrates on calcium cycling of cardiac myocytes derived from human induced pluripotent stem cells. Biomaterials 34:2399–2411. https://doi.org/10.1016/j.biomaterials.2012.11.055

160. McDevitt TC, Angello JC, Whitney ML, et al (2002) In vitro generation of differentiated cardiac myofibers on micropatterned laminin surfaces. J Biomed Mater Res 60:472–479.

https://doi.org/10.1002/jbm.1292

161. Yang X, Rodriguez M, Pabon L, et al (2014) Tri-iodo-l-thyronine promotes the maturation of human cardiomyocytes-derived from induced pluripotent stem cells. J Mol Cell Cardiol 72:296–304. https://doi.org/10.1016/j.yjmcc.2014.04.005

162. Nakano H, Minami I, Braas D, et al (2017) Glucose inhibits cardiac muscle maturation through nucleotide biosynthesis. Elife 6:. https://doi.org/10.7554/eLife.29330

163. Horikoshi Y, Yan Y, Terashvili M, et al (2019) Fatty Acid-Treated Induced Pluripotent Stem Cell-Derived Human Cardiomyocytes Exhibit Adult Cardiomyocyte-Like Energy Metabolism Phenotypes. Cells 8:1095. https://doi.org/10.3390/cells8091095

164. Yang X, Rodriguez ML, Leonard A, et al (2019) Fatty acids enhance the maturation of cardiomyocytes derived from human pluripotent stem cells. Stem Cell Reports 13:657–668. https://doi.org/10.1016/j.stemcr.2019.08.013

165. Dunn KK, Reichardt IM, Simmons AD, et al (2019) Coculture of Endothelial Cells with Human Pluripotent Stem Cell-Derived Cardiac Progenitors Reveals a Differentiation Stage-Specific Enhancement of Cardiomyocyte Maturation. Biotechnol J 14:. https://doi.org/10.1002/biot.201800725

166. Abecasis B, Gomes-Alves P, Rosa S, et al (2019) Unveiling the molecular crosstalk in a human induced pluripotent stem cell-derived cardiac model. Biotechnol Bioeng 116:1245–1252. https://doi.org/10.1002/bit.26929

167. Yoshida S, Miyagawa S, Fukushima S, et al (2018) Maturation of Human Induced Pluripotent Stem Cell-Derived Cardiomyocytes by Soluble Factors from Human Mesenchymal Stem Cells. Mol Ther 26:2681–2695. https://doi.org/10.1016/j.ymthe.2018.08.012

168. Kroll K, Chabria M, Wang K, et al (2017) Electro-mechanical conditioning of human iPSC-

derived cardiomyocytes for translational research. Prog Biophys Mol Biol 130:212–222. https://doi.org/10.1016/j.pbiomolbio.2017.07.003

169. Chan YC, Ting S, Lee YK, et al (2013) Electrical stimulation promotes maturation of cardiomyocytes derived from human embryonic stem cells. J Cardiovasc Transl Res 6:989–999. https://doi.org/10.1007/s12265-013-9510-z

170. Bremner SB, Gaffney KS, Sniadecki NJ, Mack DL (2022) A Change of Heart: Human Cardiac Tissue Engineering as a Platform for Drug Development. Curr Cardiol Rep 1:1–14

171. Schaaf S, Eder A, Vollert I, et al (2014) Generation of Strip-Format Fibrin-Based Engineered Heart Tissue (EHT). Methods Mol Biol 1181:121–129. https://doi.org/10.1007/978-1-4939-1047-2

172. Polonchuk L, Chabria M, Badi L, et al (2017) Cardiac spheroids as promising in vitro models to study the human heart microenvironment. Sci Rep 7:1–12. https://doi.org/10.1038/s41598-017-06385-8

173. Kelm JM, Ehler E, Nielsen LK, et al (2004) Design of Artificial Myocardial Microtissues. Tissue Eng 10:201–214. https://doi.org/10.1089/107632704322791853

174. Boudou T, Legant WR, Mu A, et al (2012) A microfabricated platform to measure and manipulate the mechanics of engineered cardiac microtissues. Tissue Eng - Part A 18:910–919. https://doi.org/10.1089/ten.tea.2011.0341

175. Huebsch N, Loskill P, Deveshwar N, et al (2016) Miniaturized iPS-Cell-Derived Cardiac Muscles for Physiologically Relevant Drug Response Analyses. Sci Rep 6:1–12. https://doi.org/10.1038/srep24726

176. Hansen A, Eder A, Bönstrup M, et al (2010) Development of a drug screening platform based on engineered heart tissue. Circ Res 107:35–44. https://doi.org/10.1161/CIRCRESAHA.109.211458

177. Zimmermann WH, Schneiderbanger K, Schubert P, et al (2002) Tissue engineering of a differentiated cardiac muscle construct. Circ Res 90:223–230. https://doi.org/10.1161/hh0202.103644

178. Nunes SS, Miklas JW, Liu J, et al (2013) Biowire: A platform for maturation of human pluripotent stem cell-derived cardiomyocytes. Nat Methods 10:781–787. https://doi.org/10.1038/nmeth.2524

179. Feric NT, Pallotta I, Singh R, et al (2019) Engineered cardiac tissues generated in the Biowire II: A platform for human-based drug discovery. Toxicol Sci 172:89–97. https://doi.org/10.1093/toxsci/kfz168

180. Eschenhagen T, Fink C, Remmers U, et al (1997) Three-dimensional reconstitution of embryonic cardiomyocytes in a collagen matrix: a new heart muscle model system. FASEB J 11:683–694. https://doi.org/10.1096/fasebj.11.8.9240969

181. Jackman CP, Carlson AL, Bursac N (2016) Dynamic culture yields engineered myocardium with near-adult functional output. Biomaterials 111:66–79. https://doi.org/10.1016/j.biomaterials.2016.09.024

182. Bian W, Jackman CP, Bursac N (2014) Controlling the structural and functional anisotropy of engineered cardiac tissues. Biofabrication 6:024109. https://doi.org/10.1088/1758-5082/6/2/024109

183. Leonard A, Bertero A, Powers JD, et al (2018) Afterload promotes maturation of human induced pluripotent stem cell derived cardiomyocytes in engineered heart tissues. J Mol Cell Cardiol 118:147–158. https://doi.org/10.1016/j.yjmcc.2018.03.016

184. Bielawski KS, Leonard A, Bhandari S, et al (2016) Real-rime force and frequency analysis of engineered human heart tissue derived from induced pluripotent stem cells using magnetic sensing. Tissue Eng Part C 22:932–940.

https://doi.org/10.1089/ten.tec.2016.0257

185. Bremner SB, Goldstein AJ, Higashi T, Sniadecki NJ (2022) Engineered Heart Tissues for Contractile, Structural, and Transcriptional Assessment of Human Pluripotent Stem Cell-Derived Cardiomyocytes in a Three-Dimensional, Auxotonic Environment. In: Coulombe KLK, Black LD (eds) Cardiac Tissue Engineering: Methods and Protocols, 2nd ed. Springer US, New York, NY, United States

186. Zaunbrecher RJ, Abel AN, Beussman K, et al (2019) Cronos Titin Is Expressed in Human Cardiomyocytes and Necessary for Normal Sarcomere Function. Circulation 140:1647–1660. https://doi.org/10.1161/CIRCULATIONAHA.119.039521

187. Bertero A, Fields PA, Smith AST, et al (2019) Chromatin compartment dynamics in a haploinsufficient model of cardiac laminopathy. J Cell Biol 218:2919–2944. https://doi.org/10.1083/jcb.201902117

188. Tsui JH, Leonard A, Camp ND, et al (2021) Tunable electroconductive decellularized extracellular matrix hydrogels for engineering human cardiac microphysiological systems. Biomaterials 272:120764. https://doi.org/10.1016/j.biomaterials.2021.120764

189. Mihic A, Li J, Miyagi Y, et al (2014) The effect of cyclic stretch on maturation and 3D tissue formation of human embryonic stem cell-derived cardiomyocytes. Biomaterials 35:2798–2808. https://doi.org/10.1016/j.biomaterials.2013.12.052

190. Ruan J-LL, Tulloch NL, Razumova M V., et al (2016) Mechanical stress conditioning and electrical stimulation promote contractility and force maturation of induced pluripotent stem cell-derived human cardiac tissue. Circulation 134:1557–1567. https://doi.org/10.1161/CIRCULATIONAHA.114.014998

191. Ruan JL, Tulloch NL, Saiget M, et al (2015) Mechanical stress promotes maturation of human myocardium from pluripotent stem cell-derived progenitors. Stem Cells 33:2148–

2157. https://doi.org/10.1002/stem.2036

192. Abilez OJ, Tzatzalos E, Yang H, et al (2018) Passive stretch induces structural and functional maturation of engineered heart muscle as predicted by computational modeling. Stem Cells 36:265–277. https://doi.org/10.1002/stem.2732

193. Shimko VF, Claycomb WC (2008) Effect of mechanical loading on three-dimensional cultures of embryonic stem cell-derived cardiomyocytes. Tissue Eng - Part A 14:49–58. https://doi.org/10.1089/ten.a.2007.0092

194. Schroer A, Pardon G, Castillo E, et al Engineering hiPSC cardiomyocyte in vitro model systems for functional and structural assessment. https://doi.org/10.1016/j.pbiomolbio.2018.12.001

195. Ronaldson-Bouchard K, Ma SP, Yeager K, et al (2018) Advanced maturation of human cardiac tissue grown from pluripotent stem cells. Nature 556:239–243. https://doi.org/10.1038/s41586-018-0016-3

196. Bliley JM, Vermeer MCSC, Duffy RM, et al (2020) Dynamic loading of human engineered heart tissue enhances contractile function and drives desmosome-linked disease phenotype. bioRxiv. https://doi.org/10.1101/2020.05.25.111690

197. Lu K, Seidel T, Cao-Ehlker X, et al (2021) Progressive stretch enhances growth and maturation of 3D stem-cell-derived myocardium. 11:13. https://doi.org/10.7150/thno.54999

198. Eschenhagen T, Mummery C, Knollmann BC (2015) Modelling sarcomeric cardiomyopathies in the dish: From human heart samples to iPSC cardiomyocytes. Cardiovasc Res 105:424–438

199. Sharma A, Sances S, Workman MJ, Svendsen CN (2020) Multi-lineage Human iPSC-Derived Platforms for Disease Modeling and Drug Discovery. Cell Stem Cell 26:309–329

200. Goldfracht I, Efraim Y, Shinnawi R, et al (2019) Engineered heart tissue models from hiPSC-derived cardiomyocytes and cardiac ECM for disease modeling and drug testing applications. Acta Biomater 92:145–159

201. Hoes MF, Bomer N, van der Meer P (2019) Concise review: The current state of human in vitro cardiac disease modeling: A focus on gene editing and tissue engineering. Stem Cells Transl Med 8:66–74. https://doi.org/10.1002/sctm.18-0052

202. Bremner SB, Mandrycky CJ, Leonard A, et al (2022) Full-length dystrophin deficiency leads to contractile and calcium transient defects in human engineered heart tissues. J Tissue Eng 13:1–16. https://doi.org/10.1177/20417314221119628

Chapter 2. Human Engineered Heart Tissues as a Platform for Drug Screening

The contents of this chapter were published as the following first-author review paper:

S.B. Bremner, K.S. Gaffney, N.J. Sniadecki, D.L. Mack. A change of heart: human cardiac tissue engineering as a platform for drug development. *Current Cardiology Reports.* 2022:1. DOI: 10.1007/s11886-022-01668-7.

2.1 Abstract

Human cardiac tissue engineering holds great promise for early detection of drug-related cardiac toxicity and arrhythmogenicity during drug discovery and development. We describe shortcomings of the current drug development pathway, recent advances in the development of cardiac tissue constructs as drug testing platforms, and the challenges remaining in their widespread adoption. Human pluripotent stem cell-derived cardiomyocytes (hPSC-CMs) have been used to develop a variety of constructs including cardiac spheroids, microtissues, strips, rings, and chambers. Several ambitious studies have used these constructs to test a significant number of drugs, and while most have shown proper negative inotropic and arrhythmogenic responses, few have been able to demonstrate positive inotropy, indicative of relative hPSC-CM immaturity. Several engineered human cardiac tissue platforms have demonstrated native cardiac physiology and proper drug responses. Future studies addressing hPSC-CM immaturity and inclusion of patient-specific cell lines will further advance the utility of such models for *in vitro* drug development.

2.2 Introduction

The current drug development pathway is exorbitantly expensive and time-consuming. It is estimated that between 2009 and 2018, the median cost to bring a new drug to market was

$985.3 million, including capitalized research and development investment costs [1]. This figure includes the cost of failed trials, as it has been reported that the approval rate for drugs entering phase 1 trials is only 13.8% [2]. Even having reached later phases of clinical trials, it is unfortunately common for drugs to fail due to lack of efficacy or unanticipated adverse effects, regardless of the promise shown in preclinical studies [3]. In a large part, this is due to limitations of animal models and *in vitro* preclinical models that limit our ability to accurately predict drug performance in human patients [4,5]. Additionally, many pharmaceutical companies opt to embrace a fail early, fail fast strategy where the vast majority of drug candidates are eliminated early in the process to avoid costly late-stage failures, thus possibly missing potentially life-saving drugs [6]. In light of this, it is necessary that we re-evaluate the preclinical drug discovery and testing paradigm to make drug development more efficient and cost effective.

The shortcomings of the canonical drug development process are perhaps most evident when considering cardiac effects, as side effects such as cardiac toxicity and arrhythmogenicity are the most common reasons for late-stage drug failure or drug withdrawal [7,8]. To address this, regulatory agencies require specific cardiotoxicity screening; however, the methods employed lack the relevance to the human cardiovascular system needed to accurately predict cardiac effects. The more simple *in vitro* models rely on non-cardiac cell lines that express a recombinant human *ether-á-go-go* related gene (hERG) potassium channel, as this channel plays a major role in cardiac repolarization and hERG-blocking compounds frequently cause ventricular arrhythmias [9,10]. While useful in some cases, these simple, *in vitro* models are unable to model the interactions of multiple ion channels and the compensatory mechanisms present in the native myocardium. Increasing in complexity, rodent models are frequently used due to their relative low costs and short experimental timelines. However, these models often produce irrelevant results due to distinct physiological differences between human and rodent cardiovascular biology [5,11]. While larger animal models can yield more relevant results, the costs and resources required for

colony maintenance and ethical concerns are often prohibitive [12]. Thus, there exists a need to develop improved human *in vitro* cardiac models for drug screening and development.

The human heart is the ideal platform for drug testing; however, the limited availability and inadequate *ex vivo* viability of primary samples prevents their widespread use. Consequently, the development of human pluripotent stem cells (hPSCs, either embryonic stem cells, hESCs, or induced pluripotent stem cells, hiPSCs) and hPSC-derived cardiomyocytes (hPSC-CMs) holds great promise for advancing drug development platforms [13–16]. To date, hPSC-CMs have been shown to express key cardiomyocyte structural and signaling elements and faithfully recapitulate human cardiac biology, leading to their widespread use in studies demonstrating typical responses to drug compounds. However, hPSC-CMs are limited in their relative immaturity as compared to adult cardiomyocytes, as hPSC-CMs have been shown to more closely resemble fetal cardiomyocytes with regard to transcriptional activity, ultrastructure, and function, limiting their utility as a preclinical drug screening model [17–19]. Thus, several approaches have been employed to improve hPSC-CM maturity, including increased time in culture, topographical cues, biochemical stimuli, and the development of three-dimensional engineered models [20].

Human engineered cardiac tissues can be broadly defined as multicellular aggregates made from hPSC-CMs, often accompanied by other cell types, with or without the presence of extracellular matrix protein scaffolds. Such engineered constructs more closely mimic the native myocardium by recapitulating key cell-cell and cell-matrix biology that has been shown to further advance hPSC-CM maturation and facilitate key measures of cardiac function such as force production and voltage propagation [21–25]. These tissue constructs come in many shapes and sizes ranging from scaffold-free spheroids amenable to high throughput screening to larger engineered chambers capable of generating pressure-volume loops. In recognition of the promise of these cardiac constructs to improve our ability to model cardiomyopathy and drug responses *in vitro*, research groups have developed various platforms, and many have moved toward

commercialization. This review describes the newest advances made in the development of engineered cardiac constructs as valid platforms for preclinical drug screening and the remaining challenges preventing widespread adoption of these platforms.

2.3 Engineered cardiac platforms for drug screening

As a category, engineered cardiac tissues have come to include any cell culture platform facilitating multicellular, three-dimensional culture of synchronously contracting hPSC-CMs. As such, these platforms take many forms that vary widely in geometry and scale, the inclusion of non-myocytes, and the presence of scaffold proteins. Broadly, those on the smaller scale such as spheroids and microtissues more easily facilitate high-throughput cardiotoxicity screening while retaining some aspects of cardiac function, whereas larger platforms including cardiac sheets, strips, rings, and chambers are more suited to lower-throughput assessment of drug effect on cardiac function, as they more closely resemble native cardiac tissue and enable measurement of voltage propagation and force generation (**Fig 2.1**). In the following sections, we have categorized these platforms broadly by geometry as a means to discuss their advantages and limitations as platforms for drug testing and progress made toward drug screening applications. Details describing the various platforms and findings from recent drug screening studies are summarized in **Table 2.1**.

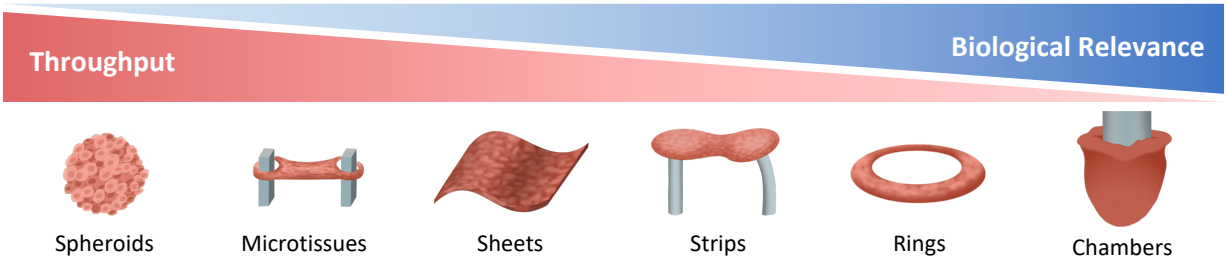

	Spheroids	Microtissues	Sheets	Strips	Rings	Chambers
Advantages	Readouts for **cell viability, apoptosis, motion analysis** Simple setup, automated seeding and analysis	Readouts for **contraction force, cell viability, apoptosis** Anisotropic organization, automated seeding and analysis, non-invasive force measurement	Readouts for **optical mapping, motion analysis, Ca^{2+} transients** Larger surface area for optical mapping, amenable to electrical stimulation	Readouts for **contraction force, optical mapping, Ca^{2+} transients** Non-invasive force measurement, anisotropic organization, amenable to electrical stimulation	Readouts for **optical mapping, Ca^{2+} transients, contraction force** Anisotropic organization, larger surface area for optical mapping, amenable to electrical stimulation	Readouts for **pressure-volume loops, optical mapping, Ca^{2+} transients** Clinically-relevant readouts, amenable to electrical stimulation
Limitations	No direct force measurement, isotropic organization	Requires specialized culture platforms, too small for optical mapping	No direct force measurement, anisotropic organization requires patterning	Potential for drug absorption by silicone posts	Direct force measurement requires force transducer, requires manual handling	Labor-intensive, requires specialized equipment

Figure 2.1. Different engineered cardiac tissue platforms organized by relative throughput and biological relevance with a description of their advantages and limitations.

Table 2.1. Summary of drug screening studies in human engineered cardiac tissues.

Construct type	Cell types	Cells per hEHT	Scaffold material	Compounds tested & dosage			Readouts	Ref.
Spheroid	hiPSC-CM HCAEC iPSC-CF	1.2×10^4	Scaffold-free	Doxorubicin L-NIO	1–40 µM 100 µM		• Cell viability • Apoptosis	[32]
Spheroid	hiPSC-CM hCMEC hCF	5×10^2	Scaffold-free	Acyclovir Amiodarone Amphotericin B Bortezomib Buspirone Cisapride Clozapine Cyclophosphamide Dasatinib Donepezil Doxorubicin Erlotinib Fluorouracil Gemfibrozil Idarubicin	0.3–100 µM 0.2–50 µM 0.2–50 µM 0.3–100 µM 0.3–100 µM 0.3–100 µM 0.3–100 µM 0.3–100 µM 0.3–100 µM 0–30 µM 0.2–50 µM 0–30 µM 0.3–100 µM 0.3–100 µM 0.3–100 µM	Imatinib Isoproterenol Ketoprofen Lapatinib Mebendazole Methapyrilene Minoxidil Mitoxantrone Naringenin Nifedipine Praziquantel Sorafenib Sunitinib Terfenadine	0.2–50 µM 0.3–100 µM 0.3–100 µM 0.3–100 µM 0.2–50 µM 0.3–100 µM 0.2–50 µM 0.3–100 µM 0.3–100 µM 0.3–100 µM 0.3–100 µM 0.3–100 µM 0.1–30 µM 0.3–100 µM	• Cellular viability • Mitochondrial membrane potential • Endoplasmic reticulum integrity	[33•]
Fibrotic spheroid	hESC-CM hESC-MSC	5×10^4	Scaffold-free	Aldosterone Bisphenol A Metoprolol	10 µM 10 µM 10 µM		• Collagen deposition • Apoptosis • Mitochondrial morphology	[31]
Ischemic spheroid	hiPSC-CM NHCF HUVEC hADSC	4.3×10^4	Scaffold-free	Doxycycline JQ1	0.1–50 µM 10 nM		• Contraction amplitude • Apoptosis	[35]
Spheroid	hiPSC-CM hCF	$1.2–2.4 \times 10^4$	Scaffold-free	4-Aminopyridine BayK8644 BPA	50 mM 300 nM 1–1000 nM	E4031 Isoproterenol Ranolazine	2 µM 100 nM 2–100 µM	• Optical mapping of membrane potential	[34]
3D printed spheroid array	hiPSC-CM HUVEC NHDF	3.5×10^4 per spheroid 500 spheroids per tissue	Scaffold-free	Blebbistatin Doxorubicin Isoproterenol Propranolol	500 nM 10 µM 1 µM 5 µM			• Contraction amplitude and kinetics • Cell viability	[36]
Microtissue strip	hiPSC-CM	$0.9–1.8 \times 10^6$	Scaffold-free	Ampicillin E4031 Erythromycin Metformin Rosiglitazone	0.01 µM–1 mM 0.001–10 µM 0.01–500 µM 0.01–1 mM 0.001–200 µM	Tamoxifen Troglitazone Trovafloxacin Vandetanib	0.001–200 µM 0.01–200 µM 0.01–200 µM 0.001–100 µM	• Contraction amplitude • Beating rate • Cell viability	[38]

Microtissue strip	hiPSC–CM hMSC	5×10^2	Collagen I	Sunitinib	1–10 μM			• Apoptosis • Beating rate	[41]
Microtissue strip	hESC-CM	5×10^4	Collagen I Matrigel	105 compounds	0.1–10 μM			• Contraction amplitude • Proliferation	[42•]
Microtissue ring	hESC-CM hCF	7.5×10^4	Collagen I	Blebbistatin Isoproterenol	1 nM–10 μM 10 nM–1 μM	Nifedipine	1 nM–10 μM	• Contraction amplitude	[37]
Anisotropic cell sheet	hESC-CM	2.5×10^5 cm^{-1}	Scaffold-free	Aspirin Cisapride Flecainide	3–30 μM 30–300 nM 0.3–3 μM	Procainamide Terfenadine Tocainide	30–300 μM 30-300 nM 10–100 μM	• Action potential kinetics	[43]
Layered cell sheet	hiPSC-CM NHCF HMVEC	1×10^6	Fibronectin Gelatin	E-4031 Isoproterenol	1–100 nM 1–1000 nM			• Beating rate • Contraction kinetics	[45]
Layered cell sheet	hiPSC-CM NHCF HMVEC	1.1×10^6	Fibronectin Gelatin	Chromanol 293B Dobutamine E-4031 Flecainide Glibenclamide	1–30 nM 3–100 μM 3–30 nM 30–1000 nM 1–30 μM	Isoproterenol Milrinone Ouabain Pimobendan Verapamil	1–1000 nM 3–100 μM 3–30 nM 0.1–3 μM 3–100 nN	• Beating rate • Contraction kinetics • Contraction amplitude	[44]
Tissue strip	hiPSC-CM HS27a	5.5×10^5	Fibrin	Isoproterenol Verapamil	0.05–50 μM 0.5–50 μM			• Beat Rate • Contraction force	[58]
Tissue strip	hiPSC-CM	1×10^6	Matrigel Fibrin	Aspirin Citalopram Digoxin Isoproterenol Formoterol Lidocaine	0.1–30 μM 0.1–30 μM 0.1–30 μM 3–300 nM 0.01–3 μM 0.1–30 μM	Milrinone Nifedipine Rolipram Ryanodine Tacrolimus	0.1–30 μM 0.1–30 μM 0.1–30 μM 0.1–30 μM 0.1–30 μM	• Contraction force • Contraction kinetics	[50]
Tissue strip	hPSC-CM	1×10^6	Matrigel Fibrin	BayK-8644 Digoxin EMD-57033 Isoproterenol	3–300 nM 0.01-1 μM 0.1–10 μM 0.3–100 nM	Nifedipine Ryanodine Thapsigargin	3–1000 nM 1–30 μM 3–300 μM	• Contraction force • Contraction kinetics	[78]
Atrial tissue strip	hiPSC-CM	1×10^6	Fibrin	4-AP CCh	50 μM 10 μM			• Action potential amplitude and kinetics	[54]
Tissue strip	hiPSC-CM NHDF	2×10^6	Fibrin	Isoproterenol	0.01 nM–1 mM			• Beat rate • Contraction force	[52•]

Tissue strip (Biowire)	hiPSC-CM NHCF	1.1×10^5	Fibrin Collagen Matrigel	Digoxin Dobutamine Endothelin-1 FPL64176 Isoproterenol Levosimendan	0.1 nM–100 μM 0.003 nM–3 μM 0.0004–40 nM 0.1 nM–30 μM 1 pM–10 μM 0.2 nM–20 μM	Mavacamten Milrinone Nifedipine Omecamtiv PACAP27 Thapsigargin	0.1 nM–100 μM 1 nM–300 μM 0.01 nM–10 μM 1 nM–10 μM 0.001–300 nM 0.1 nM–30 μM	• Contraction force	[49]
Atrial and ventricular tissue strip (Biowire)	hESC-CM NHCF	1.1×10^5	Collagen Matrigel	4-AP Carbachol Diltiazem Dofetilide E4031 Isoproterenol	25–50 μM 1 μM 10–20 μM 10–1000 nM 0.01 nM 0.1–10 nM	Lidocaine Milrinone Nifedipine Serotonin Thapsigargin Verapamil	10–20 μM 0.08–20 μM 0.01–10 μM 0.01–1 μM 5–50 μM 0.1–10 μM	• Action potential amplitude and kinetics • Contraction force • Ca^{2+} transients	[53]
Tissue strip (Biowire)	hiPSC-CM NHCF	1.1×10^5	Fibrin Matrigel	Angiotensin II Losartan	200 nM 10–50 μM	Relaxin Saracatinib	0.1–0.5 μg/mL 1–10 μM	• Contraction force and kinetics • Beat rate • Ca^{2+} transients • Cell viability	[55]
Tissue strip	hiPSC-CM	1×10^6	Fibrin Matrigel	Aspirin Atenolol Captopril Citalopram Clonidine Dobutamine Doxorubicin Enalaprilat Epinephrine Flecainide Forskolin Glibenclamide Itraconazole Ivabradine	0.01–1 mM 0.1–10 μM 1–100 μM 1–100 μM 0.01–1 μM 0.1–10 μM 0.1–10 μM 1–100 μM 0.01–1 μM 0.1–10 μM 0.1–10 μM 0.1–10 μM 0.1–10 μM 0.1–10 μM	Levosimendan Milrinone Omecamtiv Paracetamol Phentolamine Pimobendan Pravastatin Sildenafil Sorafenib Sunitinib Terbutaline Tolbutamide Verapamil Zimelidine	0.01–1 μM 1–100 μM 0.01–1 μM 10–1000 μM 1–100 μM 1–100 μM 1–100 μM 0.3–30 μM 0.1–10 μM 0.1–10 μM 0.1–10 μM 1–100 μM 0.01–1 μM 1–100 μM	• Contraction amplitude and kinetics	[51]
Tissue ring	hiPSC-CM	2×10^6	pcECM Chitosan	ATX-II Carbamylcholine Carbenoxolone Dofetilide E-4031	30 nM 1 μM 50 μM 25 nM 0.1–1 μM	Isoproterenol Lidocaine Ouabain Quinidine	1 μM 100 μM 1 mM 0.1–30 μM	• Ca^{2+} transients • Action potential amplitude and kinetics • Contraction force and kinetics	[60]
Atrial and ventricular tissue ring	hESC-CM	2×10^6	Collagen	Carbamylcholine Flecainide Isoproterenol	2–10 μM 10 μM 10 μM	Lidocaine Nifedipine Vernakalant	100 μM 0.1 μM 30 μM	• Action potential duration • Beat rate • Contraction force	[61]

Chamber	hiPSC-CM	3×10^6	PCL/gelatin nanofibers	Isoproterenol	0.1 nM–0.1 mM			• Pressure-volume loops • Beat rate	[62]
Chamber (hvCOC)	hESC-CM NHDF	1×10^7	Collagen I Matrigel	Digoxin Disopyramide Flecainide	0.1 μM 1 μM 0.01–10 μM	Isoproterenol Nifedipine Verapamil	0.01–10 μM 1 μM 0.01–1 μM	• Pressure-volume loops • Action potential amplitude and kinetics	[63]
Chamber (hvCOC)	hESC-CM NHDF	1×10^7	Collagen I Matrigel	Isoproterenol Levosimendan	0.1–10 μM 0.001–1 μM	Milrinone	0.01–1 μM	• Pressure-volume loops	[64•]
Tissue strip (hvCTS)	hESC-CM NHDF	1×10^6	Collagen I Matrigel	Amitriptyline Aspirin Bepridil Caffeine Digoxin Disopyramide Dobutamine Dopamine Flecainide Glibenclamide Isoproterenol Levosimendan Lidocaine	10–100 μM 0.03–30 μM 30–300 μM 0.1–100 μM 0.1–30 μM 0.1–100 μM 0.03–100 μM 1–100 μM 0.1–100 μM 0.1–30 μM 0.001–3 μM 0.1–30 μM 0.03–1 mM	Lisinopril Mibefradil Milrinone Nifedipine Norepinephrine Pravastatin Procainamide Quinidine Ramipril Tocainide Tolbutamide Verapamil	0.1–30 μM 0.1–10 μM 0.03–100 μM 0.03–10 μM 1–10 μM 0.03–30 μM 0.1–100 μM 3–100 μM 0.1–30 μM 0.1–100 μM 0.1–3 μM 0.03–3 μM	• Contraction force	

hADSC human adipose-derived stem cells (Lonza), *HCAEC* human coronary artery endothelial cells (Cell Applications), *hCF* human cardiac fibroblasts (PromoCell), *hCMEC* human cardiac microvascular endothelial cells (PromoCell), *hESC-CMS* human embryonic stem cell derived mesenchymal stem cell, *hiPSC-CF* hiPSC-derived cardiac fibroblasts (Axiogenesis), *hMSC* human mesenchymal stem cells (Lonza), *HMVEC* human cardiac microvascular endothelial cells (Lonza), *HS27a* human bone marrow stromal cells (ATCC), *HUVEC* human umbilical vein endothelial cells (Lonza), *hvCOC* human ventricular cardiac organoid chamber, *hvCTS* human ventricular cardiac tissue strip, *NHCF* normal human ventricular cardiac fibroblasts (Lonza), *NHDF* normal human dermal fibroblasts (Lonza), *pcECM* porcine cardiac ECM, PCL polycaprolactone

2.3.1 Spheroids

At the smallest end of the scale are cardiac spheroids, also often referred to as cardiac organoids. Cardiac spheroids are small hPSC-CM aggregates that are formed by hanging-drop [26] or self-assembly on low-attachment substrates [27]. These platforms are generally scaffold-free, which allows for a dense network of cell-cell connections and removes any concern of drug absorption by scaffolding hydrogels or silicone support structures often used for larger platforms [28]. Spheroid systems often include non-myocyte cell types such as endothelial, fibroblast, and mesenchymal cells, which has repeatedly been shown to enhance spheroid function [29–31]. Perhaps most attractively, the small scale of cardiac spheroids requires significantly lower resources in terms of cell number and culture space and are most easily amenable to automated generation and high-throughput analysis.

Cardiac spheroids have been used extensively to develop drug testing platforms. In an earlier study, it was shown that cardiac spheroids generated from hiPSC-CMs were similarly able to model doxorubicin-mediated cardiotoxicity as compared to spheroids made from primary human cardiomyocytes [32]. Demonstrating their high-throughput capabilities, a study used cardiac spheroids to screen a panel of 29 compounds approved by regulatory agencies with or without known structural cardiotoxicity [33•]. It was demonstrated that this platform was able to detect changes in cellular viability, endoplasmic reticulum integrity, and mitochondrial membrane potential. Beyond structural effects, cardiac spheroids have been used to stratify pro-arrhythmic toxicity of hERG channel blockers and environmental toxins [34].

Using cardiac spheroids, it is also possible to model disease states. To model cardiac fibrosis, spheroids generated from hESC-CMs and hESC-derived mesenchymal stem cells were treated with transforming growth factor beta (TGF-β) [31]. It was shown that TGF-β triggered fibrotic features in the cardiac spheroids and that this response was worsened with the administration of known cardiotoxins. In a separate study, cardiac spheroids were used to model

myocardial infarction by culturing in hypoxic conditions and treating with noradrenaline [35]. It was shown that hypoxic conditions worsened doxorubicin-mediated cardiotoxicity, while an antifibrotic compound could reduce ischemic spheroid stiffness and asynchronicity.

While the use of cardiac spheroids for drug screening is advantageous given their relative accessibility and high-throughput nature, these culture systems do not promote uniaxially-aligned contractile machinery and functional outputs are often limited to cell viability with some insight into contractility and arrhythmogenicity by measurement of spheroid deflection. However, it is possible for spheroids to serve as building blocks for higher order tissues, as was demonstrated with bioprinting of spheroids into larger cardiac rings [36]. Ultimately, higher-throughput spheroid systems may be best suited for earlier stages of drug compound testing.

2.3.2 Microtissues

To increase functional readout capacity while retaining the high-throughput benefits of spheroid culture systems, many have developed what we here call microtissues, where a similarly small number of cells, sometimes in a hydrogel scaffold, are self-assembled onto manufactured posts, such that they form geometries similar to the cardiac strips and rings presented in the following sections [37–41]. It was demonstrated that microtissues outperform age-matched two-dimensional hiPSC-CMs in terms of predictive accuracy in drug response [38]. Building on the high-throughput advantages of spheroid culture systems, these microtissue platforms provide uniaxial mechanical cues, generating improved cellular alignment and facilitate more rigorous measurement of contractile function by tracking the deflection of cantilever posts.

Possibly the most useful application of microtissues or other smaller cardiac platforms is as an intermediate screen between high-throughput two-dimensional *in vitro* experiments and animal studies. This paradigm was demonstrated in a study screening for pro-proliferative compounds using 96-well microtissues, where an initial pool of approximately 5,000 compounds were screened in two-dimensional hiPSC-CMs for their ability to induce cellular proliferation [42].

Of this initial pool, 105 compounds were identified and screened further for pro-proliferative effects using microtissues, which also allowed for the elimination of compounds causing negative functional effects. A smaller pool of the leading compounds were then further evaluated in microtissues that were further matured with fatty acid supplementation [40,42]. This study uniquely demonstrates a pathway by which to pursue drug development with varying hierarchies of *in vitro* hPSC-CM models.

2.3.3 Sheets

Cardiac sheets consist of one or multiple layers of hPSC-CMs and are particularly useful for detecting arrhythmogenicity. Using fluorescent voltage or calcium-sensitive dyes or genetically encoded sensors, it is possible to model arrhythmic risk of drug compounds by visualizing conduction speeds and re-entry waves as was done in two-dimensional cell sheets [43]. This platform has the additional benefit of microgrooves providing anisotropic cell patterning that more closely represents native myocardium. Other groups have developed methods of coating hPSC-CMs and other cell types with ECM and seeding them into cell sheets that are multiple layers thick [44,45]. Using motion tracking, it was possible to measure the effects of several drug compounds on magnitude of contraction, contraction kinetics and abnormal beat intervals [44]. However, shortcomings of cardiac sheets include the difficulty in obtaining direct measurement of force output and the need for additional interventions to facilitate sheet patterning and cellular alignment.

2.3.4 Tissue strips

Cardiac strips are perhaps the most commonly thought of hEHT platform along with spheroids, and are made from hPSC-CMs embedded in a hydrogel that is cast into a mold where it solidifies and subsequently compacts and begins beating spontaneously [46]. Cardiac strips are cast uniaxially between two elastomeric posts [47] or wires (Biowire) [48,49]. This platform

enables higher-throughput measurement of contractile forces via tracking the deflection of elastomeric supports. As such, these models are particularly suited to drug screening, where easily-measured force production and kinetics can provide insights into the inotropic and arrhythmogenic effects of test compounds.

To date, cardiac strips have been used to test a wide panel of compounds with and without known cardiac effects. A panel of eleven compounds was tested on cardiac strips, demonstrating that these tissues were able to faithfully reproduce positive and negative inotropic effects when compared to human atrial trabeculae, but the relative immaturity of the hiPSC-CMs was evident due to limited observed beta-adrenergic effects [50]. The benefits of three-dimensional culture were further demonstrated in another study where an impressive panel of 28 drugs was tested on cardiac strips as well as 2D hiPSC-CM monolayers, where it was demonstrated that the tissues yielded more accurate drug responses in terms of contractility and calcium transient response (85% accuracy for hiPSC-CM monolayers vs. 93% accuracy for tissue strips) [51]. Additionally, both of these studies demonstrate the potential for increased throughput with tissue strip platforms despite their larger size, as not only were multiple drugs tested, but at multiple doses, enabling the derivation of EC_{50} values.

Chronic electrical stimulation of cardiac strips has been demonstrated to improve tissue maturity and promote positive force-frequency relationships, thus improving the accuracy of drug responses and the ability to model positive inotropy [52]. Similar stimulation protocols have been used on the Biowire II platform, which was used to derive EC_{50} values and demonstrate canonical responses for several drug compounds [49]. This platform and others have been further developed to model specific atrial and ventricular responses to drugs in chamber-specific tissues [53,54] and to explore anti-fibrotic drugs in angiotensin II-mediated non-genetic cardiomyopathy [55]. Despite their increased size and required resources as compared to spheroids or microtissues, strip hEHTs have been used to generate impressive datasets demonstrating

relevant responses to many compounds at various doses in a single study. Paired with efforts to improve hEHT maturity, efforts to increase analysis throughput through optical [56,57] or magnetic detection of post movement [58], will only further increase the utility of cardiac strip platforms.

2.3.5 Tissue rings

Cardiac rings are similar to cardiac strips save for their shape, where cardiac rings are cast in circular molds before being transferred to isometric or elastomeric supports [59]. Given their larger surface area, cardiac rings are particularly suited to modeling voltage propagation as an indicator of arrhythmogenicity. Using genetically-encoded voltage and calcium sensors, tissue rings have been shown to properly model drug-induced changes in contraction rate and conduction properties [60]. Additionally, by using patient-derived hiPSCs, authors were able to reproduce long QT syndrome and demonstrate drug-induced reentrant arrhythmias. This platform was further developed to model chamber-specific responses to a panel of drugs by using atrial or ventricular hiPSC-CMs [61]. While tissue ring platforms are useful for modeling drug-induced changes in conduction properties and arrhythmogenicity, it would appear that they may be less popular than other platforms of similar size. This may be due to the requirement for more individual tissue handling, as measurement of contractile forces often requires the use of a force transducer, which hampers throughput.

2.3.6 Chambers

At the opposite end of the spectrum from cardiac spheroids are cardiac chambers, which resemble a miniaturized ventricle [62,63]. The geometry of this platform most closely resembles a native ventricle, and engineered cardiac chambers are the only platform capable of generating pressure, enabling measurement of clinically relevant outputs including ejection fraction, cardiac output, and pressure-volume loops. Cardiac chambers have been shown to surpass lower-order 2D and 3D hPSC-CM culture systems in transcriptional maturity [63]. Given their advanced

maturation and attainable performance metrics, chamber constructs are an appealing platform for drug screening and characterization.

One such platform (human ventricle-like cardiac organoid chamber, hvCOC) is generated by casting hESC-CMs in a hydrogel around a balloon catheter, which is removed after tissue compaction [63]. This initial study demonstrated altered pressure-volume loops and electrophysiological performance after treatment with six compounds. In a follow up study, hvCOCs and human ventricular-like cardiac tissue strips (hvCTS) were treated with a panel of 25 cardioactive compounds, where it was demonstrated that hvCOCs displayed enhanced positive inotropy as compared to hvCTSs [64•]. A similar platform has been developed using pull-spun nanofibers that recapitulates the concentric, anisotropic orientation of native myocardium [62]. While it was possible to measure pressure-volume loops, this model failed to replicate a positive inotropic response with isoproterenol treatment, indicating relative immaturity.

Compared to other cardiac tissue platforms, cardiac chambers are limited in terms of the increased resources and technical expertise required, ultimately resulting in a lower-throughput platform. However, with the addition of additional maturation techniques such as electrical stimulation and anisotropic cell sheet patterning [65], such models could effectively serve as *in vitro* replacements for Langendorff whole-heart preparations.

2.4 Challenges remaining

Despite wide-spread excitement surrounding engineered cardiac platforms for drug development and several commercialization efforts underway, several hurdles remain. Compared to adult myocardium, or even neonatal myocardium, engineered cardiac constructs present a very immature phenotype, potentially limiting their physiological relevance. In early stages after differentiation with no intervention, hPSC-CMs display only fetal transcriptomes [66], ion channel expression [67], metabolic function [68], and contractility [69]. While three-dimensional culture has been shown to promote advanced hPSC-CM maturation [21–25], it is evidently insufficient to

routinely produce a robust cardiac phenotype that includes positive force-frequency responses and positive inotropic responses, thus potentially limiting their use as drug screening platforms. Several methods shown to advance hPSC-CM maturity in two-dimensional culture could potentially have the same effect in tissues, including fatty acid [70] or thyroid hormone supplementation [71], or microRNA treatment [72,73]. Advanced engineering approaches have been employed to further increase the maturity achieved in cardiac tissues, including electrical stimulation [52], increasing afterload [74], and the addition of preload or passive stretch [75,76], which, if successful, will greatly improve the predictive capacity of these engineered models.

A significant difficulty that has become apparent when working with engineered tissues is controlling variability and demonstrating reproducibility. This variability arises, in part, from hPSC-CM batch-to-batch variability and the different protocols used by different institutions for hPSC-CM differentiation and tissue generation, both of which are inherently human processes where results may vary simply by the hands performing the experiment. To remove human sources of variability, many are turning toward automation of tissue generation and analysis, which will also increase platform throughput [37,57,77]. Additional variation arises from the different genetic backgrounds of the various hPSC lines used. Highlighting this challenge, a study compared the performance of ten different hPSC lines in cardiac tissue strips [78]. It was found that spontaneous and electrically paced tissue contractile performance and kinetics varied widely between the different lines, emphasizing the need for isogenic controls in disease modeling and advocating for the use of multiple hPSC lines during platform validation. Interestingly, it was found that despite the variability in baseline performance, the different hPSC lines behaved more consistently with regard to drug response, although with varying EC_{50} values [78]. To address this concern, it is likely that robust cardiac tissue platforms will continue to rely on multiple biological replicates and turn toward automation and the use of multiple genetic backgrounds.

Conversely, this variability can be seen as a facet of hPSC and tissue engineering that

has not yet been fully taken advantage of. There are numerous studies describing the development of hPSC lines harboring cardiomyopathy-associated mutations that could be further used to screen disease-specific drug candidates in engineered cardiac constructs [79]. Additionally, such engineered tissue models can be used to examine biological sex-related differences in cardiac biology and disease, as these differences are known, but often overlooked in *in vitro* disease modeling and preclinical screening [80]. By including multiple cell lines from different genetic backgrounds and with different disease-causing genetic variants, we can begin to approximate not only personalized and patient-specific medicine, but also population-wide responses to different pharmacological agents in the dish.

A significant limitation to translatability is that most platforms lack the biological complexity needed to fully reproduce native myocardium, necessitating the continued reliance on animal models for preclinical testing. At their simplest, cardiac constructs contain only hPSC-CMs, while others have included additional cell types including fibroblasts, endothelial cells, and mesenchymal cells, which have been shown to improve tissue quality and maturity. A biological element often missing from engineered cardiac constructs is vasculature, a key component needed to accurately model drug delivery. Strategies to vascularize constructs consist of co-culturing with endothelial cells and addition of angiogenic factors, three-dimensional bioprinting, or microfluidic systems [81,82]. The development of *in vitro* models that better recapitulate the complexity of drug delivery and toxicity will also require the inclusion of additional organ systems involved in drug metabolism and clearance, e.g. hepatic and renal systems. To achieve this, several groups are developing complex, modular organ-on-a-chip systems [83,84]. If successful, such vascularized multi-organ systems would be the pinnacle of *in vitro* drug testing platforms.

Lastly, it is worth noting that the vast majority of studies described in this review evaluated only compounds with known effects in human patients. As such, further studies are needed to demonstrate the true predictive capabilities of engineered cardiac tissues for clinical trial success.

However, some pioneering studies have used engineered constructs to explore novel antifibrotic agents [55], perform screening experiments to identify pro-proliferative compounds for heart regeneration [42], evaluate a novel myotrope [85], and even to evaluate the effect of COVID-19 treatments on cardiac function [86]. Thus, it is evident that the stage is now set to explore the potential effects of novel therapeutics in engineered cardiac platforms.

2.5 Conclusion

In order to increase the efficiency with which new drugs are discovered and brought to clinical trials, it is necessary to improve the human *in vitro* models used, to increase their biological relevance and enable the field to move away from a reliance on animal models as the gold standard. To address concerns of cardiac toxicity, great efforts have been put toward the development of engineered cardiac tissues from hPSC-CMs. These platforms range in shape and scale from cardiac spheroids and microtissues, to sheets, strips, and rings, to chambers emulating an entire ventricle, all of which present their own advantages and limitations. This review has highlighted recent advances made in the development of cardiac tissue engineering for drug screening platforms. While lacking functional maturity and structural complexity in some regards, these constructs hold merit as drug screening platforms with powerful predictive capabilities that, as they stand, can provide value to early stages of the drug screening pipeline. With continued advancements in tissue maturity, automation, and throughput, it is our prediction that cardiac tissue engineering will continue to gain favor in the pharmaceutical industry.

2.6 References

1. Wouters OJ, McKee M, Luyten J. Estimated research and development investment needed to bring a new medicine to market, 2009-2018. J Am Med Assoc. 2020:323(9):844–53. Doi: 10.1001/jama.2020.1166.

2. Wong CH, Siah KW, Lo AW. Estimation of clinical trial success rates and related parameters. Biostatistics. 2019:20(2):273–86. Doi: 10.1093/biostatistics/kxx069.

3. Packer M. Unbelievable folly of clinical trials in heart failure. Circ Hear Fail. 2016:9(4). Doi: 10.1161/CIRCHEARTFAILURE.116.002837.

4. Hartung T. Food for thought; look back in anger - what clinical studies tell us about preclinical work. ALTEX. 2013:30(3):275–91. Doi: 10.14573/altex.2013.3.275.

5. Olson H, Betton G, Robinson D, Thomas K, Monro A, Kolaja G, et al. Concordance of the toxicity of pharmaceuticals in humans and in animals. Regul Toxicol Pharmacol. 2000:32(1):56–67. Doi: 10.1006/rtph.2000.1399.

6. Paul SM, Mytelka DS, Dunwiddie CT, Persinger CC, Munos BH, Lindborg SR, et al. How to improve r&d productivity: the pharmaceutical industry's grand challenge. Nat Rev Drug Discov. 2010:9(3):203–14. Doi: 10.1038/nrd3078.

7. Onakpoya IJ, Heneghan CJ, Aronson JK. Post-marketing withdrawal of 462 medicinal products because of adverse drug reactions: a systematic review of the world literature. BMC Med. 2016:14(1):1–11. Doi: 10.1186/s12916-016-0553-2.

8. Laverty H, Benson C, Cartwright E, Cross M, Garland C, Hammond T, et al. How can we improve our understanding of cardiovascular safety liabilities to develop safer medicines? Br J Pharmacol. 2011:163(4):675–93. Doi: 10.1111/J.1476-5381.2011.01255.X.

9. Fernandez D, Ghanta A, Kauffman GW, Sanguinetti MC. Physicochemical features of the herg channel drug binding site. J Biol Chem. 2004:279(11):10120–7. Doi: 10.1074/jbc.M310683200.

10. Gintant G, Sager PT, Stockbridge N. Evolution of strategies to improve preclinical cardiac safety testing. Nat Rev Drug Discov 2016 157. 2016:15(7):457–71. Doi: 10.1038/nrd.2015.34.

11. Milani-Nejad N, Janssen PML. Small and large animal models in cardiac contraction research: advantages and disadvantages. Pharmacol Ther. 2014:141(3):235–49. Doi: 10.1016/J.PHARMTHERA.2013.10.007.

12. Silva KAS, Emter CA. Large animal models of heart failure: a translational bridge to clinical success. JACC Basic to Transl Sci. 2020:5(8):840–56. Doi: 10.1016/j.jacbts.2020.04.011.

13. Thomson JA. Embryonic stem cell lines derived from human blastocysts. Science (80-). 1998:282(5391):1145–7. Doi: 10.1126/science.282.5391.1145.

14. Takahashi K, Yamanaka S. Induction of pluripotent stem cells from mouse embryonic and adult fibroblast cultures by defined factors. Cell. 2006:126(4):663–76. Doi: 10.1016/j.cell.2006.07.024.

15. Mummery CL, Zhang J, Ng ES, Elliott DA, Elefanty AG, Kamp TJ. Differentiation of human embryonic stem cells and induced pluripotent stem cells to cardiomyocytes: a methods overview. Circ Res. 2012:111(3):344–58. Doi: 10.1161/CIRCRESAHA.110.227512.

16. Lian X, Hsiao C, Wilson G, Zhu K, Hazeltine LB, Azarin SM, et al. Robust cardiomyocyte differentiation from human pluripotent stem cells via temporal modulation of canonical wnt signaling. Proc Natl Acad Sci U S A. 2012:109(27). Doi: 10.1073/pnas.1200250109.

17. Snir M, Kehat I, Gepstein A, Coleman R, Itskovitz-Eldor J, Livne E, et al. Assessment of the ultrastructural and proliferative properties of human embryonic stem cell-derived cardiomyocytes. Am J Physiol - Hear Circ Physiol. 2003:285(6 54-6). Doi: 10.1152/ajpheart.00020.2003.

18. Synnergren J, Améen C, Jansson A, Sartipy P. Global transcriptional profiling reveals similarities and differences between human stem cell-derived cardiomyocyte clusters and heart tissue. Physiol Genomics. 2012:44(4):245–58. Doi: 10.1152/physiolgenomics.00118.2011.

19. Tan SH, Ye L. Maturation of pluripotent stemcell-derived cardiomyocytes: a critical step for drug development and cell therapy. J Cardiovasc Transl Res. 2018:11(5):375–92. Doi: 10.1007/s12265-018-9801-5.

20. Marchianò S, Bertero A, Murry CE. Learn from your elders: developmental biology lessons to guide maturation of stem cell-derived cardiomyocytes. Pediatr Cardiol. 2019:40(7):1367–87. Doi: 10.1007/s00246-019-02165-5.

21. Mihic A, Li J, Miyagi Y, Gagliardi M, Li SH, Zu J, et al. The effect of cyclic stretch on maturation and 3d tissue formation of human embryonic stem cell-derived cardiomyocytes. Biomaterials. 2014:35(9):2798–808. Doi: 10.1016/j.biomaterials.2013.12.052.

22. Ruan J-LL, Tulloch NL, Razumova M V., Saiget M, Muskheli V, Pabon L, et al. Mechanical stress conditioning and electrical stimulation promote contractility and force maturation of induced pluripotent stem cell-derived human cardiac tissue. Circulation. 2016:134(20):1557–67. Doi: 10.1161/CIRCULATIONAHA.114.014998.

23. Ruan JL, Tulloch NL, Saiget M, Paige SL, Razumova M V., Regnier M, et al. Mechanical stress promotes maturation of human myocardium from pluripotent stem cell-derived progenitors. Stem Cells. 2015:33(7):2148–57. Doi: 10.1002/stem.2036.

24. Abilez OJ, Tzatzalos E, Yang H, Zhao MT, Jung G, Zöllner AM, et al. Passive stretch induces structural and functional maturation of engineered heart muscle as predicted by computational modeling. Stem Cells. 2018:36(2):265–77. Doi: 10.1002/stem.2732.

25. Shimko VF, Claycomb WC. Effect of mechanical loading on three-dimensional cultures of embryonic stem cell-derived cardiomyocytes. Tissue Eng - Part A. 2008:14(1):49–58. Doi: 10.1089/ten.a.2007.0092.

26. Beauchamp P, Moritz W, Kelm JM, Ullrich ND, Agarkova I, Anson BD, et al. Development and characterization of a scaffold-free 3d spheroid model of induced pluripotent stem cell-

derived human cardiomyocytes. Tissue Eng - Part C Methods. 2015:21(8):852–61. Doi: 10.1089/ten.tec.2014.0376.

27. Richards DJ, Coyle RC, Tan Y, Jia J, Wong K, Toomer K, et al. Inspiration from heart development: biomimetic development of functional human cardiac organoids. Biomaterials. 2017:142:112–23. Doi: 10.1016/j.biomaterials.2017.07.021.

28. Nugraha B, Hong X, Mo X, Tan L, Zhang W, Chan PM, et al. Galactosylated cellulosic sponge for multi-well drug safety testing. Biomaterials. 2011:32(29):6982–94. Doi: 10.1016/J.BIOMATERIALS.2011.05.087.

29. Giacomelli E, Meraviglia V, Campostrini G, Cochrane A, Cao X, van Helden RWJ, et al. Human-ipsc-derived cardiac stromal cells enhance maturation in 3d cardiac microtissues and reveal non-cardiomyocyte contributions to heart disease. Cell Stem Cell. 2020:26(6):862-879.e11. Doi: 10.1016/j.stem.2020.05.004.

30. Beauchamp P, Jackson CB, Ozhathil LC, Agarkova I, Galindo CL, Sawyer DB, et al. 3D co-culture of hipsc-derived cardiomyocytes with cardiac fibroblasts improves tissue-like features of cardiac spheroids. Front Mol Biosci. 2020:7:14. Doi: 10.3389/fmolb.2020.00014.

31. Lee MO, Jung KB, Jo SJ, Hyun SA, Moon KS, Seo JW, et al. Modelling cardiac fibrosis using three-dimensional cardiac microtissues derived from human embryonic stem cells. J Biol Eng. 2019:13(1):1–17. Doi: 10.1186/s13036-019-0139-6.

32. Polonchuk L, Chabria M, Badi L, Hoflack JC, Figtree G, Davies MJ, et al. Cardiac spheroids as promising in vitro models to study the human heart microenvironment. Sci Rep. 2017:7(1):1–12. Doi: 10.1038/s41598-017-06385-8.

33. Archer CR, Sargeant R, Basak J, Pilling J, Barnes JR, Pointon A. Characterization and validation of a human 3d cardiac microtissue for the assessment of changes in cardiac

pathology. Sci Rep. 2018:8(1):1–15. Doi: 10.1038/s41598-018-28393-y.

34. Kofron CM, Kim TY, Munarin F, Soepriatna AH, Kant RJ, Mende U, et al. A predictive in vitro risk assessment platform for pro-arrhythmic toxicity using human 3d cardiac microtissues. Sci Rep. 2021:11(1):1–16. Doi: 10.1038/s41598-021-89478-9.

35. Richards DJ, Li Y, Kerr CM, Yao J, Beeson GC, Coyle RC, et al. Human cardiac organoids for the modelling of myocardial infarction and drug cardiotoxicity. Nat Biomed Eng. 2020:4(4):446–62. Doi: 10.1038/s41551-020-0539-4.

36. Arai K, Murata D, Takao S, Nakamura A, Itoh M, Kitsuka T, et al. Drug response analysis for scaffold-free cardiac constructs fabricated using bio-3d printer. Sci Rep. 2020:10(1):1–11. Doi: 10.1038/s41598-020-65681-y.

37. Thavandiran N, Hale C, Blit P, Sandberg ML, McElvain ME, Gagliardi M, et al. Functional arrays of human pluripotent stem cell-derived cardiac microtissues. Sci Rep. 2020:10(1):1–13. Doi: 10.1038/s41598-020-62955-3.

38. Lu HF, Leong MF, Lim TC, Chua YP, Lim JK, Du C, et al. Engineering a functional three-dimensional human cardiac tissue model for drug toxicity screening. Biofabrication. 2017:9(2). Doi: 10.1088/1758-5090/aa6c3a.

39. Boudou T, Legant WR, Mu A, Borochin MA, Thavandiran N, Radisic M, et al. A microfabricated platform to measure and manipulate the mechanics of engineered cardiac microtissues. Tissue Eng - Part A. 2012:18(9–10):910–9. Doi: 10.1089/ten.tea.2011.0341.

40. Mills RJ, Titmarsh DM, Koenig X, Parker BL, Ryall JG, Quaife-Ryan GA, et al. Functional screening in human cardiac organoids reveals a metabolic mechanism for cardiomyocyte cell cycle arrest. Proc Natl Acad Sci. 2017:114(40):E8372–81. Doi: 10.1073/PNAS.1707316114.

41. Truitt R, Mu A, Corbin EA, Vite A, Brandimarto J, Ky B, et al. Increased afterload augments

sunitinib-induced cardiotoxicity in an engineered cardiac microtissue model. JACC Basic to Transl Sci. 2018:3(2):265–76. Doi: 10.1016/j.jacbts.2017.12.007.

42. Mills RJ, Parker BL, Quaife-Ryan GA, Voges HK, Needham EJ, Bornot A, et al. Drug screening in human psc-cardiac organoids identifies pro-proliferative compounds acting via the mevalonate pathway. Cell Stem Cell. 2019:24(6):895-907.e6. Doi: 10.1016/j.stem.2019.03.009.

43. Shum AMY, Che H, Wong AOT, Zhang C, Wu H, Chan CWY, et al. A micropatterned human pluripotent stem cell-based ventricular cardiac anisotropic sheet for visualizing drug-induced arrhythmogenicity. Adv Mater. 2017:29(1):1602448. Doi: 10.1002/adma.201602448.

44. Tadano K, Miyagawa S, Takeda M, Tsukamoto Y, Kazusa K, Takamatsu K, et al. Cardiotoxicity assessment using three-dimensional vascularized cardiac tissue consisting of fibroblasts and human ipsc-derived cardiomyocytes. Mol Ther - Methods Clin Dev. 2021:22:338. Doi: 10.1016/j.omtm.2021.05.007.

45. Takeda M, Miyagawa S, Ito E, Harada A, Mochizuki-Oda N, Matsusaki M, et al. Development of a drug screening system using three-dimensional cardiac tissues containing multiple cell types. Sci Rep. 2021:11(1):1–12. Doi: 10.1038/s41598-021-85261-y.

46. Eschenhagen T, Fink C, Remmers U, Scholz H, Wattchow J, Weil J, et al. Three-dimensional reconstitution of embryonic cardiomyocytes in a collagen matrix: a new heart muscle model system. FASEB J. 1997:11(8):683–94. Doi: 10.1096/fasebj.11.8.9240969.

47. Hansen A, Eder A, Bönstrup M, Flato M, Mewe M, Schaaf S, et al. Development of a drug screening platform based on engineered heart tissue. Circ Res. 2010:107(1):35–44. Doi: 10.1161/CIRCRESAHA.109.211458.

48. Nunes SS, Miklas JW, Liu J, Aschar-Sobbi R, Xiao Y, Zhang B, et al. Biowire: a platform for maturation of human pluripotent stem cell-derived cardiomyocytes. Nat Methods. 2013:10(8):781–7. Doi: 10.1038/nmeth.2524.

49. Feric NT, Pallotta I, Singh R, Bogdanowicz DR, Gustilo MM, Chaudhary KW, et al. Engineered cardiac tissues generated in the biowire ii: a platform for human-based drug discovery. Toxicol Sci. 2019:172(1):89–97. Doi: 10.1093/toxsci/kfz168.

50. Mannhardt I, Eder A, Dumotier B, Prondzynski M, Kr-amer E, Traebert M, et al. Blinded contractility analysis in hipsc-cardiomyocytes in engineered heart tissue format: comparison with human atrial trabeculae. Toxicol Sci. 2017:158(1):164–75. Doi: 10.1093/toxsci/kfx081.

51. Saleem U, Meer BJV, Katili PA, Yusof NANM, Mannhardt I, Garcia AK, et al. Blinded, multicenter evaluation of drug-induced changes in contractility using human-induced pluripotent stem cell-derived cardiomyocytes. Toxicol Sci. 2020:176(1):103–23. Doi: 10.1093/toxsci/kfaa058.

52. Ronaldson-Bouchard K, Ma SP, Yeager K, Chen T, Song LJ, Sirabella D, et al. Advanced maturation of human cardiac tissue grown from pluripotent stem cells. Nature. 2018:556(7700):239–43. Doi: 10.1038/s41586-018-0016-3.

53. Zhao Y, Rafatian N, Feric NT, Cox BJ, Aschar-Sobbi R, Wang EY, et al. A platform for generation of chamber-specific cardiac tissues and disease modeling. Cell. 2019:176(4):913-927.e18. Doi: 10.1016/j.cell.2018.11.042.

54. Lemme M, Ulmer BM, Lemoine MD, Zech ATL, Flenner F, Ravens U, et al. Atrial-like engineered heart tissue: an in vitro model of the human rtrium. Stem Cell Reports. 2018:11(6):1378–90. Doi: 10.1016/j.stemcr.2018.10.008.

55. Wang EY, Kuzmanov U, Smith JB, Dou W, Rafatian N, Lai BFL, et al. An organ-on-a-chip

model for pre-clinical drug evaluation in progressive non-genetic cardiomyopathy. J Mol Cell Cardiol. 2021:160:97–110. Doi: 10.1016/j.yjmcc.2021.06.012.

56. Stoehr A, Neuber C, Baldauf C, Vollert I, Friedrich FW, Flenner F, et al. Automated analysis of contractile force and ca2+ transients in engineered heart tissue. AJP Hear Circ Physiol. 2014:306(9):H1353–63. Doi: 10.1152/ajpheart.00705.2013.

57. Mannhardt I, Saleem U, Benzin A, Schulze T, Klampe B, Eschenhagen T, et al. Automated contraction analysis of human engineered heart tissue for cardiac drug safety screening. J Vis Exp. 2017:2017(122):55461. Doi: 10.3791/55461.

58. Bielawski KS, Leonard A, Bhandari S, Murry CE, Sniadecki NJ. Real-rime force and frequency analysis of engineered human heart tissue derived from induced pluripotent stem cells using magnetic sensing. Tissue Eng Part C. 2016:22(10):932–40. Doi: 10.1089/ten.tec.2016.0257.

59. Tiburcy M, Meyer T, Soong PL, Zimmermann WH. Collagen-based engineered heart muscle. Methods Mol Biol. 2014:1181:167–76. Doi: 10.1007/978-1-4939-1047-2_15.

60. Goldfracht I, Efraim Y, Shinnawi R, Kovalev E, Huber I, Gepstein A, et al. Engineered heart tissue models from hipsc-derived cardiomyocytes and cardiac ecm for disease modeling and drug testing applications. Acta Biomater. 2019:92:145–59.

61. Goldfracht I, Protze S, Shiti A, Setter N, Gruber A, Shaheen N, et al. Generating ring-shaped engineered heart tissues from ventricular and atrial human pluripotent stem cell-derived cardiomyocytes. Nat Commun. 2020:11(1):1–15. Doi: 10.1038/s41467-019-13868-x.

62. MacQueen LA, Sheehy SP, Chantre CO, Zimmerman JF, Pasqualini FS, Liu X, et al. A tissue-engineered scale model of the heart ventricle. Nat Biomed Eng. 2018:2(December):930–41. Doi: 10.1038/s41551-018-0271-5.

63. Li RA, Keung W, Cashman TJ, Backeris PC, Johnson B V., Bardot ES, et al. Bioengineering an electro-mechanically functional miniature ventricular heart chamber from human pluripotent stem cells. Biomaterials. 2018:163:116–27. Doi: 10.1016/j.biomaterials.2018.02.024.

64. Keung W, Chan PKW, Backeris PC, Lee EK, Wong N, Wong AOT, et al. Human cardiac ventricular-like organoid chambers and tissue strips from pluripotent stem cells as a two-tiered assay for inotropic responses. Clin Pharmacol Ther. 2019:106(2):402–14. Doi: 10.1002/cpt.1385.

65. Williams NP, Rhodehamel M, Yan C, Smith AST, Jiao A, Murry CE, et al. Engineering anisotropic 3d tubular tissues with flexible thermoresponsive nanofabricated substrates. Biomaterials. 2020:240:119856. Doi: 10.1016/J.BIOMATERIALS.2020.119856.

66. Van Den Berg CW, Okawa S, Chuva De Sousa Lopes SM, Van Iperen L, Passier R, Braam SR, et al. Transcriptome of human foetal heart compared with cardiomyocytes from pluripotent stem cells. Dev. 2015:142(18):3231–8. Doi: 10.1242/dev.123810.

67. Davis RP, van den Berg CW, Casini S, Braam SR, Mummery CL. Pluripotent stem cell models of cardiac disease and their implication for drug discovery and development. Vol. 17, Trends in Molecular Medicine. Elsevier Current Trends; 2011. p. 475–84. Doi: 10.1016/j.molmed.2011.05.001.

68. Ulmer BM, Eschenhagen T. Human pluripotent stem cell-derived cardiomyocytes for studying energy metabolism. Vol. 1867, Biochimica et Biophysica Acta - Molecular Cell Research. Elsevier B.V.; 2020. p. 118471. Doi: 10.1016/j.bbamcr.2019.04.001.

69. Pioner JM, Racca AW, Klaiman JM, Yang K-C, Guan X, Pabon L, et al. Isolation and mechanical measurements of myofibrils from human induced pluripotent stem cell-derived cardiomyocytes. Stem Cell Reports. 2016:6(6):885–96. Doi:

10.1016/j.stemcr.2016.04.006.

70. Yang X, Rodriguez ML, Leonard A, Sun L, Fischer KA, Wang Y, et al. Fatty acids enhance the maturation of cardiomyocytes derived from human pluripotent stem cells. Stem Cell Reports. 2019:13(4):657–68. Doi: 10.1016/j.stemcr.2019.08.013.

71. Yang X, Rodriguez M, Pabon L, Fischer KA, Reinecke H, Regnier M, et al. Tri-iodo-l-thyronine promotes the maturation of human cardiomyocytes-derived from induced pluripotent stem cells. J Mol Cell Cardiol. 2014:72:296–304. Doi: 10.1016/j.yjmcc.2014.04.005.

72. Kuppusamy KT, Jones DC, Sperber H, Madan A, Fischer KA, Rodriguez ML, et al. Let-7 family of microrna is required for maturation and adult-like metabolism in stem cell-derived cardiomyocytes. Proc Natl Acad Sci. 2015:112(21):E2785–94. Doi: 10.1073/pnas.1424042112.

73. Miklas JW, Clark E, Levy S, Detraux D, Leonard A, Beussman K, et al. TFPa/hadha is required for fatty acid beta-oxidation and cardiolipin re-modeling in human cardiomyocytes. Nat Commun 2019 101. 2019:10(1):1–21. Doi: 10.1038/s41467-019-12482-1.

74. Leonard A, Bertero A, Powers JD, Beussman KM, Bhandari S, Regnier M, et al. Afterload promotes maturation of human induced pluripotent stem cell derived cardiomyocytes in engineered heart tissues. J Mol Cell Cardiol. 2018:118:147–58. Doi: 10.1016/j.yjmcc.2018.03.016.

75. Bliley JM, Vermeer MCSC, Duffy RM, Batalov I, Kramer D, Tashman JW, et al. Dynamic loading of human engineered heart tissue enhances contractile function and drives desmosome-linked disease phenotype. bioRxiv. 2020: Doi: 10.1101/2020.05.25.111690.

76. Lu K, Seidel T, Cao-Ehlker X, Dorn T, Nazeer Batcha AM, Schneider CM, et al. Progressive stretch enhances growth and maturation of 3d stem-cell-derived myocardium.

2021:11(13):13. Doi: 10.7150/thno.54999.

77. Stoehr A, Neuber C, Baldauf C, Vollert I, Friedrich FW, Flenner F, et al. Automated analysis of contractile force and ca2+ transients in engineered heart tissue. Am J Physiol Circ Physiol. 2014:306(9):H1353–63. Doi: 10.1152/ajpheart.00705.2013.

78. Mannhardt I, Saleem U, Mosqueira D, Loos MF, Ulmer BM, Lemoine MD, et al. Comparison of 10 control hpsc lines for drug screening in an engineered heart tissue format. Stem Cell Reports. 2020:15(4):983–98. Doi: 10.1016/j.stemcr.2020.09.002.

79. Hoes MF, Bomer N, van der Meer P. Concise review: the current state of human in vitro cardiac disease modeling: a focus on gene editing and tissue engineering. Stem Cells Transl Med. 2019:8(1):66–74. Doi: 10.1002/sctm.18-0052.

80. Lock R, Asafen H Al, Fleischer S, Tamargo M, Zhao Y, Radisic M, et al. A framework for developing sex-specific engineered heart models. Nat Rev Mater. 2021:1. Doi: 10.1038/S41578-021-00381-1.

81. Williams MAC, Mair DB, Lee W, Lee E, Kim D-H. Engineering three-dimensional vascularized cardiac tissues. Tissue Eng Part B Rev. 2021: Doi: 10.1089/ten.teb.2020.0343.

82. Osaki T, Sivathanu V, Kamm RD. Vascularized microfluidic organ-chips for drug screening, disease models and tissue engineering. Curr Opin Biotechnol. 2018:52:116–23. Doi: 10.1016/J.COPBIO.2018.03.011.

83. Lai BFL, Huyer LD, Lu RXZ, Drecun S, Radisic M, Zhang B. InVADE: integrated vasculature for assessing dynamic events. Adv Funct Mater. 2017:27(46):1703524. Doi: 10.1002/adfm.201703524.

84. Picollet-D'hahan N, Zuchowska A, Lemeunier I, Le Gac S. Multiorgan-on-a-chip: a systemic approach to model and decipher inter-organ communication. Vol. 39, Trends in

Biotechnology. Elsevier Current Trends; 2021. p. 788–810. Doi: 10.1016/j.tibtech.2020.11.014.

85. Shen S, Sewanan LR, Jacoby DL, Campbell SG. Danicamtiv enhances systolic function and frank-starling behavior at minimal diastolic cost in engineered human myocardium. J Am Heart Assoc. 2021:10(12):20860. Doi: 10.1161/JAHA.121.020860.

86. Wong AOT, Gurung B, Wong WS, Mak SY, Tse WW, Li CM, et al. Adverse effects of hydroxychloroquine and azithromycin on contractility and arrhythmogenicity revealed by human engineered cardiac tissues. J Mol Cell Cardiol. 2021:153:106–10. Doi: 10.1016/j.yjmcc.2020.12.014.

Chapter 3. Establishing a three-dimensional model of Duchenne muscular dystrophy with a robust, multifaceted disease phenotype

The findings in this chapter were published as the following first-author manuscript:

S.B. Bremner, C.J. Mandrycky, A. Leonard, R.M. Padgett, A.R. Levinson, E.S. Rehn, J.M. Pioner, N.J. Sniadecki, D.L. Mack. Full-length dystrophin deficiency leads to contractile and calcium transient defects in human engineered heart tissues. *Journal of Tissue Engineering.* 2022:13. DOI: 10.1177/20417314221119628.

3.1 Abstract

Cardiomyopathy is currently the leading cause of death for patients with Duchenne muscular dystrophy (DMD), a severe neuromuscular disorder affecting young boys. Animal models have provided insight into the mechanisms by which dystrophin protein deficiency causes cardiomyopathy, but there remains a need to develop human models of DMD to validate pathogenic mechanisms and identify therapeutic targets. Here, we have developed human engineered heart tissues (EHTs) from CRISPR-edited, human induced pluripotent stem cell-derived cardiomyocytes (hiPSC-CMs) expressing a truncated dystrophin protein lacking part of the actin-binding domain. The 3D EHT platform enables direct measurement of contractile force, simultaneous monitoring of Ca^{2+} transients, and assessment of myofibril structure. Dystrophin-mutant EHTs produced less contractile force as well as delayed kinetics of force generation and relaxation, as compared to isogenic controls. Contractile dysfunction was accompanied by reduced sarcomere length, increased resting cytosolic Ca^{2+} levels, delayed Ca^{2+} release and reuptake, and increased beat rate irregularity. Transcriptomic analysis revealed clear differences between dystrophin-deficient and control EHTs, including downregulation of genes related to Ca^{2+} homeostasis and extracellular matrix organization, and upregulation of genes related to regulation of membrane potential, cardiac muscle development, and heart contraction. These findings

indicate that the EHT platform provides the cues necessary to expose the clinically-relevant, functional phenotype of force production as well as mechanistic insights into the role of Ca^{2+} handling and transcriptomic dysregulation in dystrophic cardiac function, ultimately providing a powerful platform for further studies in disease modeling and drug discovery.

3.2 Introduction

Duchenne muscular dystrophy (DMD) is characterized by profound skeletal muscle weakness and wasting, but the leading cause of death in these patients is congestive heart failure downstream of dilated cardiomyopathy [1]. DMD and Becker muscular dystrophy (BMD), the less severe form of the disease, are caused by a lack of full-length dystrophin, a long, rod-shaped protein that localizes to the sarcolemma, where it anchors the sarcolemma to the extracellular matrix and the intracellular cytoskeleton through recruitment of the dystroglycan complex [2]. Dystrophin deficiency causes increased cell fragility and vulnerability to contraction-induced cell damage, leading to cycles of cardiac degeneration along with a gradual accumulation of non-contractile fibrotic tissue as the disease progresses [3]. Lack of dystrophin also has pleiotropic effects on cardiomyocyte function, including Ca^{2+} dysregulation [4, 5], nitric oxide dysregulation [6, 7], and mitochondrial dysfunction [8, 9], leading to oxidative damage and cell death [10, 11]. Dystrophin expression first occurs early in cardiac development [12, 13], thus, a lack of functional dystrophin likely affects cardiac development well before the presentation of clinical symptoms [14, 15]. However, the cellular mechanisms by which dystrophin deficiency leads to cardiac dysfunction at the organ level are not well understood, further complicated by limitations of current disease models. As such, the development of improved human in vitro disease models would be of great benefit to the field.

Current models are insufficient to fully elucidate the mechanisms of cardiomyopathy progression in DMD, as commonly used animal models have only mild and late-onset cardiac phenotypes and fail to recapitulate the human condition. The *mdx* mouse [16], although relied

upon heavily to advance our understanding of DMD, displays a minimal reduction in average lifespan when compared to human patients and presents minimal disease phenotypes or clinical indicators of cardiomyopathy until much later in disease progression [17, 18]. This lack of clinically relevant symptoms is often accompanied by spontaneous rhabdomyosarcoma, something not seen in human DMD patients [19]. Larger animal models, while often presenting more severe disease phenotypes, are limited by disease phenotype variability, high maintenance costs, and ultimately, a lack of relevant human physiology [20]. Additionally, given ethical concerns surrounding the use of animal in research, there is a desire to reduce and replace the use of animal models. Hence, there exists a need for human models of DMD suitable for preclinical studies to validate the molecular drivers of cardiac and skeletal muscle pathology and test genetic and small molecule therapeutics quickly and inexpensively.

Human induced pluripotent stem cell-derived cardiomyocytes (hiPSC-CMs) have emerged as a useful tool to study the multiple facets of dystrophin function not easily explored with animal models [21]. These stem cell-derived models have successfully replicated many known dystrophic phenotypes observed in DMD patients, including membrane fragility, Ca^{2+} handling and electrophysiological abnormalities, mitochondrial damage, and impaired force production [21–30]. However, hiPSC-CMs grown in 2D tissue culture platforms are limited by an immature cardiac phenotype, requiring long-term culture or a combination of structural and biochemical cues to promote sufficient maturation and accentuate the multifaceted dystrophic phenotype [23, 31]. These 2D platforms also subject cells to non-physiologic culture conditions and rely on single-cell measures, all of which limit the ability to capture an accurate and complete representation of cardiac function in both the normal and diseased states. 3D cardiac tissue engineering holds promise to produce models that more accurately mimic dystrophic cardiomyopathy in vitro.

We have previously developed engineered heart tissues (EHTs) that provide a 3D, physiological cell culture platform that allows for the assessment of hiPSC-CM auxotonic contractile function under uniaxial tensile load [32–34]. The EHT platform consists of hiPSC-CMs and stromal cells suspended in a fibrin hydrogel between two silicone posts, one flexible and one rigid, that forms synchronously contracting tissues, allowing for measurement of contractile force and kinetics. EHTs promote uniaxial cell alignment and physiological auxotonic contractions, which have been shown to improve cardiac maturation beyond what is achieved in 2D culture [35–39]. We hypothesize that the EHT platform will provide the environment necessary to expose the structural and physiological differences between normal and dystrophin-deficient heart muscle in vitro.

In this study, we generated EHTs from genetically-edited hiPSC-CMs harboring a dystrophin-truncating mutation (DMD 263delG) [31, 40]. Compared to isogenic controls, we observed that DMD 263delG EHTs display reduced contractile force and delayed kinetics of force development and relaxation. This was observed in addition to impaired sarcomere development, as dystrophic EHTs were found to have shorter sarcomere lengths. Dystrophic EHTs were also found to have increased cytosolic Ca^{2+} levels, slowed Ca^{2+} transient kinetics, and a higher incidence of irregular beat intervals as compared to isogenic controls. Transcriptome sequencing indicated dysregulation of several biological processes in DMD 263delG EHTs, including those related to heart development and contraction, Ca^{2+} and membrane potential homeostasis, and organization of the extracellular matrix. These results demonstrate that the EHT platform provides sufficient maturational cues to expose multiple facets of the DMD phenotype in a single platform. The results of this and future studies will continue to uncover and refine our understanding of the mechanisms by which dystrophin deficiency leads to heart failure early in disease progression and provide a platform for testing new genetic and small molecule therapies.

3.3 Methods

3.3.1 Stem cell culture and directed cardiac differentiation

A urine-derived hiPSC line from a healthy male donor (control) was established as previously described [22]. An isogenic diseased cell line harboring a dystrophin mutation (DMD 263delG) was generated from the control cell line via the deletion of a single base pair in Exon1 of the DMD gene with CRISPR-Cas9 as previously described [31]. Undifferentiated hiPSCs were maintained in mTeSR1 (Stemcell Technologies) on tissue culture plates coated with a 1:60 dilution of Matrigel (Corning). Cardiomyocyte directed differentiation was performed using a modified small molecule Wnt-modulating protocol optimized to each cell line as previously described [41]. Briefly, hiPSCs were seeded at 1.5 – 2.5 $\times$ 10^5 cells/cm^2 on Matrigel-coated plates in mTeSR1 with 10 μM Y-27632 ROCK inhibitor (Tocris). Cells were maintained in mTeSR1 with daily media changes until they reached confluency, which was typically 2 to 3 days after initial seeding. The initiation of directed differentiation (day 0) was defined by changing the media to RPMI 1640 (Gibco) plus B-27 supplement minus insulin (Life Technologies) and 12-14 μM Chiron 99021 (Axon Medchem) to activate Wnt/β-catenin signaling via inhibition of glycogen synthase kinase-3β (GSK-3β). After 24 h (day 1), media was changed to RPMI with B-27 minus insulin. On day 3, media was changed to RPMI with B-27 minus insulin and 5 μM IWP-4 (Stemgent) to inhibit Wnt/β-catenin signaling. On day 5, media was changed to RPMI with B-27 minus insulin. On day 7, the media was changed to RPMI with B-27 supplement (with insulin) and media was subsequently changed every 2-3 days. All differentiation steps were performed in 12-well plates with media volumes of 2 mL per well. hiPSC-CMs were replated into 10 cm dishes on day 14 to prepare for lactate enrichment. On days 16 and 18, media was changed to DMEM without glucose (Gibco) supplemented with 4 mM sodium L-lactate (Sigma-Aldrich) to enrich for cardiomyocytes. Cells were returned to RPMI with B-27 supplement plus insulin and cultured until day 25-27. Prior

to EHT casting, cardiomyocyte purity (>90%) was evaluated by flow cytometry for cardiac troponin T (**Fig 3.1**). All cell culture media was supplemented with 100 U/mL penicillin-streptomycin.

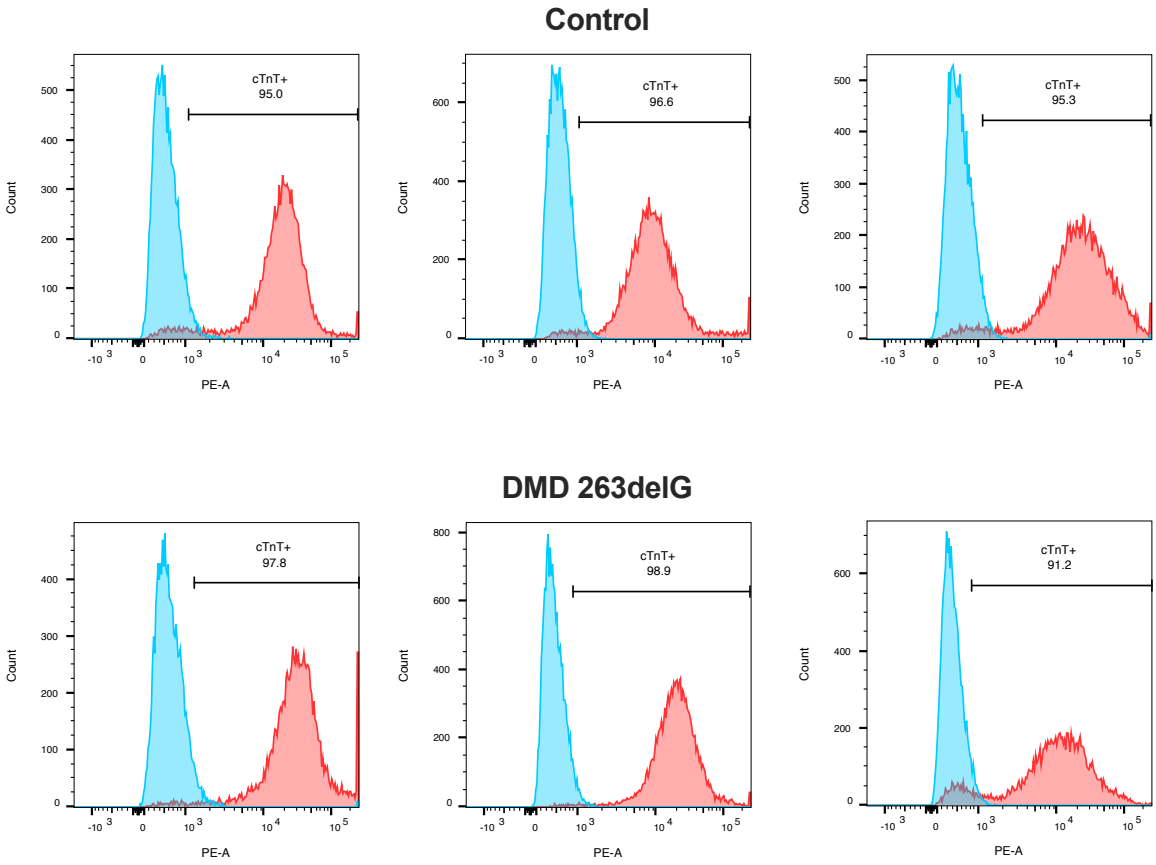

Figure 3.1. Flow cytometric analysis of hiPSC-CM purity. All batches of control (above) and DMD 263delG (below) hiPSC-CMs used in casting EHTs were confirmed to contain >90% cardiomyocytes are measured by cardiac troponin T (cTnT) expression. Red peaks indicate cTnT-stained samples and blue peaks indicate IgG-stained negative controls.

3.3.2 EHT platform and generation

The EHT post platform was designed and fabricated as described previously, resulting in racks of six pairs of posts measuring 12 mm long and 1.5 mm in diameter with a cap [32–34]. Briefly, uncured polydimethylsiloxane (PDMS, Sylgard 184 mixed at a 10:1 ratio of base to curing agent) was poured into a four-part acrylic mold with a glass capillary tube (Drummond, Cat #1-

000-0500) inserted into one post of each pair to make it rigid. Posts were left to cure at room temperature for 24 h then baked at 65 °C overnight to cure completely before being separated from the mold. Prior to EHT casting, PDMS posts were submerged in 70% ethanol for 10 min, rinsed with sterile deionized water for 10 min, then UV sterilized for 10 min. The PDMS had a modulus of elasticity of 2.5 MPa, so the bending stiffness of the flexible post in each pair was calculated to be 0.95 μN/μm, as previously described [32, 42].

EHTs were cast on day 25-27 of cardiac differentiation as previously described [33, 34]. Briefly, rectangular 2% agarose casting molds were prepared in 24-well tissue culture plates using 3D-printed spacers. Each rack of PDMS posts was positioned upside down with the tips of posts centered in the agarose wells. A solution of 100 μL volume consisting of 7.5×10^5 hiPSC-CMs and 5×10^4 HS27a human bone marrow stromal cells (ATCC) in RPMI with B-27 with 5 mg/mL bovine fibrinogen (Sigma-Aldrich) and 3 U/mL thrombin (Sigma-Aldrich) was pipetted into each agarose well. The mixture was incubated at 37 °C for 80 min to form EHTs suspended between pairs of posts and then transferred into a new 24-well plate with EHT media (RPMI with B-27 supplemented with 5 mg/mL aminocaproic acid, Sigma-Aldrich) for culture. EHT media was exchanged every 2-3 days for 3 weeks before subsequent analysis.

3.3.3 Contractile force measurement

EHTs were placed in a Tyrode's buffer (1.8 mM $CaCl_2$, 1 mM $MgCl_2$, 5.4 mM KCl, 140 mM NaCl, 0.33 mM NaH_2PO_4, 5 mM glucose, pH 7.35) at 37 °C for contractile analysis. A custom pacing apparatus with carbon electrodes built to fit a 24-well plate was used with an electrical stimulator (Astro Med Grass Stimulator, Model S88X) to provide biphasic field stimulation at 1.5 Hz (5 V/cm for 10 ms duration) during imaging [33]. Videos of EHT contraction were taken at 66.7 frames per second using an ORCA-Flash4.0 C13440 CMOS camera (Hamamatsu) on a Nikon TEi epi-fluorescent microscope with a 2× objective and 0.7× coupler, providing 4.64 μm/pixel resolution and a field of view of 9.5 mm × 9.5 mm, which was sufficient to visualize the full length

of the EHTs and the tips of both posts. A custom MATLAB script was used to track the deflection of the flexible post relative to the rigid post and from this analysis, we calculated twitch force, shortening velocity, time to peak, time to 50% and 90% relaxation, active twitch power, and total twitch work, as previously described [42, 43]. Briefly, twitch force was calculated by subtracting the tissue force minima from the following maxima and contraction kinetic metrics were calculated from the unnormalized tissue force traces. Shortening velocity was calculated as the maximum derivative of tissue force of each EHT contraction. EHT cross-sectional area was calculated assuming an elliptical cross section with a measured tissue width and conservatively estimated thickness of 500 μm. Specific force was then calculated by dividing the twitch force of each EHT by its cross-sectional area. For each EHT, analysis was performed on five consecutive contractions.

3.3.4 Beat interval irregularity measurement

Before initiation of electrical pacing, video recordings of spontaneously beating EHTs were taken to assess beat rate variability as previously described [23, 44]. Briefly, EHTs were submerged in Tyrode's buffer at 37 °C and a video of the flexible post was recorded for 60 s at 10 frames per second during spontaneous contraction. Post deflection was tracked and beat intervals (BI) were measured using a custom MATLAB script. BI were identified using a noise tolerant, peak finding algorithm that identifies local maxima that are greater than a threshold of one-fourth the amplitude of the data above the minimum. BI irregularity (ΔBI) was calculated as the difference between subsequent BI ($\Delta BI = BI_{n+1} - BI_n$).

3.3.5 Calcium transient measurement

Ca^{2+} transients in EHTs were assessed using the ratiometric Ca^{2+} indicator dye Fura-2 AM (Invitrogen), under 1.5 Hz electrical stimulation in Tyrode's buffer at 37 °C. To load Fura-2, EHTs were incubated in EHT media with 5 μM Fura-2 AM for 1 h followed by a washout period of

30 min in EHT media before being transferred to Tyrode's buffer. Two custom filter cubes (Chroma) were used to excite the dye at 365 nm or 380 nm and capture its emission at 510 nm. Excitation at 365 nm is near the isosbestic point of Fura-2 (360 nm) while emission intensity with 380 nm excitation decreases with increasing Ca^{2+} levels. Videos were taken at 50 frames per second on an ORCA-Flash4.0 C13440 CMOS camera (Hamamatsu) on a Nikon TEi epi-fluorescent microscope with a 2x objective and 0.7x coupler as described. To enable ratiometric Ca^{2+} assessment, a series of three videos of EHT contraction were taken sequentially at 365 nm, 380 nm, and again at 365 nm excitation. These videos were then analyzed with a custom MATLAB script to track the position of the flexible post and determine the average pixel intensity within the EHT area during contraction. The fluorescence intensity of the two 365 nm excitation recordings at the start and end of the experiments were averaged to account for any effects of photobleaching of the dye. The average was then used in calculating a ratio of baseline fluorescence intensity at 365 nm excitation over the dynamic fluorescence intensity at 380 nm excitation due to changes in the concentration of intracellular Ca^{2+}. The 365nm/380nm ratio was then used to calculate the kinetics of the Ca^{2+} transient, including time to peak, time to 50% decay, and rate to 50% decay. For each EHT, analysis was performed on 5 consecutive contractions.

3.3.6 Immunoblot

Protein lysates were obtained from a subset of individual EHTs after force and Ca^{2+} measurements using an ice-cold RIPA buffer supplemented with 2% protease inhibitor cocktail (Sigma P8340). Individual EHTs were homogenized in 75–100 µL of buffer using a micro-homogenizer with a 5 mm probe (VWR). Samples were lysed on ice for 30 min, then spun down at 21,000 *g* for 10 min at 4 ºC to remove cellular and matrix debris. The supernatant was isolated and protein concentration was measured using the Pierce BCA Protein Assay Kit (Thermo Fisher Scientific) according to manufacturer's instructions.

Samples were prepared for electrophoresis by adding 4× Laemmli Sample Buffer (Bio-Rad) and 2.5% β-mercaptoethanol, after which samples were denatured at 95 ºC for 10 min. Protein was loaded into 4–15% Mini-PROTEAN TGX Stain-Free Gel at 50 µg per sample and run at 100 V for 80 min in 1× Tris/Glycine/SDS running buffer (Bio-Rad). Protein gels were transferred onto Immun-Blot LF PVDF membranes (Bio-Rad) overnight at 30 V and 4 ºC in 1× Tris/Glycine buffer (Bio-Rad) with 10% methanol. Membranes were blocked in Blocker FL Fluorescent Blocking Buffer (Thermo Fisher Scientific) for 1 hour at room temperature. Primary antibodies against dystrophin (Abcam 15277, 1:1000), β-dystroglycan (DSHB MANDAG2(D11), 1:1000), and GAPDH (Sigma SAB4300645, 1:1000) were diluted in blocking buffer and incubation was performed overnight at 4 ºC with agitation. Membranes were washed three times for 5 min in TBS-T at room temperature, then incubated for 1 hour at room temperature with species-matched AlexaFluor-conjugated secondary antibodies (Invitrogen, 1:1000) diluted in blocking buffer with agitation. Membranes were again washed three times for 5 min in TBS-T before imaging on a ChemiDoc MP imaging system (Bio-Rad). Before re-probing for other targets, membranes were stripped of antibodies with Restore Plus Western Stripping Buffer (Thermo Fisher Scientific) for 10 minutes, then washed 3 times for 10 minutes in TBS-T at room temperature. Densitometric quantification of western blot band intensity was performed using ImageJ and protein levels were normalized to the level of GAPDH in the sample.

3.3.7 Immunofluorescent imaging and quantitative sarcomere analysis

A subset of EHTs were processed for histology as previously described [33]. Briefly, following force and Ca^{2+} assessment, EHTs were submerged in 140 mM KCl for 1 min to inhibit contraction and induce EHT relaxation followed by fixation in 4% paraformaldehyde in DPBS for 15 min. EHTs were then washed with DPBS and dehydrated in a 30% w/v sucrose solution overnight at 4 °C. EHTs were removed from the posts and embedded in O.C.T. compound. Longitudinal and transverse cryosections of 20 µm thickness were used for histology. Sections

were blocked and permeabilized with 1% BSA and 0.1% Triton X-100 for 30 min at room temperature, followed by overnight incubation at 4 °C with mouse primary antibodies against α-actinin (Sigma-Aldrich A7811, 1:800) or dystrophin (Leica NCL-DYS1 (monoclonal, 1:30) or Abcam 15277 (polyclonal, 1:200). The following day, sections were incubated with donkey anti-mouse Alexa Fluor 488, donkey anti-rabbit Alexa Fluor 555, or goat anti-mouse Alexa Fluor 594 (Invitrogen, 1:200), and Alexa Fluor 488 phalloidin (Invitrogen A12379, 1:150), for 1 hour at room temperature. Cover slides were mounted with ProLong™ Gold Antifade Mountant with DAPI (Invitrogen). Images were taken on a Leica SP8 confocal microscope. Laser strength and gain were kept constant between all samples and fields of view. Resting sarcomere length and alignment were calculated using α-actinin stained images and a scanning gradient Fourier transform program in MATLAB, as previously described [45]. Z-disk width was calculated using a custom MATLAB script that thresholds and measures the major axis length of α-actinin stained images. Dystrophin stain intensity was quantified by applying a threshold mask to images to select cell area then averaging the pixel intensity within the mask.

3.3.8 RNA sequencing

Following force and Ca^{2+} assessments, a subset of EHTs were removed from posts and stored in RNAlater (Ambion) at -80 ºC. Lactate enriched, age-matched hiPSC-CMs (7 weeks post differentiation) were similarly stored in RNAlater at -80 ºC. Individual EHTs and hiPSC-CM samples were sent to BGI genomics for RNA extraction and 100 base pair paired-end transcriptome sequencing on the DNBseq platform with 50 million reads per sample. Reads were aligned to the human genome using Rsubread (Bioconductor) to GENCODE GRCh38.p13 [46]. Aligned reads were then counted using featureCounts (Bioconductor), excluding chimeras, multi-mapping genes, multi-overlap, and single end genes, resulting in roughly 20 million counts per individual EHT [46]. Differential expression analysis was performed using edgeR (Bioconductor) and the following criteria: counts > 10, $p < 0.05$, $|\log(FC)| > 0.3$, FDR < 0.05 [47]. Gene ontology

(GO, 02/2021 release) analysis was performed with clusterProfiler (Bioconductor) [48]. The RNA sequencing datasets described in this study can be accessed in the NCBI Gene Expression Omnibus (GEO) repository with accession ID GSE199242.

3.3.9 Biological replicates and statistical analysis

The data shown herein represent EHTs pooled from multiple experimental replicates as indicated, where an independent experiment refers to a batch of EHTs made from an independent differentiation. The data encompasses up to three independent experiments with 6–12 tissues per batch, as indicated in figure legends. All data points shown in figures represent values for a single EHT and different symbols designate separate experiments. All values are reported as mean ± standard error of the mean (S.E.M.) unless indicated otherwise. Results were compared using an unpaired, two-tail t-test unless indicated otherwise and differences with a p-value < 0.05 were considered statistically significant as denoted with an asterisk.

3.4 Results

3.4.1 Generation of EHTs from dystrophin-mutant hiPSC-CMs

Control hiPSCs were generated from urine derived cells from a healthy donor as previously described [22]. The control line was genetically edited using CRISPR-Cas9 to generate an isogenic match that harbored a dystrophin-truncating mutation (DMD 263delG) [31, 40]. Briefly, the DMD 263delG line has a single base pair deletion within the first exon of the *DMD* gene, resulting in the expression of a truncated isoform of dystrophin lacking a significant portion of the actin-binding domain (exons 1-6) (**Fig 3.2A**). N-terminal *DMD* mutations are known to cause more severe cases of Becker's muscular dystrophy [49]. Both control and DMD 263delG hiPSCs were subjected to directed cardiomyocyte differentiation and used to generate EHTs by casting hiPSC-CMs in a fibrin gel between two silicone posts, one flexible and one rigid (**Fig 3.2B**). Both control and DMD 263delG hiPSC-CMs generated EHTs that compacted in size between the posts and

began to generate observable spontaneous contractions within one week of casting (**Fig 3.2C**). Both control and DMD hiPSC-CMs produced EHTs of similar resting length and cross-sectional area, indicating that EHT compaction, and therefore resting tissue force and stress, was consistent between the two lines (**Fig 3.3**). Western blot analysis using a polyclonal antibody against the C-terminal domain of dystrophin showed similar expression levels of dystrophin protein in control and DMD 263delG EHTs (**Fig 3.2D-E**). Additionally, we observed lower-trending expression of β-dystroglycan, another dystroglycan complex protein, in DMD 263delG EHTs (**Fig 3.2D-E**), recapitulating the most recent demonstration of dystroglycan protein complex assembly in hiPSC-CMs [50]. However, while immunocytochemical analysis of sarcomeric F-actin confirmed the presence of uniaxially aligned sarcomeres in control and DMD 263delG EHTs, an antibody targeting the rod domain of dystrophin (exons 26-30) indicated a high amount of the full-length protein in the control EHTs and only a trace amount of the truncated protein in the DMD 263delG EHTs (**Fig 3.2F, Fig 3.4**). Similarly, in transverse sections, we observed that dystrophin localized strongly to the cell membrane in control EHTs, while less dystrophin appeared at the cell membrane in DMD 263delG EHTs (**Fig 3.2G**). Together, these results suggest that while there was equivalent total expression of dystrophin in the DMD 263delG EHTs as seen by western blot, there is decreased localization of this truncated dystrophin to the cell membrane as seen by immunofluorescence. The observed decrease in β-dystroglycan further supports this hypothesis of impaired dystroglycan protein complex formation in the absence of full-length dystrophin.

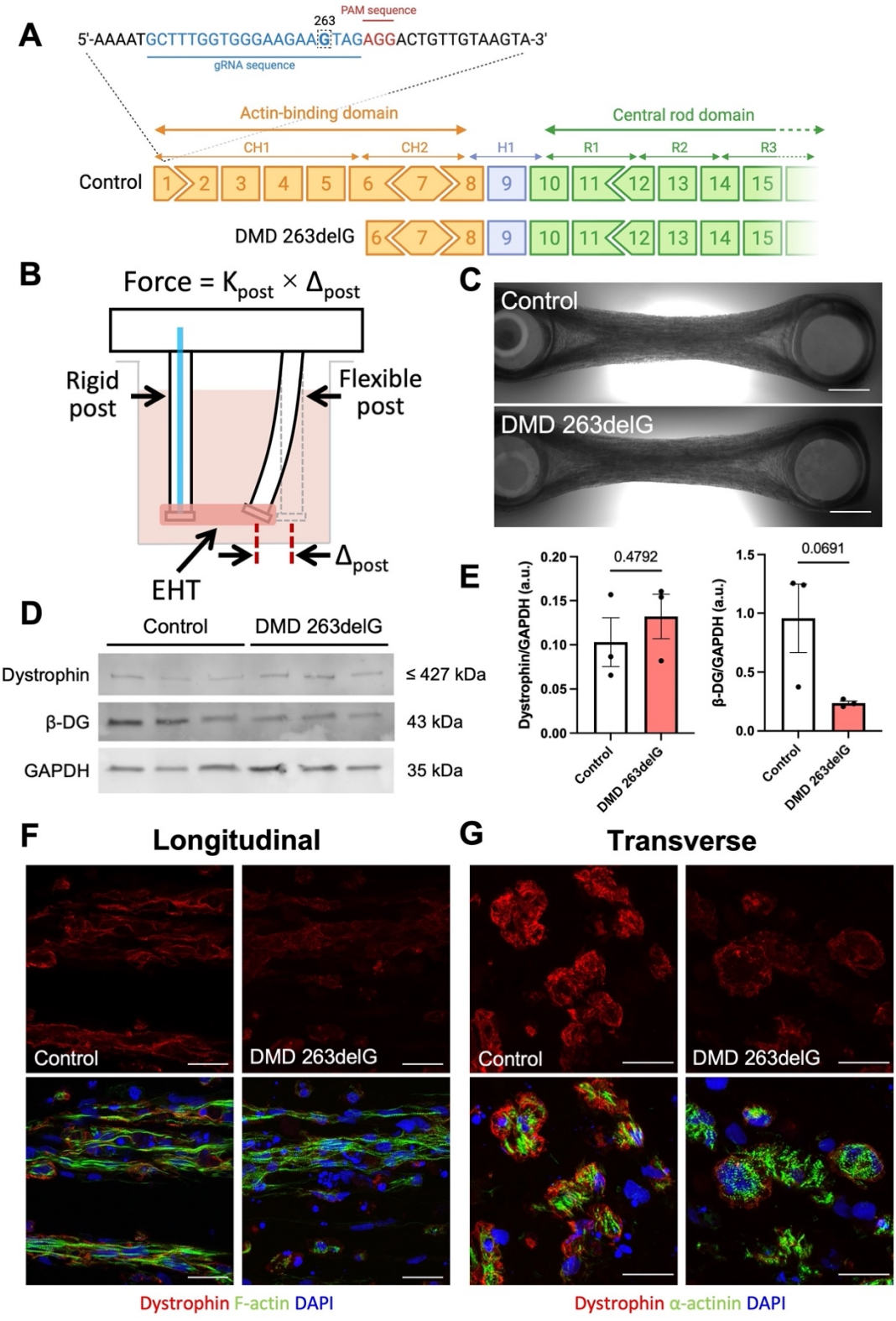
A
263
PAM sequence
5'-AAAATGCTTTGGTGGGAAGAAGTAGAGGACTGTTGTAAGTA-3'
gRNA sequence
Actin-binding domain
Central rod domain
CH1
CH2
H1
R1
R2
R3
Control
DMD 263delG
B
Force = Kpost × Δpost
Rigid post
Flexible post
Δpost
EHT
C
Control
DMD 263delG
D
Control
DMD 263delG
Dystrophin
β-DG
GAPDH
≤ 427 kDa
43 kDa
35 kDa
E
Dystrophin/GAPDH (a.u.)
0.4792
β-DG/GAPDH (a.u.)
0.0691
Control
DMD 263delG
F
Longitudinal
G
Transverse
Dystrophin F-actin DAPI
Dystrophin α-actinin DAPI

Figure 3.2. Human engineered heart tissues as a model of DMD. Human engineered heart tissues as a model of DMD. (A) Schematic of the CRISPR gene editing strategy that targeted the first exon of the DMD gene, resulting in the deletion of G263 to generate the DMD 263delG cell line which expresses a truncated protein missing the actin-binding domain up to exon 6. (B) Schematic diagram showing an EHT attached to two posts, one flexible and one rigid, in culture. The force of EHT contraction can be quantified using the stiffness (K_{post}) and measured deflection (Δ_{post}) of the flexible post. (C) Representative images of control DMD 263del EHTs with the rigid post on the left and the flexible post on the right. Scale bars = 1 mm. (D) Western blot analysis of dystrophin and β-dystroglycan (β-DG) expression in individual control and DMD 263delG (DMD) EHTs, with GAPDH as a loading control (n = 3). (E) Normalized protein level of dystrophin and β-dystroglycan based on loading control GAPDH (n = 3, p-values indicated). (F) Immunofluorescent images of longitudinal EHT sections stained for dystrophin (Leica NCL-DYS1, red), F-actin (Phalloidin, green), and nuclei (DAPI, blue). Scale bars = 50 μm. (G) Immunofluorescence images of transverse sections of control and DMD 263delG EHTs stained with antibodies for dystrophin (Abcam 15277, red), α-actinin (green), and nuclei (blue). Scale bars = 25 μm.

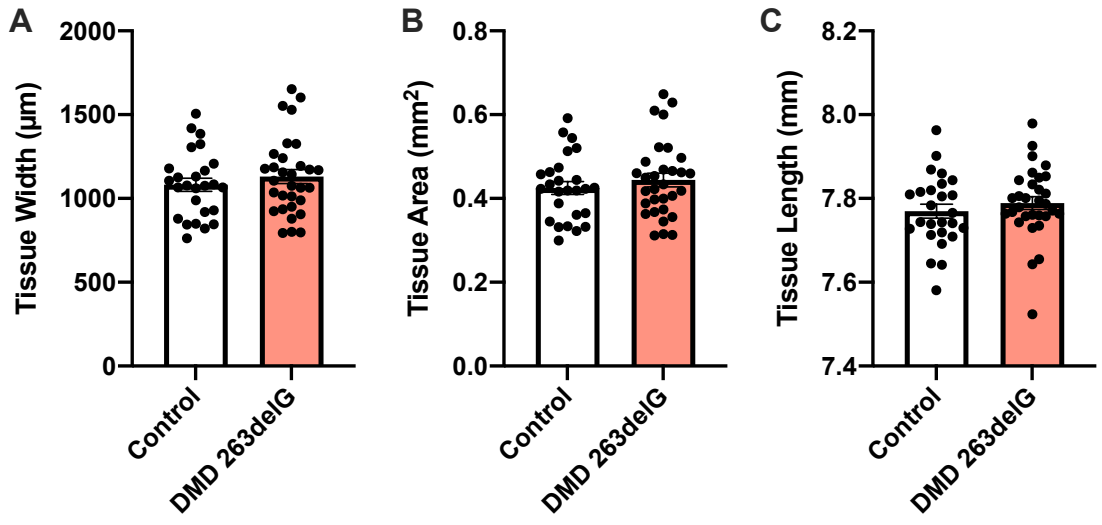

Figure 3.3. Consistency in EHT compaction after 3 weeks in culture. (A) Width of control and DMD 263delG EHTs as measured from recorded images. (B) Estimated EHT cross-sectional area calculated as an ellipse from the measured tissue width and an estimated 500 μm tissue thickness (Area = π × width × thickness). (C) Total EHT length as measured from recorded images, illustrating the occurrence of compaction from the original 8 mm starting EHT length. Data shown represent all replicates from three independent experiments (Control n = 27, DMD 263delG n = 30).

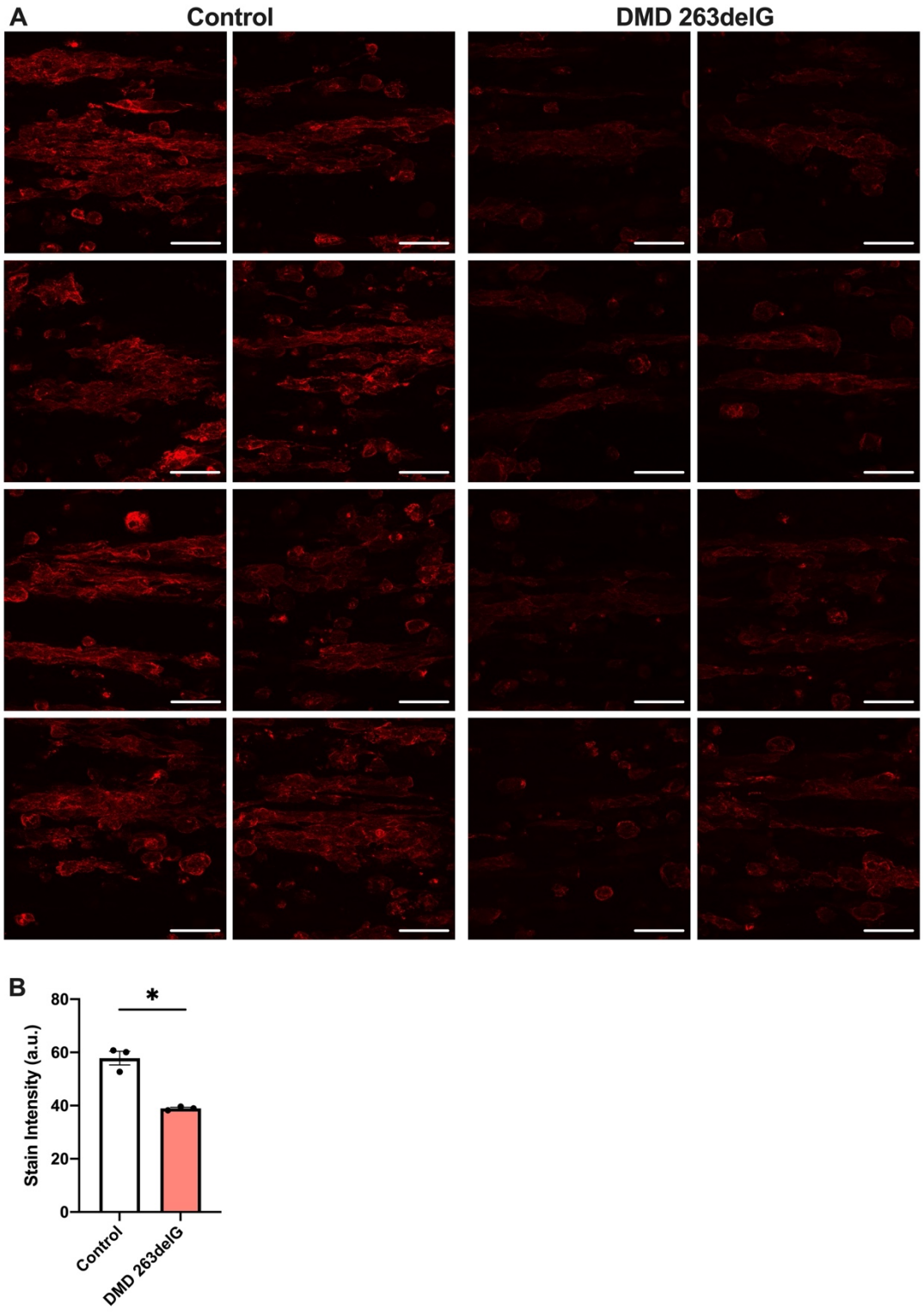

Figure 3.4. Dystrophin expression measured by immunofluorescence imaging. (A) Control and DMD 263delG EHTs were stained with an antibody targeting the rod domain of dystrophin (exons 26-30), indicating a high amount of

the full-length protein in the control EHTs and a trace amount of the truncated protein in the DMD 263delG EHTs. Scale bars = 50 μm. (B) Quantification of dystrophin stain pixel intensity, each data point represents the average of multiple images from a single EHT.

3.4.2 Transcriptional phenotype of DMD hiPSC-CMs and EHTs

We performed RNA-sequencing on age-matched hiPSC-CMs and EHTs to investigate the transcriptomic effects of 3D EHT culture downstream of the DMD 263delG mutation (**Fig 3.5A**). We observed that 2D cell culture produced more differentially expressed genes (DEGs, $|\log(FC) > 0.3|$, $p < 0.05$, FDR < 0.05, n = 3) between control and DMD 263delG samples than EHTs (4,233 DEGs for 2D cell culture versus 1,527 DEGs for EHTs) (**Fig 3.5B**). Interestingly, there appeared to be very little overlap between DEGs upregulated or downregulated as a result of the DMD 263delG mutation in 2D cell culture when compared to EHTs. To better demonstrate the differences between 2D and EHT culture, we compared the top 30 upregulated and downregulated gene ontology (GO) biological processes (BP) as ranked by p-value (**Fig 3.5C-D**). When comparing 2D control and DMD 263delG hiPSC-CMs, very little emerges that is relevant to dystrophin function or cardiac biology. Interestingly, while there was a downregulation of genes related to heart development and cardiac muscle cell action potential, the majority of BP terms relate to a large upregulation in mitochondrial function and ATP generation, with downregulation of BPs related to neural development, epithelial morphogenesis, and hemostasis (**Fig 3.5C**). Conversely, when comparing control and DMD 263delG EHTs, we observed dysregulation of many BPs relevant to cardiac function, including many related to heart and cardiac muscle development, cardiac action potential and muscle contraction, as well as extracellular matrix organization (**Fig 3.5D**). These results suggest that the *DMD* 263delG mutation does not have a profound effect on the cardiac-specific transcriptome in 2D culture, perhaps due to decreased hiPSC-CM maturity in this less physiologically-relevant culture platform, while the uniaxial, 3D culture provided by EHTs produces a disease-relevant transcriptomic response.

A closer analysis of the transcriptional changes that occurred in DMD 263delG EHTs reveals potential mechanisms driving the dystrophic phenotype presented in EHTs. Direct comparison of a subset of DEGs with the highest fold change revealed a hierarchical clustering that clearly delineates the two genotypes (**Fig 3.5E**). GO analysis indicated dysregulation of several key BPs including those related to cardiac muscle tissue development, heart contraction, regulation of membrane potential, calcium ion homeostasis, and extracellular matrix organization (**Fig 3.5F**). Further inspection of key genes identified by GO analysis indicates potential drivers of the dystrophic phenotype presented in EHTs (**Table 2.1**). Interestingly, we observed increased expression of *DMD* mRNA in DMD 263delG EHTs, potentially indicating an attempted compensatory mechanism for the dysfunctional mutant dystrophin protein. Ultimately, we observed that 3D EHT culture produces transcriptional changes relevant to cardiac biology, suggesting multiple mechanisms driving the dystrophic phenotype produced as a result of a lack of full-length dystrophin.

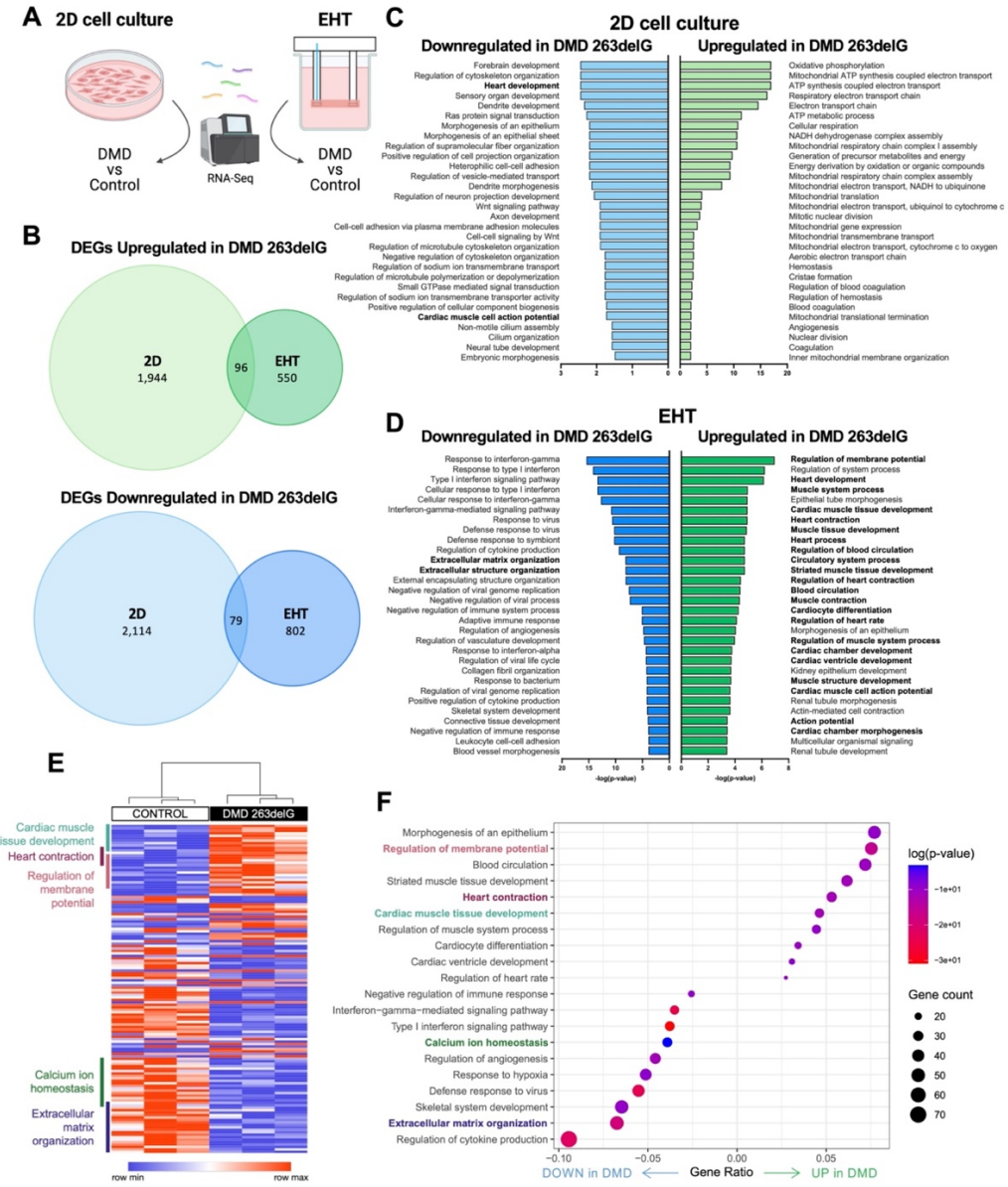

Figure 3.5. Transcriptome dysregulation in DMD 263delG hiPSC-CMs and EHTs. (A) Schematic of RNA-sequencing experiment where control and DMD 263delG hiPSC-CMs (7 weeks post differentiation) were compared and control and DMD 263delG EHTs (4 weeks post differentiation + 3 weeks EHT culture) were compared in separate experiments (n = 3). (B) Venn diagrams comparing the number of differentially expressed genes (DEGs) that were upregulated or downregulated in DMD 263delG 2D hiPSC-CMs and EHTs. (C) Top gene ontology (GO) processes up- or downregulated in DMD 263delG hiPSC-CMs and (D) EHTs, as ranked by p-value. GO terms relevant to cardiac biology appear in bold typeface. (E) Heatmap of a subset of normalized DEGs in control and DMD 263delG EHTs with hierarchical clustering represented by dendrogram (n = 3). Highlighted areas indicate genes corresponding to GO processes. (F) GO analysis of DEGs in DMD 263delG versus control EHTs.

Table 3.1. Biological processes of interest from gene ontology (GO) analysis of EHTs.

GO ID	Description	Gene Ratio	Adjusted p-value	Genes
Upregulated in DMD				
GO:0042391	Regulation of membrane potential	44/584	1.12E-07	*NRXN1, GJA5, GABRB2, CACNA1G, KCNJ3, RGS4, ANK3, ATP2A2, PLN, MEF2C, RNF207, RYR2, SCN5A, AKAP6, NETO1, BVES, USP53, SLC8A1, CACNA1C, DMD, KCNK1, POPDC2, ATP1B2, KCNK2, NNT, NDUFS1, ATP1B1, GOT1, FGF12, SCN3B, INSYN2A, KCNQ3, CUX2, BCO2, IGSF11, POPDC3, GRIN3A, RELN, RTL10, NLGN4X, MYH14, RIMS4, SEZ6, SLC25A27*
GO:0048738	Cardiac muscle tissue development	27/584	1.16E-05	*MYH6, RGS4, TBX3, PDLIM5, S1PR1, TTN, MYH11, PLN, MEF2C, RYR2, NEBL, FHOD3, WNT5A, MYOCD, MYBPC3, BMP7, BMP5, AKAP6, BVES, SLC8A1, PROX1, ADAMTS9, KCNK2, TBX5, TGFB2, FOXC2, SGCD*
GO:0060047	Heart contraction	31/584	1.16E-05	*GJA5, MYH6, CACNA1G, KCNJ3, RGS4, TTN, ATP2A2, PLN, RNF207, CORIN, RYR2, MYBPC3, SCN5A, BVES, SLC8A1, CACNA1C, DMD, AGT, DES, KCNK1, POPDC2, ATP1B2, CELF2, TGFB2, ATP1B1, FGF12, SCN3B, CCN2, SPX, SEMA3A, SGCD*
GO:0014706	Striated muscle tissue development	36/584	1.85E-05	*MYH6, RGS4, TBX3, PDLIM5, S1PR1, TTN, MYH11, TLL2, PLN, MEF2C, MYOM2, NR1D2, RYR2, BTG2, NEBL, FHOD3, WNT5A, MYOCD, MYBPC3, BMP7, BMP5, AKAP6, GPCPD1, BVES, SLC8A1, POPDC2, PROX1, ADAMTS9, KCNK2, TBX5, TGFB2, FOXC2, POPDC3, SMO, SGCD, MYH14*
GO:0008015	Blood circulation	42/584	3.93E-05	*ANGPT1, GJA5, MYH6, DRD1, CACNA1G, KCNJ3, RGS4, CDH5, TTN, ATP2A2, PLN, SLIT2, RNF207, CORIN, SLC6A4, RYR2, MYBPC3, SCN5A, BVES, SLC8A1, CACNA1C, DMD, AGT, DES, KCNK1, POPDC2, ATP1B2, CELF2, TGFB2, ATP1B1, FGF12, SMTNL2, FOXC2, SCN3B, CCN2, ARHGAP42, SPX, SEMA3A, ADRB3, ZDHHC21, SGCD, FLI1*
GO:0035051	Cardiocyte differentiation	20/584	5.29E-05	*MYH6, RGS4, JAG1, TBX3, PDLIM5, TTN, MYH11, MEF2C, NEBL, FHOD3, VCAM1, MYOCD, PRICKLE1, BMP7, AKAP6, BVES, SLC8A1, PROX1, TBX5, TGFB2*
GO:0002027	Regulation of heart rate	16/584	7.24E-05	*MYH6, CACNA1G, KCNJ3, RGS4, ATP2A2, PLN, RYR2, SCN5A, BVES, SLC8A1, CACNA1C, DMD, POPDC2, SCN3B, SPX, SEMA3A*
GO:0002009	Morphogenesis of an epithelium	45/584	8.58E-05	*EPHA4, SFRP2, TGM2, IRX2, IRX1, MTSS1, NPNT, JAG1, TBX3, COL4A1, PBX1, SHROOM3, KIF26B, ROR1, SLIT2, MEF2C, RNF207, PDPN, NTN1, RYR2, WNT5A, PRICKLE1, BMP7, BMP5, DLC1, FERMT1, GPC3, AGT, DCHS1, PROX1, TBX5, CELSR1, RDH10, STARD13, TGFB2, FOXC2, FST, SEMA3A, OSR1, OPA1, SMO, HOXB4, TIE1, CYP7B1, FRZB*
GO:0090257	Regulation of muscle system process	26/584	0.000102	*FOXO1, GJA5, RGS4, ATP2A2, PLN, RNF207, RYR2, MYOCD, MYBPC3, MLIP, SCN5A, AKAP6, SLC8A1, PPARGC1A, CACNA1C, DMD, AGT, TRPC3, ATP1B1, PPP1R12B, CCN2, ARHGAP42, SPX, ZDHHC21, KIT, CALCRL*
GO:0003231	Cardiac ventricle development	18/584	0.000180	*GJA5, SFRP2, MYH6, JAG1, TBX3, SLIT2, MEF2C, RYR2, WNT5A, MYOCD, MYBPC3, SCN5A, PROX1, KCNK2, TBX5, TGFB2, FOXC2, ROBO2*
Downregulated in DMD				

GO:0060337	Type I interferon signaling pathway	28/742	4.13E-14	*USP18, IRF6, HLA-B, IFITM3, MX2, IFI6, HLA-C, GBP2, HLA-E, IFITM2, HLA-A, ISG15, EGR1, OAS2, STAT2, IRF7, SP100, IFITM1, PSMB8, BST2, OAS3, OAS1, IFIT3, NLRC5, IRF1, OASL, STAT1, IFIT2*
GO:0060333	Interferon-gamma-mediated signaling pathway	26/742	1.44E-11	*IRF6, HLA-B, TRIM38, ICAM1, HLA-C, GBP2, HLA-E, PML, HLA-A, TRIM22, OAS2, IRF7, SP100, PARP14, B2M, TRIM21, OAS3, OAS1, NLRC5, IRF1, OASL, PARP9, SOCS1, NMI, STAT1, HCK*
GO:0051607	Defense response to virus	41/742	5.15E-11	*DTX3L, SHFL, PLSCR1, IFITM3, IFI44L, TRIM56, MX2, IFI6, BNIP3L, DDIT4, DHX58, IFITM2, PML, ZC3HAV1, ISG15, EIF2AK2, TSPAN32, IFI16, TRIM22, OAS2, IFIH1, STAT2, IRF7, IFITM1, GBP3, DDX60, BST2, OAS3, SLFN11, OAS1, IFIT3, NLRC5, NLRP1, IRF1, OASL, ZC3H12A, PARP9, STAT1, UNC93B1, BNIP3, IFIT2*
GO:0001817	Regulation of cytokine production	70/742	4.12E-10	*IL20RB, SSC5D, CDH3, HLA-B, ERRFI1, C3, BTN3A2, LRP1, CD36, TRIM56, UBA7, INHBB, LUM, BTN3A1, DHX58, HLA-E, PML, CPTP, TGFB1, CD47, RUNX1, GATA3, RELB, HLA-A, ISG15, EIF2AK2, EGR1, CEBPB, DTX4, IFI16, LTF, IFIH1, CCN4, STAT6, IRF7, TRIB2, BCL3, UBE2L6, P2RX7, F3, B2M, GAPDH, TRIM21, HILPDA, GPNMB, ANXA4, BST2, SEMA7A, RARA, INHA, RPS3, UCN, NFATC4, NLRC5, ITGB8, DDIT3, NLRP1, IRF1, ZC3H12A, IL18, TSKU, SERPINB7, GDF2, MAPK13, SOCS1, POU2F2, NMI, LGALS9, STAT1, CCDC88B*
GO:0030198	Extracellular matrix organization	50/742	6.73E-09	*COL5A1, DCN, AGRN, JAM2, VWA1, WT1, LRP1, TNC, ICAM1, LOXL2, DPT, LOX, COL1A1, LUM, MMP2, COL6A2, COL1A2, ECM2, BGN, TGFB1, COL2A1, COL6A3, CD47, RUNX1, COL4A4, COL11A2, COL3A1, CREB3L1, ITGA6, NTNG1, BCL3, LOXL1, CCDC80, ITGA11, SPOCK2, SOX9, LOXL4, EMILIN1, COL5A3, MELTF, ADTRP, PECAM1, CTSS, ITGB8, OLFML2A, LAMB3, CSGALNACT1, TGFBI, ERO1A, COL10A1*
GO:0045765	Regulation of angiogenesis	34/742	1.42E-05	*AQP1, DCN, TNMD, C3, VEGFA, THBS2, PML, PTK2B, RRAS, RUNX1, EFNA3, YJEFN3, CREB3L1, VEGFB, SEMA3E, FGF1, PKM, SP100, RHOB, BTG1, CTSH, ANGPTL4, F3, VEGFC, GPNMB, PGK1, EMILIN1, ITGB8, NPPB, CCL11, ZC3H12A, BMPER, GDF2, STAT1*
GO:0001501	Skeletal system development	48/742	7.11E-05	*PRELP, LRRC17, ZNF385A, LOXL2, LOX, COL1A1, LUM, MMP2, EXTL1, RANBP3L, COL1A2, BGN, TGFB1, COL2A1, RARG, RUNX1, STC1, BBX, COL11A2, VKORC1, COL3A1, LTF, FGFR1, CCN4, HOXB9, HOXC10, PDGFC, UNCX, HOXC6, SOX9, HOXB7, INHA, HAND1, ACVR2A, ITGB8, FMN1, NOG, EVC, CSGALNACT1, TGFBI, WNT10B, TRPS1, TSKU, NKX3-2, GDF2, TBX15, COL10A1, HOXB5*
GO:0050777	Negative regulation of immune response	19/742	0.000125	*IL20RB, SERPING1, HLA-B, DHX58, HLA-E, IL13RA2, HLA-A, COL3A1, IFI16, LGALS3, PARP14, TRIM21, NLRC5, ZBTB7B, ZC3H12A, HLX, GPR17, NMI, LGALS9*
GO:0001666	Response to hypoxia	38/742	0.000152	*AQP1, PLOD2, ICAM1, VEGFA, LOXL2, NOL3, BNIP3L, DDIT4, PLOD1, MMP2, PML, PTK2B, CA9, STC1, ALKBH5, MALAT1, EGR1, VEGFB, ALAS2, LDHA, PKM, PSME1, AK4, PSMB8, NDRG1, ANGPTL4, PSMB9, VEGFC, HILPDA, BAD, PGK1, ITPR1, ENO1, ERO1A, NKX3-1, CPEB1, ANKRD1, BNIP3*
GO:0055074	Calcium ion homeostasis	29/742	0.0416	*CCL21, CAMK2N1, CASQ1, LRP1, CCL28, CD36, NOL3, PML, PTK2B, STC1, PTGFR, P2RX7, SLC8B1, ITPR1, CACNB3, NPFF, CSRP3, TRPM8, ATP1A2, DDIT3, CCL11, LPAR2, CCR1, GPR17, BDKRB2, ERO1A, DRD4, ATP2A3, BNIP3*

3.4.3 Decreased contractility and delayed contractile kinetics in DMD EHTs

Given the central role of dystrophin in maintaining mechanical integrity of the cell, it was of interest to assess the extent to which dystrophic EHTs are able to produce contractile forces. After 3 weeks in culture, control and DMD 263delG EHTs were subjected to auxotonic contractility assessment with electrical field stimulation at 1.5 Hz via optical measurement of the deflection of the flexible post. It was observed that DMD 263delG EHTs had a similar baseline tension as control EHTs but produced significantly decreased twitch forces (**Fig 3.6A-B**). Accordingly, DMD 263delG EHTs produced lower specific forces than the control EHTs when estimated cross-sectional areas were accounted for (**Fig 3.6C**). DMD 263delG EHTs were also observed to have lower twitch power, twitch work, and shortening velocity, as compared to control EHTs**,** illustrating an overall decrease in contractile performance (**Fig 3.6D-F)**. Normalized traces of tissue force (**Fig 3.6G**) reveal slower kinetics of contraction in DMD 263delG EHTs, which significantly increased the time to peak force and time to 50% relaxation (**Fig 3.6H-J**). Overall, these results indicate that the dystrophin mutation results in impaired contractile function in DMD 263delG EHTs.

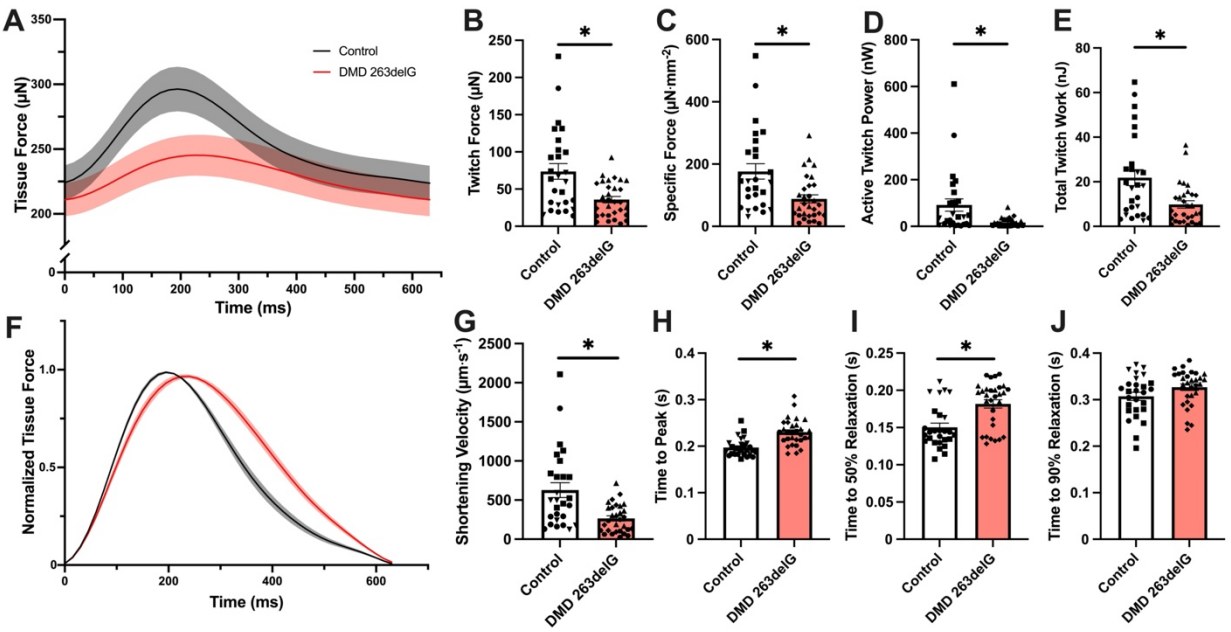

Figure 3.6. Auxotonic contractile properties of DMD 263delG EHTs. (A) Average tissue force traces of control and isogenic DMD 263delG EHTs. (B) Calculated maximum twitch force, (C) twitch stress, (D) active twitch power, (E) and total twitch work of EHT contraction. (F) Normalized average tissue force trace of control and isogenic DMD 263delG EHTs. (G) Calculated shortening velocity, (H) time to peak, (I) time to 50% relaxation, and (J) time to 90% relaxation. For (A) and (F), lines represent average ± S.E.M. Data shown represent all replicates from three independent experiments per cell line, different symbols represent different experimental batches (Control n = 27, DMD 263delG n = 30).

3.4.4 Altered sarcomere organization in DMD EHTs

To investigate the underlying causes of impaired contractility, we performed quantitative image analysis of myofibril structure. Specifically, control and DMD 263delG EHTs were stained for Z-disk protein α-actinin, and confocal images were analyzed with custom image analysis scripts. We observed that both the control and DMD 263delG EHTs generated cardiomyocytes that had sarcomeres aligned in the longitudinal direction (**Fig 3.7A**). Sarcomere length was quantified using a scanning-gradient Fourier transform [45]. We found that control EHTs had significantly longer sarcomeres as compared to DMD 263delG EHTs (**Fig 3.7B**). However, we

observed no significant difference in Z-disk width between control and DMD 263delG EHTs (**Fig 3.7C**). Additionally, it was observed that control and DMD 263delG EHTs had similar overall sarcomere alignment (**Fig 3.7D**). The observed shorter sarcomere spacing is consistent with the lower contractile forces observed in DMD 263delG EHTs.

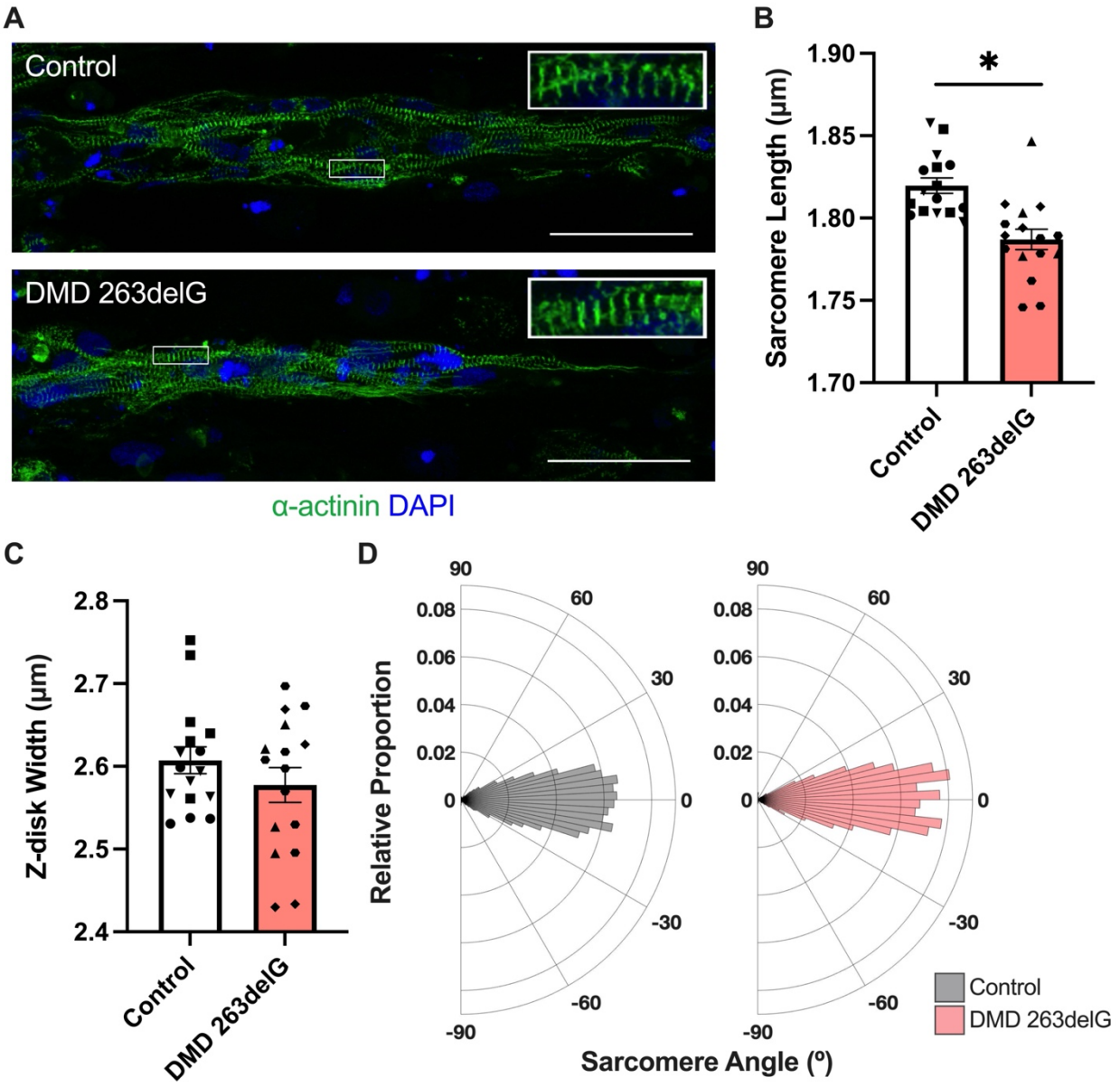

Fig. 3.7. Sarcomere structure in DMD EHTs. (A) Representative control and DMD 263delG EHTs stained for α-actinin (green) and nuclei (blue) from which sarcomere measurements were made. Insets show a magnified view of striated sarcomeres. (B) Average measured sarcomere length and (C) Z-disk width from histological images of control and

DMD 263delG EHTs. (D) Rose plots displaying distribution of sarcomere angles for all measured control and DMD 263delG EHTs (n = 16). Scale bars = 50 µm. Each data point represents an average of nine images for a single EHT. Data shown represent all replicates from three independent experiments, different symbols represent different experimental batches (Control n =16, DMD 263delG n = 16).

3.4.5 Altered calcium transients in DMD EHTs

It was of interest to investigate the Ca^{2+} transients of dystrophic EHTs, as previous studies have pointed to Ca^{2+} dysregulation as a key phenotype of DMD presented in vitro [22–25, 28–31]. To assess the extent of Ca^{2+} dysregulation in DMD 263delG EHTs, the ratiometric Ca^{2+} dye Fura-2 was used to assess both the kinetics of Ca^{2+} transients as well as the relative cytosolic Ca^{2+} levels under electrical field stimulation at 1.5 Hz. Comparing the ratiometric fluorescence intensities (**Fig 3.8A**) revealed significantly higher baseline levels of cytosolic Ca^{2+} (**Fig 3.8B**) as well as higher peak levels (**Fig 3.8C**) but with a decreased amplitude of Ca^{2+} flux in DMD 263delG EHTs (**Fig 3.8D**). Examining the kinetics of Ca^{2+} transients of control and DMD 263delG EHTs, normalized traces of cytosolic Ca^{2+} flux (**Fig 3.8E**) revealed slower time to Ca^{2+} transient peak in DMD 263delG EHTs (**Fig 3.8F**). We observed a decreased rate to 50% and 90% Ca^{2+} transient decay in DMD 263delG EHTs (**Fig 3.8G-H**). While we observed some batch-to-batch variability in measured 365nm/380nm values, the trends remained consistent. An examination of average force-Ca^{2+} loops highlighted the elevated Ca^{2+} level and decreased Ca^{2+} transient amplitude, as well as the decreased twitch force in DMD 263delG EHTs (**Fig 3.8I**). The significantly decreased force- Ca^{2+} loop area provided further evidence toward the lower Ca^{2+} flux as a significant contributor to the reduction of force seen in DMD 263delG EHTs (**Fig 3.8J**). These results point to elevated cytosolic Ca^{2+} and Ca^{2+} transient abnormalities as key contributors to the dystrophic phenotype presented in vitro.

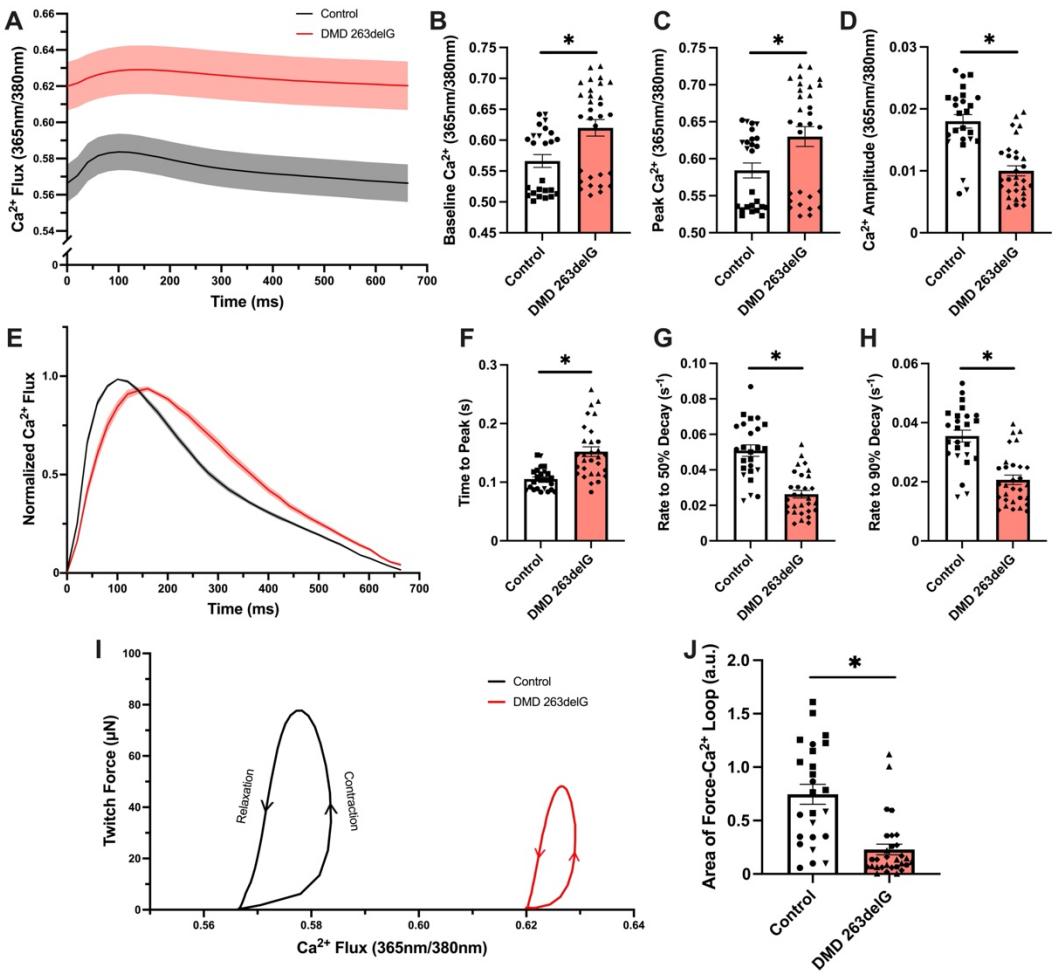

Fig. 3.8. Ca^{2+} transients of DMD 263delG EHTs. (A) Average relative cytosolic Ca^{2+} levels during EHT contraction as measured with Fura-2 AM (365nm/380nm). (B) Measured baseline, (C) peak, and (D) amplitude of relative Ca^{2+} level. (E) Normalized average Ca^{2+} transient traces. (F) Calculated time to peak, (G) rate to 50% Ca^{2+} transient decay, and (H) rate to 90% transient decay. (I) Average force- Ca^{2+} loops of control and DMD 263delG EHTs. Twitch force and Ca^{2+} transients were simultaneously captured using the movement of the flexible post as seen with Fura-2 fluorescence. (J) Calculated area of force-Ca^{2+} loops (Control n = 25, DMD 263delG n = 30). For (A) and (E), lines represent average ± S.E.M. Data shown represent all replicates from three independent experiments per cell line, different symbols represent different experimental batches (Control n = 25, DMD 263delG n = 30).

3.4.6 Increased beat interval irregularity in DMD EHTs

To investigate consequences of Ca^{2+} transient abnormalities, we next investigated whether previously observed increased beat interval irregularity (ΔBI) was conserved in this model [23, 30]. We found that DMD 263delG and control EHTs had similar average spontaneous beating frequencies (**Fig 3.9A**), but upon closer inspection of individual traces, intermittent irregular beats were observed to occur at a higher frequency in DMD 263delG EHTS (**Fig 3.9B**). We compared the difference between subsequent beat intervals ($\Delta BI = BI_{n+1} - BI_n$), which revealed a higher distribution of ΔBI in 263delG EHTs when distributions were compared with a nonparametric statistical test (**Fig 3.9C**). We noted that the distribution of ΔBI in the DMD 263delG EHTs spanned a greater time interval than the control EHTs. To highlight this difference, we selected a cutoff values of 1000 ms and compared the frequency with which ΔBI events exceeded this cutoff. This analysis revealed an increased occurrence of highly irregular events in DMD 263delG EHTs (**Fig 3.9D**). All collected traces are shown in **Fig 3.10**. These results indicate a potential downstream consequence of the altered Ca^{2+} transients observed in DMD 263delG EHTs.

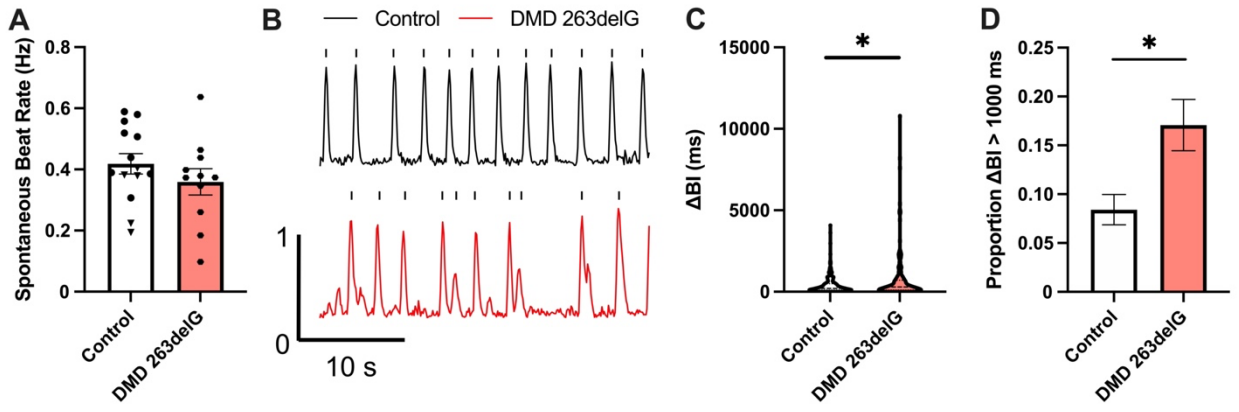

Fig. 3.9. Spontaneous beat interval variability in DMD 263delG EHTs. (A) Spontaneous beat rate of control and DMD 263delG EHTs. (B) Representative traces of spontaneous EHT contraction with counted beats labeled with tick marks. (C) Distribution of calculated beat interval (BI) variability ($\Delta BI = BI_{n+1} - BI_n$) measured over 30 s of spontaneous

EHT contraction and (D) proportion of beats occurring with ΔBI > 1000 ms. Data shown represent all replicates from 1–2 independent experiments, different symbols represent different experimental batches (Control n = 14, DMD 263delG n = 11).

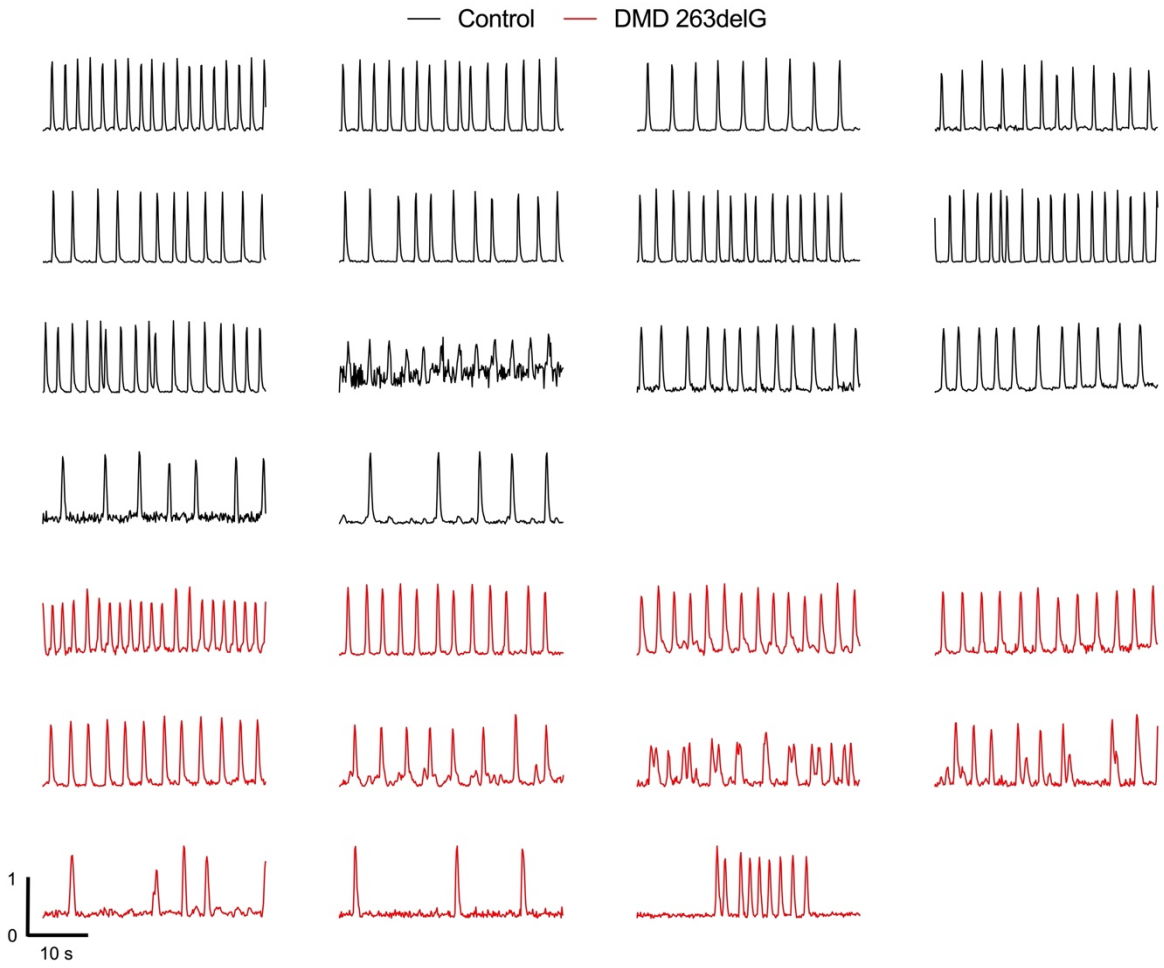

Figure 3.10. Beat interval irregularity traces for control and DMD 263delG EHTs. Normalized traces of EHT displacement measured at the flexible post measured over 60 s of spontaneous EHT contraction. Each trace represents a single EHT.

3.5 Discussion

The mechanisms underlying cardiac disease initiation and progression in the absence of dystrophin are poorly understood, despite the prevalence of cardiomyopathy and heart failure as the leading cause of death for DMD patients. Thus, there is a need for human models of DMD to uncover the molecular drivers of cardiac pathology and to aid in the development of novel therapeutics. This is especially true considering recent unexpected adverse events and failure to meet clinical endpoints in several DMD gene therapy clinical trials currently underway [51]. Human-derived, 2D stem cell models have emerged as a powerful tool to study the disease characteristics of various *DMD* mutations and to test various pharmaceutical, gene editing, and exon skipping treatment approaches [21]. However, it is likely that 3D culture is needed to promote more physiological cell behavior and to better understand how the absence of full-length dystrophin affects tissue-level function. To address this, we developed a 3D tissue-engineered cardiac model of DMD and demonstrated that it recapitulates multiple key aspects of the disease (**Fig 3.11**).

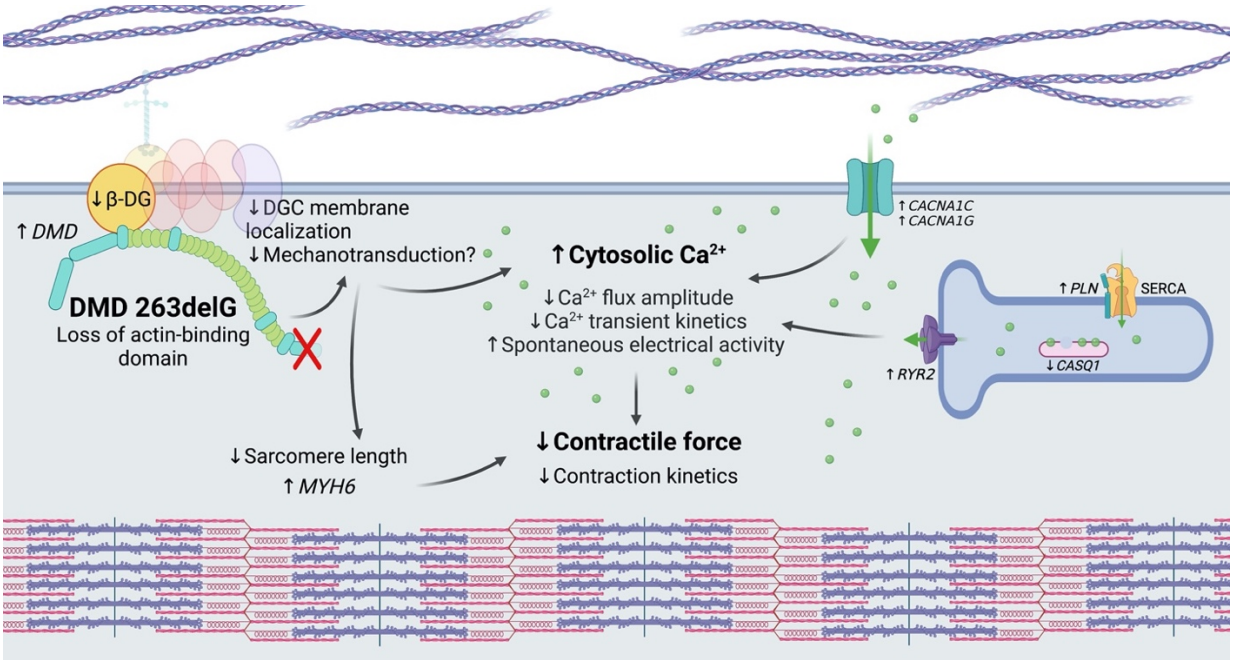

Fig. 3.11. Summary of proposed mechanism of observed phenotypes in DMD 263delG EHTs.

We observed profound differences in transcriptomic changes that occur as a result of the DMD 263delG mutation in EHTs as compared to hiPSC-CMs grown in 2D culture. While both platforms produced clear transcriptomic differences between control and DMD 263delG genotypes, we found that the EHT platform evoked a smaller pool of transcriptional changes much more relevant to cardiac biology, highlighting the improved biological relevance of this 3D model. When comparing control and DMD 263delG EHTs, several biological processes of interest emerged during GO analysis, with which we can begin to hypothesize the molecular drivers of the dystrophic phenotype found in subsequent analysis of this model.

Dystrophin mutations have long been thought to cause myocyte frailty, although it is less understood how this affects cell contractility. In this study, we observed a decrease in auxotonic contractile performance in EHTs lacking full-length dystrophin. This finding is in agreement with previous studies performed on dystrophic hiPSC-CMs cultured as embryoid bodies [30], as well as 3D engineered cardiac tissues under isometric loading [25, 52]. This contractile deficit has also been observed in myofibrils isolated from hiPSC-CMs lacking full-length dystrophin [31], indicating that this phenotype is likely partially explained by changes at the sarcomere level. This notion is supported by our finding that while both control and DMD 263delG EHTs produced uniaxially aligned sarcomeres with similar Z-disk widths and sarcomere alignment, we found that DMD 263delG EHTs had significantly shorter sarcomeres. Regarding the kinetics of EHT contraction, we observed that dystrophic EHTs displayed slower force development as well as relaxation kinetics, in accordance with what has been observed at both the single cell and myofibril level, where isolated myofibrils from hiPSC-CMs lacking full-length dystrophin were found to have a slower fast phase of relaxation [31]. The delayed relaxation kinetics observed in this study replicate the diastolic dysfunction known to be one of the initial clinical phenotypes observed in patients with DMD [53].

The contractile phenotype observed is further supported by our transcriptomic results, in which we observed upregulation of processes related to heart development and cardiomyocyte differentiation in DMD 263delG EHTs, including increased expression of *MYH6*, which has been shown to be a marker of hiPSC-CM immaturity and could also be a contributor to the observed decrease in contractile forces [54, 55]. DMD 263delG EHTs also displayed downregulation of genes related to extracellular matrix deposition and organization (several collagen genes, *MMP2*, *LOX*, *LOXL1*, *LOXL2*), which point to a potential inability of DMD 263delG hiPSC-CMs to exert their internal forces on the external environment, which could contribute to the observed decrease in EHT contractile forces.

Increased cytosolic Ca^{2+} levels and aberrant Ca^{2+} handling are thought to be key contributors to mechanisms of dystrophic pathology in patients. Here, for the first time, we examine the Ca^{2+} transients of dystrophin-mutant hiPSC-CMs in 3D culture, moving us closer toward understanding the role of dystrophin in mediating Ca^{2+} handling at the tissue level. We found that DMD 263delG EHTs had higher resting Ca^{2+} levels with a smaller amplitude of Ca^{2+} flux and delayed Ca^{2+} transient kinetics. Higher cytosolic Ca^{2+} [23, 24, 28] and slowed Ca^{2+} transient kinetics [22, 25, 29–31] have been previously observed in 2D cultured dystrophin-deficient hiPSC-CMs. It is thought that increased cytosolic Ca^{2+} in dystrophic myocardium can arise from multiple sources, including membrane tears [56] and stretch-activated channels [57], and can be worsened by hyper-phosphorylation of Ca^{2+} channels [58] and a leaky sarcoplasmic reticulum due to increased ryanodine receptor open probability [59]. The observed increase in baseline cytosolic Ca^{2+} and decreased amplitude of Ca^{2+} flux in DMD 263delG EHTs are likely contributors to the observed contractile deficiencies and delayed contractile kinetics. As Ca^{2+} overload has been shown to mediate cardiac arrythmias [60, 61], and previous studies have shown dystrophin-deficient hiPSC-CMs to have increased spontaneous beat rate variability [23, 27, 30], we adapted a multi-electrode array method of assessing beat rate variability to assess

arrhythmogenicity in this 3D model of DMD [44]. We observed that spontaneously contracting, dystrophic EHTs had a higher incidence of irregular beats, which we propose may be caused by the observed elevated cytosolic Ca^{2+}. To the best of our knowledge, this is the first time this dystrophic beat interval irregularity phenomenon has been observed in a 3D in vitro model.

The Ca^{2+} transient results are further supported by our transcriptomic data, which showed that DMD 263delG EHTs exhibited downregulation (*CASQ1*) and upregulation (*PLN*, *RYR2*) of genes related to sarcoplasmic reticulum function, which suggest decreased Ca^{2+} storage in the sarcoplasmic reticulum. Additionally, DMD EHTs displayed increased expression of genes related to excitation-contraction coupling and regulation of membrane potential (*SCN5A*, *CACNA1G*, *CACNA1C*) which, could point toward membrane hyper-excitability and increased Na^{+} and Ca^{2+} currents causing prolongation of action potentials and increased incidence of early after depolarizations. Taken together, these results support the potential for electrophysiological remodeling that occurs as a consequence of, or as a compensatory mechanism in the absence of full-length dystrophin and thus help explain the observed elevated cytosolic Ca^{2+} levels, delayed Ca^{2+} transients, and increased beat rate variability.

Of note, it appears that sufficient cellular maturation may be required to expose this Ca^{2+} transient phenotype, as our group has found that dystrophic hiPSC-CMs displayed elevated Ca^{2+} levels, but only when exposed to a combination of maturational cues [23]. Additionally, others have observed that the elevated Ca^{2+} levels were exacerbated when dystrophic hiPSC-CMs were exposed to mechanical stretch [28]. These findings suggest that the EHT platform provides sufficient maturational cues and mechanical loading necessary to expose this Ca^{2+} transient phenotype that is thought to be central to DMD pathology. In this study, our specific DMD truncating mutation allows us to study the effect of protein structure on Ca^{2+} transients. Our model displays Ca^{2+} transient abnormalities despite retaining much of the dystrophin protein except for a portion of the actin-binding domain, illustrating a novel link between the mechanical cues

provided by the full-length protein structure and Ca^{2+} handling. Additionally, this is the first time that a dystrophic Ca^{2+} handling defect has been shown in a 3D in vitro model, which is a significant step in advancing the clinical relevance of stem cell-derived disease models of DMD.

Studies in *mdx* mice have provided insight into mechanisms of DMD pathology, as they recapitulate some clinical aspects of DMD. While used extensively to study skeletal muscle pathology, the utility of this model to study dystrophic cardiomyopathy is greatly limited as this model displays few clinical signs of cardiomyopathy until old age or in the presence of multiple knockouts for dystroglycan complex proteins [17], highlighting the need for humanized models of dystrophic cardiomyopathy. Our study revealed decreased force production with slowed kinetics in dystrophic EHTs. Similarly, a study performed with young *mdx* mice revealed decreased force production by isolated papillary muscles in addition to impaired myosin function as evidenced by in vitro motility [14]. Additionally, cardiomyocytes isolated from *mdx* mice display elevated cytosolic Ca^{2+}, although this phenotype only emerges in older mice (9-12 months) [4, 62, 63], whereas our EHT platform was able to recapitulate this finding in three weeks. It is intriguing to consider that a human model such as the one described herein may help in bridging the gap between animal models and clinical trials in the development of therapeutics to treat DMD.

This study has illustrated the power of a 3D in vitro model to recapitulate a variety of disease-relevant phenotypes in a single simple and highly tunable platform. To our knowledge, this is the first study to provide such an in-depth description of a hiPSC-derived dystrophic phenotype in a 3D, tissue engineered model. In this EHT platform, the readout of force production provides a functional means by which to assess the extent of overall dystrophic cardiac dysfunction, as the observed Ca^{2+} dysregulation and impaired sarcomere structure as well as unexplored potential deficiencies in mitochondrial function and nitric oxide signaling likely contribute to this observed reduction in contractile force. To this end, force production can be viewed as the integration of overall cardiac dysfunction, suitable for preclinical screening

applications. Having established the disease phenotype presented in this study, future studies will be able to use this platform to investigate the mechanisms underlying DMD pathology and test emerging therapies in a physiologically-relevant platform. The contribution of Ca^{2+} overload to the contractile deficiencies in dystrophic EHTs can be investigated through the use of Ca^{2+} channel blockers or membrane sealants, as has been shown in previous in vitro studies [23, 24]. Exon-skipping [26, 64] and gene editing [29, 65–67] have been shown to restore dystrophin expression in 2D hiPSC-CMs and limited studies have shown recovery of force of contraction in 3D engineered cardiac tissues [25, 52], but these studies have fallen short of describing a robust functional recovery in vitro. Through the studies described herein, we have made significant progress toward the development of a human-derived model of dystrophic cardiomyopathy.

3.6 Conclusions

Our ability to efficiently study DMD pathophysiology and develop emerging therapies is limited by the lack of functional in vitro, human disease models. In this study, we generated 3D, human engineered heart tissue as a model of DMD and described the transcriptional changes and multifaceted disease phenotype presented. Stem cell-derived cardiomyocytes lacking full-length dystrophin, when cast into EHTs, were shown to display decreased force production and slowed kinetics, accompanied by decreased sarcomere lengths. For the first time, we examined Ca^{2+} transients in a 3D in vitro model of DMD and found that dystrophic EHTs had elevated baseline cytosolic Ca^{2+} levels with slowed Ca^{2+} release and reuptake. Lastly, we observed increased beat interval irregularity in dystrophic EHTs. Taken together, we present the value of a 3D tissue-engineered model of DMD in that it can replicate a variety of dystrophic phenotypes while providing a platform for assessment of overall cardiac function, something unattainable with most traditional tissue culture methods. Future studies will further uncover the mechanisms underlying the dystrophic phenotypes observed as well as explore the translational potential of this in vitro platform as a preclinical model of dystrophic heart disease.

3.7 References

1. Eagle M, Baudouin S V, Chandler C, et al (2002) Survival in Duchenne muscular dystrophy: improvements in life expectancy since 1967 and the impact of home nocturnal ventilation. Neuromuscul Disord 12:926–9. https://doi.org/10.1016/S0960-8966(02)00140-2

2. Rybakova IN, Patel JR, Ervasti JM (2000) The dystrophin complex forms a mechanically strong link between the sarcolemma and costameric actin. J Cell Biol 150:. https://doi.org/10.1083/JCB.150.5.1209

3. Rapezzi C, Leone O, Biagini E, Coccolo F (2007) Echocardiographic clues to diagnosis of dystrophin related dilated cardiomyopathy. Heart 93:10. https://doi.org/10.1136/hrt.2006.087643

4. Fanchaouy M, Polakova E, Jung C, et al (2009) Pathways of abnormal stress-induced Ca2+ influx into dystrophic mdx cardiomyocytes. Cell Calcium 46:114–121. https://doi.org/10.1016/j.ceca.2009.06.002

5. Rohman MS, Emoto N, Takeshima Y, et al (2003) Decreased mAKAP, ryanodine receptor, and SERCA2a gene expression in mdx hearts. Biochem Biophys Res Commun 310:228–35. https://doi.org/10.1016/J.BBRC.2003.09.005

6. Chang WJ, Iannaccone ST, Lau KS, et al (1996) Neuronal nitric oxide synthase and dystrophin-deficient muscular dystrophy. Proc Natl Acad Sci U S A 93:9142–9147. https://doi.org/10.1073/pnas.93.17.9142

7. Rando TA (2001) Role of nitric oxide in the pathogenesis of muscular dystrophies: A “two hit” hypothesis of the cause of muscle necrosis. Microsc Res Tech 55:223–235. https://doi.org/10.1002/jemt.1172

8. Khairallah M, Khairallah R, Young ME, et al (2007) Metabolic and signaling alterations in

dystrophin-deficient hearts precede overt cardiomyopathy. J Mol Cell Cardiol 43:119–129. https://doi.org/10.1016/j.yjmcc.2007.05.015

9. Percival JM, Siegel MP, Knowels G, Marcinek DJ (2013) Defects in mitochondrial localization and ATP synthesis in the mdx mouse model of Duchenne muscular dystrophy are not alleviated by PDE5 inhibition. Hum Mol Genet 22:153–167. https://doi.org/10.1093/hmg/dds415

10. van Westering T, Betts C, Wood M (2015) Current Understanding of Molecular Pathology and Treatment of Cardiomyopathy in Duchenne Muscular Dystrophy. Molecules 20:8823–8855. https://doi.org/10.3390/molecules20058823

11. Shin J, Tajrishi MM, Ogura Y, Kumar A (2013) Wasting mechanisms in muscular dystrophy. Int J Biochem Cell Biol 45:2266–79. https://doi.org/10.1016/j.biocel.2013.05.001

12. Mora M, Di Blasi C, Barresi R, et al (1996) Developmental expression of dystrophin, dystrophin-associated glycoproteins and other membrane cytoskeletal proteins in human skeletal and heart muscle. Dev Brain Res 91:70–82. https://doi.org/10.1016/0165-3806(95)00169-7

13. Chevron MP, Girard F, Claustres M, Demaille J (1994) Expression and subcellular localization of dystrophin in skeletal, cardiac and smooth muscles during the human development. Neuromuscul Disord 4:419–432. https://doi.org/10.1016/0960-8966(94)90081-7

14. Wagner S, Knipp S, Weber C, et al (2012) The heart in Duchenne muscular dystrophy: early detection of contractile performance alteration. J Cell Mol Med 16:3028. https://doi.org/10.1111/J.1582-4934.2012.01630.X

15. Górecki DC (2016) Dystrophin: The dead calm of a dogma. Rare Dis 4:e1153777. https://doi.org/10.1080/21675511.2016.1153777

16. Bulfield G, Siller WG, Wight PAL, Moore KJ (1984) X chromosome-linked muscular dystrophy (mdx) in the mouse. Proc Natl Acad Sci U S A 81:1189–1192. https://doi.org/10.1073/pnas.81.4.1189

17. McGreevy JW, Hakim CH, McIntosh MA, Duan D (2015) Animal models of Duchenne muscular dystrophy: from basic mechanisms to gene therapy. Dis Model Mech 8:195–213. https://doi.org/10.1242/dmm.018424

18. Pastoret C, Sebille A (1995) mdx mice show progressive weakness and muscle deterioration with age. J Neurol Sci 129:97–105. https://doi.org/10.1016/0022-510X(94)00276-T

19. Chamberlain JS, Metzger J, Reyes M, et al (2007) Dystrophin-deficient mdx mice display a reduced life span and are susceptible to spontaneous rhabdomyosarcoma. FASEB J 21:2195–2204. https://doi.org/10.1096/fj.06-7353com

20. Yu X, Bao B, Echigoya Y, Yokota T (2015) Dystrophin-deficient large animal models: translational research and exon skipping. Am J Transl Res 7:1314–31

21. Pioner JM, Fornaro A, Coppini R, et al (2020) Advances in Stem Cell Modeling of Dystrophin-Associated Disease : Implications for the Wider World of Dilated Cardiomyopathy. Front Physiol 11:368. https://doi.org/10.3389/fphys.2020.00368

22. Guan X, Mack DL, Moreno CM, et al (2014) Dystrophin-deficient cardiomyocytes derived from human urine: New biologic reagents for drug discovery. Stem Cell Res 12:467–480. https://doi.org/10.1016/j.scr.2013.12.004

23. Macadangdang JR, Miklas JW, Smith AST, et al (2018) Engineered developmental niche enables predictive phenotypic screening in human dystrophic cardiomyopathy. bioRxiv 456301. https://doi.org/10.1101/456301

24. Lin B, Li Y, Han LL, et al (2015) Modeling and study of the mechanism of dilated

cardiomyopathy using induced pluripotent stem cells derived from individuals with Duchenne muscular dystrophy. Dis Model Mech 8:457–466. https://doi.org/10.1242/dmm.019505

25. Kyrychenko V, Kyrychenko S, Tiburcy M, et al (2017) Functional correction of dystrophin actin binding domain mutations by genome editing. JCI insight 2:. https://doi.org/10.1172/jci.insight.95918

26. Sato M, Shiba N, Miyazaki D, et al (2019) Amelioration of intracellular Ca2+ regulation by exon-45 skipping in Duchenne muscular dystrophy-induced pluripotent stem cell-derived cardiomyocytes. Biochem Biophys Res Commun 520:179–185. https://doi.org/10.1016/j.bbrc.2019.09.095

27. Eisen B, Ben Jehuda R, Cuttitta AJ, et al (2019) Electrophysiological abnormalities in induced pluripotent stem cell-derived cardiomyocytes generated from Duchenne muscular dystrophy patients. J Cell Mol Med 23:2125–2135. https://doi.org/10.1111/jcmm.14124

28. Tsurumi F, Baba S, Yoshinaga D, et al (2019) The intracellular Ca 2+ concentration is elevated in cardiomyocytes differentiated from hiPSCs derived from a Duchenne muscular dystrophy patient. PLoS One 14:e0213768. https://doi.org/10.1371/journal.pone.0213768

29. Moretti A, Fonteyne L, Giesert F, et al (2020) Somatic gene editing ameliorates skeletal and cardiac muscle failure in pig and human models of Duchenne muscular dystrophy. Nat Med 26:207–214. https://doi.org/10.1038/s41591-019-0738-2

30. Jelinkova S, Vilotic A, Pribyl J, et al (2020) DMD Pluripotent Stem Cell Derived Cardiac Cells Recapitulate in vitro Human Cardiac Pathophysiology. Front Bioeng Biotechnol 8:535. https://doi.org/10.3389/fbioe.2020.00535

31. Pioner JM, Guan X, Klaiman JM, et al (2019) Absence of full-length dystrophin impairs normal maturation and contraction of cardiomyocytes derived from human-induced

pluripotent stem cells. Cardiovasc Res 116:368–382. https://doi.org/10.1093/cvr/cvz109

32. Bielawski KS, Leonard A, Bhandari S, et al (2016) Real-rime force and frequency analysis of engineered human heart tissue derived from induced pluripotent stem cells using magnetic sensing. Tissue Eng Part C 22:932–940. https://doi.org/10.1089/ten.tec.2016.0257

33. Leonard A, Bertero A, Powers JD, et al (2018) Afterload promotes maturation of human induced pluripotent stem cell derived cardiomyocytes in engineered heart tissues. J Mol Cell Cardiol 118:147–158. https://doi.org/10.1016/j.yjmcc.2018.03.016

34. Bremner SB, Goldstein AJ, Higashi T, Sniadecki NJ (2022) Engineered Heart Tissues for Contractile, Structural, and Transcriptional Assessment of Human Pluripotent Stem Cell-Derived Cardiomyocytes in a Three-Dimensional, Auxotonic Environment. In: Coulombe KLK, Black LD (eds) Cardiac Tissue Engineering: Methods and Protocols, 2nd ed. Springer US, New York, NY, United States

35. Mihic A, Li J, Miyagi Y, et al (2014) The effect of cyclic stretch on maturation and 3D tissue formation of human embryonic stem cell-derived cardiomyocytes. Biomaterials 35:2798–2808. https://doi.org/10.1016/j.biomaterials.2013.12.052

36. Ruan J-LL, Tulloch NL, Razumova M V., et al (2016) Mechanical stress conditioning and electrical stimulation promote contractility and force maturation of induced pluripotent stem cell-derived human cardiac tissue. Circulation 134:1557–1567. https://doi.org/10.1161/CIRCULATIONAHA.114.014998

37. Ruan JL, Tulloch NL, Saiget M, et al (2015) Mechanical stress promotes maturation of human myocardium from pluripotent stem cell-derived progenitors. Stem Cells 33:2148–2157. https://doi.org/10.1002/stem.2036

38. Abilez OJ, Tzatzalos E, Yang H, et al (2018) Passive stretch induces structural and

functional maturation of engineered heart muscle as predicted by computational modeling. Stem Cells 36:265–277. https://doi.org/10.1002/stem.2732

39. Shimko VF, Claycomb WC (2008) Effect of mechanical loading on three-dimensional cultures of embryonic stem cell-derived cardiomyocytes. Tissue Eng - Part A 14:49–58. https://doi.org/10.1089/ten.a.2007.0092

40. Macadangdang J, Guan X, Smith AST, et al (2015) Nanopatterned Human iPSC-Based Model of a Dystrophin-Null Cardiomyopathic Phenotype. Cell Mol Bioeng 8:320–332. https://doi.org/10.1007/s12195-015-0413-8

41. Lian X, Zhang J, Azarin SM, et al (2012) Directed cardiomyocyte differentiation from human pluripotent stem cells by modulating Wnt/β-catenin signaling under fully defined conditions. Nat Protoc 8:162–175. https://doi.org/10.1038/nprot.2012.150

42. Sniadecki NJ, Chen CS (2007) Microfabricated Silicone Elastomeric Post Arrays for Measuring Traction Forces of Adherent Cells. Methods Cell Biol 83:313–328. https://doi.org/10.1016/S0091-679X(07)83013-5

43. Rodriguez AG, Han SJ, Regnier M, Sniadecki NJ (2011) Substrate stiffness increases twitch power of neonatal cardiomyocytes in correlation with changes in myofibril structure and intracellular calcium. Biophys J 101:2455–2464. https://doi.org/10.1016/j.bpj.2011.09.057

44. Gilchrist KH, Lewis GF, Gay EA, et al (2015) High-throughput cardiac safety evaluation and multi-parameter arrhythmia profiling of cardiomyocytes using microelectrode arrays. Toxicol Appl Pharmacol 288:249–257. https://doi.org/10.1016/j.taap.2015.07.024

45. Salick MR, Napiwocki BN, Kruepke RA, et al (2020) The scanning gradient Fourier transform (SGFT) method for assessing sarcomere organization and alignment. J Appl Phys 127:194701. https://doi.org/10.1063/1.5129347

46. Liao Y, Smyth GK, Shi W (2019) The R package Rsubread is easier, faster, cheaper and better for alignment and quantification of RNA sequencing reads. Nucleic Acids Res 47:e47–e47. https://doi.org/10.1093/NAR/GKZ114

47. Robinson MD, McCarthy DJ, Smyth GK (2010) edgeR: a Bioconductor package for differential expression analysis of digital gene expression data. Bioinformatics 26:139–140. https://doi.org/10.1093/BIOINFORMATICS/BTP616

48. Wu T, Hu E, Xu S, et al (2021) clusterProfiler 4.0: A universal enrichment tool for interpreting omics data. Innov 2:100141. https://doi.org/10.1016/J.XINN.2021.100141

49. Banks GB, Gregorevic P, Allen JM, et al (2007) Functional capacity of dystrophins carrying deletions in the N-terminal actin-binding domain. Hum Mol Genet 16:2105–2113. https://doi.org/10.1093/HMG/DDM158

50. Gilbert G, Kadur Nagaraju C, Duelen R, et al (2021) Incomplete Assembly of the Dystrophin-Associated Protein Complex in 2D and 3D-Cultured Human Induced Pluripotent Stem Cell-Derived Cardiomyocytes. Front Cell Dev Biol 9:1–9. https://doi.org/10.3389/fcell.2021.737840

51. Elangkovan N, Dickson G (2021) Gene Therapy for Duchenne Muscular Dystrophy. J Neuromuscul Dis 8:S303–S316. https://doi.org/10.3233/JND-210678

52. Long C, Li H, Tiburcy M, et al (2018) Correction of diverse muscular dystrophy mutations in human engineered heart muscle by single-site genome editing. Sci Adv 4:eaap9004. https://doi.org/10.1126/sciadv.aap9004

53. McNally EM, Kaltman JR, Woodrow Benson D, et al (2015) Contemporary cardiac issues in Duchenne muscular dystrophy. Circulation 131:1590–1598. https://doi.org/10.1161/CIRCULATIONAHA.114.015151

54. Grancharova T, Gerbin KA, Rosenberg AB, et al (2021) A comprehensive analysis of gene

expression changes in a high replicate and open-source dataset of differentiating hiPSC-derived cardiomyocytes. Sci Reports 2021 111 11:1–21. https://doi.org/10.1038/s41598-021-94732-1

55. Aksel T, ChoeYu E, Sutton S, et al (2015) Ensemble Force Changes that Result from Human Cardiac Myosin Mutations and a Small-Molecule Effector. Cell Rep 11:910. https://doi.org/10.1016/J.CELREP.2015.04.006

56. Petrof BJ, Shrager JB, Stedman HH, et al (1993) Dystrophin protects the sarcolemma from stresses developed during muscle contraction. Proc Natl Acad Sci U S A 90:3710–4

57. Yeung EW, Whitehead NP, Suchyna TM, et al (2005) Effects of stretch-activated channel blockers on [Ca2+]i and muscle damage in the mdx mouse. J Physiol 562:367–380. https://doi.org/10.1113/jphysiol.2004.075275

58. Wehrens XHT, Lehnart SE, Reiken SR, Marks AR (2004) Ca2+/Calmodulin-Dependent Protein Kinase II Phosphorylation Regulates the Cardiac Ryanodine Receptor. Circ Res 94:e61–e70. https://doi.org/10.1161/01.RES.0000125626.33738.E2

59. Fauconnier J, Thireau J, Reiken S, et al (2010) Leaky RyR2 trigger ventricular arrhythmias in Duchenne muscular dystrophy. Proc Natl Acad Sci U S A 107:1559–1564. https://doi.org/10.1073/pnas.0908540107

60. Thandroyen FT, Morris AC, Hagler HK, et al (1991) Intracellular calcium transients and arrhythmia in isolated heart cells. Circ Res 69:810–819. https://doi.org/10.1161/01.RES.69.3.810

61. Schober T, Huke S, Venkataraman R, et al (2012) Myofilament Ca sensitization increases cytosolic Ca binding affinity, alters intracellular Ca homeostasis, and causes pause-dependent Ca-triggered arrhythmia. Circ Res 111:170–179. https://doi.org/10.1161/CIRCRESAHA.112.270041

62. Yasuda S, Townsend D, Michele DE, et al (2005) Dystrophic heart failure blocked by membrane sealant poloxamer. Nature 436:1025–1029. https://doi.org/10.1038/nature03844

63. Williams IA, Allen DG (2007) Intracellular calcium handling in ventricular myocytes from *mdx* mice. Am J Physiol Circ Physiol 292:H846–H855. https://doi.org/10.1152/ajpheart.00688.2006

64. Dick E, Kalra S, Anderson D, et al (2013) Exon skipping and gene transfer restore dystrophin expression in human induced pluripotent stem cells-cardiomyocytes harboring dmd mutations. Stem Cells Dev 22:2714–2724. https://doi.org/10.1089/scd.2013.0135

65. Zhang Y, Long C, Li H, et al (2017) CRISPR-Cpf1 correction of muscular dystrophy mutations in human cardiomyocytes and mice. Sci Adv 3:e1602814. https://doi.org/10.1126/sciadv.1602814

66. Min YL, Li H, Rodriguez-Caycedo C, et al (2019) CRISPR-Cas9 corrects Duchenne muscular dystrophy exon 44 deletion mutations in mice and human cells. Sci Adv 5:eaav4324. https://doi.org/10.1126/sciadv.aav4324

67. Young CS, Hicks MR, Ermolova N V., et al (2016) A Single CRISPR-Cas9 Deletion Strategy that Targets the Majority of DMD Patients Restores Dystrophin Function in hiPSC-Derived Muscle Cells. Cell Stem Cell 18:533–540. https://doi.org/10.1016/j.stem.2016.01.021

Chapter 4. Human engineered heart tissues as a preclinical testing platform for AAV-microdystrophin gene therapies

4.1 Abstract

Miniaturized microdystrophin (μDys) gene therapies delivered by adeno-associated virus (AAV) have emerged as promising treatments for Duchenne muscular dystrophy (DMD). However, preclinical studies have focused largely on skeletal muscle rescue, despite the significant prevalence of cardiomyopathy as the leading cause of death in DMD. This is due to the lack of a severe cardiac phenotype presented in commonly used in vivo models as well as the slower progressing nature of cardiac decline in human patients. To address this, improved in vitro models of dystrophic cardiomyopathy are needed. Previously, we have developed engineered heart tissues (EHTs) from dystrophic human induced pluripotent stem cell-derived cardiomyocytes (hiPSC-CMs), and have demonstrated that dystrophic EHTs reproduce key phenotypes of DMD in vitro. Here, we have further developed a miniaturized EHT (mEHT) platform amenable to higher-throughput screening for preclinical testing of μDys gene therapies. Using this platform, we have demonstrated that DMD mEHTs display a hypocontractile phenotype and that mEHTs are amenable to efficient AAV transduction. Through these experiments, we have demonstrated the relevance of EHTs as a preclinical model of DMD and future studies will evaluate the effect of various μDys gene therapies.

4.2 Introduction

Duchenne muscular dystrophy (DMD) is currently an incurable degenerative neuromuscular disease and available treatments are palliative only, focusing on slowing disease progression and managing symptoms rather than addressing underlying disease pathology. Significant efforts

have been devoted to the development of adeno-associated viral vector (AAV) delivery of truncated microdystrophins (μDys), which promise a one-size-fits all approach to treating DMD by restoring functional dystrophin expression [1]. While the beneficial effects of AAV-μDys gene therapy on skeletal muscle function has been demonstrated extensively, much less is known about the effects of μDys on cardiac function. As cardiomyopathy contributes significantly to patient morbidity and mortality, further studies are warranted.

Three AAV-μDys vectors are currently under clinical trial, and while some positive results have been reported, there have also been unexpected adverse events and failure to meet clinical endpoints [2]. There are concerns regarding vector design, as there are seemingly endless possible combinations of μDys genes, promoters, and AAV capsids. Notably, AAV capsid library screening resulted in the identification of AAVMYO, a synthetic AAV9 variant with greatly improved muscle tropism and expression levels [3]. Additionally, screening of eight μDys designs identified μDys5, a variant including a syntrophin-binding domain that localizes neuronal nitric oxide synthase to the dystroglycan complex, resulting in increased functionality over previous iterations that is currently being evaluated in one clinical trial [4]. Studies currently underway have developed a further panel of μDys variants that are predicted to further improve cardiac functionality. Given all of these potential variations, there is a need for preclinical models of DMD for improved screening of novel therapeutics.

The preclinical models used to study DMD are hampering the progress of novel treatment development. The commonly used *mdx* mouse displays only mild symptoms of DMD, and this lack of severe phenotype is particularly true for presentation of cardiomyopathy [5, 6]. Many studies have shown that AAV-μDys is capable of robust, systemic muscle delivery and expression in addition to correction of dystrophic skeletal muscle phenotypes in *mdx* mice [4, 7–11]. However, when cardiac function has been assessed, μDys was shown to only partially improve cardiac hemodynamics and electrocardiogram profiles [10, 12, 13]. Even when larger, more relevant

canine or rat models are used, these experiments lack human physiology and can take up to 12-months before relevant timepoints in disease progression are met [14, 15]. Thus, there is a need to develop fully-human, in vitro cardiac models of DMD capable of producing relevant output measures of cardiac function.

Human induced pluripotent stem cell derived cardiomyocytes (hiPSC-CMs) have been shown to reproduce many phenotypes of DMD in vitro [16]. Previously, we presented how a 3D engineered heart tissue (EHT) model of DMD replicates many of these key disease phenotypes, while providing a more biomimetic microenvironment and facilitating functional measures of cardiac function [17]. Here, we describe the development of a 96-well miniaturized EHT (mEHT) platform capable of higher throughput screening. We have demonstrated that mEHTs made from dystrophin-deficient hiPSC-CMs display a decrease in contractile function. Additionally, we have shown that hiPSC-CMs and mEHTs are amenable to efficient AAV transduction and transgene expression. Future studies will use the mEHT platform to evaluate the effect of μDys on DMD mEHT function while evaluating the efficiency of AAV capsid and μDys vector variants. The studies described will be the first to assess μDys function in an engineered DMD hiPSC-CM platform, and among the first studies in evaluating several novel μDys vectors not previously described.

4.3 Methods

4.3.1 Vector cloning and virus production

The vectors used in this study were AAV6-cba-dsRed and AAV6-CK8e-μDys5. All AAVs were generated using standard cloning techniques as previously described [4]. To generate AAVs, μDys5 or dsRed cDNA were inserted into pAAV plasmid containing the muscle-specific creatine kinase 8 (CK8) regulatory cassette or cba expression cassette, respectively, and small synthetic polyA flanked by two AAV serotype 2 inverted terminal repeats (ITRs) [4]. Using a

calcium phosphate solution, the final pAAV plasmids were co-transfected with the pDG6 packaging plasmids (containing the AAV Rep and Cap genes) into HEK293 cells to generate recombinant AAV2/6 vectors [3]. AAV6 capsids were purified *via* heparin-affinity chromatography. All AAV preps were concentrated using sucrose gradient centrifugation. Finally, the viral titers were determined by Southern analyses and qPCR.

4.3.2 Maintenance of hiPSC lines and cardiac differentiation

A urine-derived hiPSC line from a healthy male donor (control) was established as previously described [18]. An isogenic dystrophin-null hiPSC line was generated from control hiPSCs using CRISPR-Cas9 as previously described, resulting in the deletion of exon 45 and a 17 base pair deletion in exon 54 as confirmed by DNA sequencing [19]. Undifferentiated hiPSCs were maintained in mTeSR-Plus (Stemcell Technologies) on tissue culture plates coated with Matrigel (Corning).

Cardiomyocyte directed differentiation was performed using a small-molecule protocol to modulate Wnt signaling. Briefly, hiPSCs were dissociated using Versene and seeded at 1.5 – 2.5 $\times$ 10^5 cells/cm^2 on Matrigel-coated plates in mTeSR-Plus with 10 μM Y-27632 ROCK inhibitor (Tocris). The following day, media was changed to mTeSR-Plus supplemented with 1 μM Chiron 99021 (Axon Medchem). Differentiation was initiated 24 h later (day 0), by changing media to RPMI 1640 (Gibco) plus B-27 supplement minus insulin (Life Technologies) and 10 μM Chiron 99021 (Axon Medchem). On day 2 of differentiation, media was changed to RPMI with B-27 minus insulin and 7.5 μM IWP-2 (Selleck Chemicals). On day 4, media was changed to RPMI with B-27 minus insulin. On day 6, media was changed to RPMI with B-27 supplement (with insulin) and media was subsequently changed every 2 days. On day 10, hiPSC-CMs were replated into 6-well dishes for lactate enrichment. On days 12 and 14, media was changed to DMEM without glucose (Gibco) supplemented with 4 mM sodium L-lactate (Sigma-Aldrich) to enrich for cardiomyocytes.

Cells were returned to RPMI with B-27 supplement plus insulin on day 16 and cultured until day 25-27.

4.3.3 Miniaturized EHT platform

We developed a miniaturized EHT (mEHT) platform similarly to our previously described 24-well EHT system [17, 20], made to fit in one row of a standard 96-well cell culture dish. Four-part acrylic molds were manufactured by the University of Washington Department of Mechanical Engineering machine shop, designed to generate 12 pairs of square posts measuring 0.9 mm width (*w*) and 10.5 mm in length (*L*), spaced 3.8 mm apart. Posts were fabricated by pouring uncured polydimethylsiloxane (PDMS, Sylgard 184 mixed at a 10:1 ratio of base to curing agent) into the acrylic molds with a small glass capillary tube inserted into one post of each pair to make it rigid. Posts were left to cure at room temperature for 24 h then baked at 65 °C overnight to cure completely before being separated from the mold. Prior to EHT casting, PDMS posts were submerged in 70% ethanol for 10 min, rinsed with sterile deionized water for 10 min, then UV sterilized for 10 min. The bending stiffness (*K*) of the flexible post in each pair was calculated to be 0.354 μN/μm using a modulus of elasticity (*E*) of PDMS of 2.5 MPa with the equation below, as previously described [21, 22].

$$K = \frac{E \times w^4}{4L^3}$$

mEHTs were cast on day 20-25 of cardiac differentiation using a similar protocol as previously described [23]. Briefly, rectangular 2% agarose casting molds were prepared in 96-well tissue culture plates using 3D-printed spacers. Each rack of PDMS posts was positioned upside down with the tips of posts centered in the agarose wells. A solution of 20 μL volume consisting of 1.5×10^5 hiPSC-CMs and 1.5×10^4 HS27a human bone marrow stromal cells (ATCC) in RPMI with B-27 with 5 mg/mL bovine fibrinogen (Sigma-Aldrich) and 3 U/mL thrombin (Sigma-Aldrich) was pipetted into each agarose well. The mixture was incubated at 37 °C for 60

min to form mEHTs suspended between pairs of posts and then transferred into a new 96-well plate with EHT media (RPMI with B-27 supplemented with 5 mg/mL aminocaproic acid, Sigma-Aldrich) for culture. After 48 hours, mEHTs were switched to a high-Ca^{2+} media consisting of a base mix of 25% RPMI and 75% DMEM with glucose, supplemented with 2% B27 supplement and 5 mg/mL aminocaproic acid (HC-EHT media). HC-EHT media was exchanged every 2-3 days.

4.3.4 hiPSC-CM and mEHT transduction

For AAV transduction of cells in 2D, lactate-enriched hiPSC-CMs were harvested at least 30 days after differentiation. Cells were mixed with the appropriate volume of AAV6-cba-dsRed or AAV6-CK8e-μDys5 (multiplicity of infection, MOI = $1 \times 10^4 - 1 \times 10^6$) in RPMI with B-27 supplemented with 10 μM Y-27632 ROCK inhibitor. Cells and virus were replated at 5×10^4 cells per well in 50 μL for 96-well plates or 3×10^5 cells per well in 250 μL for 24-well plates. 24 h after seeding, an equal volume of RPMI with B-27 supplement was added to each well. Media was exchanged 48 h later, resulting in a 72-h total incubation period with virus.

For AAV transduction of mEHTs, AAV6-cba-dsRed or AAV6-CK8e-μDys5 was added after mEHTs had begun to visibly contract (≥ 7 days after casting). The appropriate volume of AAV6-cba-dsRed (MOI = $1 \times 10^4 - 1 \times 10^6$) was suspended in 100 μL of EHT media per well. mEHTs were incubated with virus for 24 h, after which another 100 μL of EHT media was added per well. Media was exchanged 48 h later, resulting in a 72 h total incubation period with virus.

4.3.5 Contractile force measurement

mEHTs were imaged either in EHT media or Tyrode's buffer (1.8 mM $CaCl_2$, 1 mM $MgCl_2$, 5.4 mM KCl, 140 mM NaCl, 0.33 mM NaH_2PO_4, 5 mM glucose, pH 7.35), as indicated, at 37 °C for contractile analysis. A custom pacing apparatus with carbon electrodes built to fit a 96-well plate was used with an electrical stimulator (Astro Med Grass Stimulator, Model S88X) to provide

biphasic field stimulation at 1 Hz (5 V/cm for 10 ms duration) during imaging. Videos of EHT contraction were taken at 66.7 frames per second using an ORCA-Flash4.0 C13440 CMOS camera (Hamamatsu) on a Nikon TEi epi-fluorescent microscope with a 2× objective and 0.7× coupler, providing 4.64 μm/pixel resolution and a field of view of 9.5 mm × 9.5 mm, which was sufficient to visualize the full length of the mEHTs. A custom MATLAB script was used to track the deflection of the flexible post relative to the rigid post and from this analysis, we calculated twitch force, shortening velocity, time to peak, time to 50% and 90% relaxation, active twitch power, and total twitch work, as previously described [22, 24]. EHT cross-sectional area and specific force were calculated assuming an elliptical cross section with a measured tissue width and conservatively estimated thickness of 100 μm. For each mEHT, analysis was performed on five consecutive contractions.

4.3.6 Immunocytochemistry and fluorescence imaging

To assess AAV6-cba-dsRed expression in situ, hiPSC-CMs and mEHTs were imaged on a Nikon TEi epi-fluorescent microscope at 37 ºC with a TRITC filter cube. Average pixel intensity was calculated in FIJI as the integrated density divided by the area of the region of interest (ROI). For hiPSC-CMs in 96-well plates, the ROI was the entire area of the well and for mEHTs the ROI was the tissue area between the posts. mEHTs were processed for histology as previously described [20]. Briefly, mEHTs were submerged in 140 mM KCl for 1 min to induce EHT relaxation. For analysis of μDys expression, mEHTs were then directly embedded in O.C.T. compound and frozen with liquid nitrogen-cooled isopentane. For analysis of dsRed expression, mEHTs were fixed in 4% paraformaldehyde in PBS for 20 min and dehydrated in 30% w/v sucrose overnight at 4 ºC prior to embedding in O.C.T. compound and freezing. Transverse cryosections of 20 μm thickness were used for histology. Sections were blocked and permeabilized with 1% BSA and 0.1% Triton X-100 for 30 min at room temperature, followed by overnight incubation at 4 °C with mouse primary antibodies against α-actinin (Sigma-Aldrich A7811, 1:800) or dystrophin

(Leica NCL-DYS1, 1:30). The following day, sections were incubated with donkey anti-mouse Alexa Fluor 488, Alexa Fluor 594 phalloidin (Invitrogen, 1:300), and Hoechst 33342 (1:2000) for 1 hour at room temperature. Cover slides were mounted with Fluoromount-G (SouthernBiotech). Images were taken on a Nikon TEi epi-fluorescent microscope or Leica SP8 confocal microscope. Average pixel intensity was calculated using FIJI by measuring the integrated density per pixel area in regions of interest.

4.3.7 Immunoblotting

Protein lysates were obtained from hiPSC-CMs using an ice-cold RIPA buffer supplemented with 2% protease inhibitor cocktail (Sigma P8340). Samples were lysed on ice for 30 min, then spun down at 21,000 *g* for 10 min at 4 ºC. The supernatant was isolated and protein concentration was measured using the Pierce BCA Protein Assay Kit (Thermo Fisher Scientific) according to manufacturer's instructions. Protein samples were stored at -80 ºC.

Samples were prepared for electrophoresis by adding 4× Laemmli Sample Buffer (Bio-Rad) and 2.5% β-mercaptoethanol, after which samples were denatured at 95 ºC for 10 min. Protein was loaded into 4–15% Mini-PROTEAN TGX Stain-Free Gel at 30 µg per sample and run at 100 V for 60 min in 1× Tris/Glycine/SDS running buffer (Bio-Rad). Protein gels were transferred onto Immun-Blot LF PVDF membranes (Bio-Rad) overnight at 30 V and 4 ºC in 1× Tris/Glycine buffer (Bio-Rad) with 10% methanol. Membranes were blocked in Blocker FL Fluorescent Blocking Buffer (Thermo Fisher Scientific) for 1 hour at room temperature. Primary antibodies against dystrophin (DSHB MANEX1011B(1C7) concentrate 1:200), β-actin (sigma A5441, 1:5000), and GAPDH (Sigma SAB4300645, 1:1000) were diluted in blocking buffer and incubation was performed overnight at 4 ºC with agitation. Membranes were washed three times for 5 min in TBS-T at room temperature, then incubated for 1 hour at room temperature with species-matched AlexaFluor-conjugated secondary antibodies (Invitrogen, 1:1000) diluted in blocking buffer with

agitation. Membranes were again washed three times for 5 min in TBS-T before imaging on a ChemiDoc MP imaging system (Bio-Rad).

4.3.8 Replicates and statistical analysis

All values are reported as mean ± standard error of the mean unless indicated otherwise. Results were compared using an unpaired, two-tailed t-test unless indicated otherwise and differences with a p-value < 0.05 were considered statistically significant as indicated with asterisks.

4.4 Results

4.4.1 Development and optimization of a miniaturized EHT (mEHT) platform

While we have shown that EHTs recapitulate many dystrophic phenotypes after only three weeks in culture, the 24-well platform used requires 0.5–1 million hiPSC-CMs per EHT, which is relatively resource intensive for screening experiments [17]. Thus, we have developed a 96-well mEHT platform suitable for higher-throughput experiments (**Fig 4.1A**). Similarly to our larger EHT platform, mEHT twitch force can be measured from the displacement of the flexible post and Ca^{2+} transients can be measured using fluorescent Ca^{2+} indicator dyes (**Fig 4.1B-C**). These mEHTs require only one-fifth of the cells and as little as one-tenth of the culture volume as compared to the 24-well EHT platform (**Fig 4.1.D-E**). While the mEHTs produce lower twitch forces, preliminary studies indicate that the average twitch force per hiPSC-CM in the two platforms is similar (~0.2 nN per hiPSC-CM).

The smaller size and reagent requirements of the mEHT platform lends itself to optimization as well as screening assays. We first optimized the cellular content of an mEHT. The optimal EHT contains enough cells to generate strong contractions, but not too many such that the EHT rips from the posts before desired timepoints are made. The ratio of stromal cells to cardiomyocytes can also play a role in this balance. We designed an experiment based on

response surface methodology to test stromal cell amounts in the range of 1–2 x 10^4 cells/mEHT and hiPSC-CMs in the range of 1–2 x 10^5 cells/mEHT. We then generated mEHTs from control hiPSC-CMs and cultured them for three weeks. We found that generally, more cells produced higher twitch forces, as expected (**Fig 4.1F**). However, when comparing mEHT survival, we found that the mEHTs with the higher cell numbers were more likely to break before the three-week timepoint (**Fig 4.1G**). Ultimately, we chose 1.5 x 10^4 stromal cells and 1.5 x 10^5 hiPSC-CMs as the optimal seeding density per mEHT that produces high twitch forces while retaining mEHT integrity over the culture period.

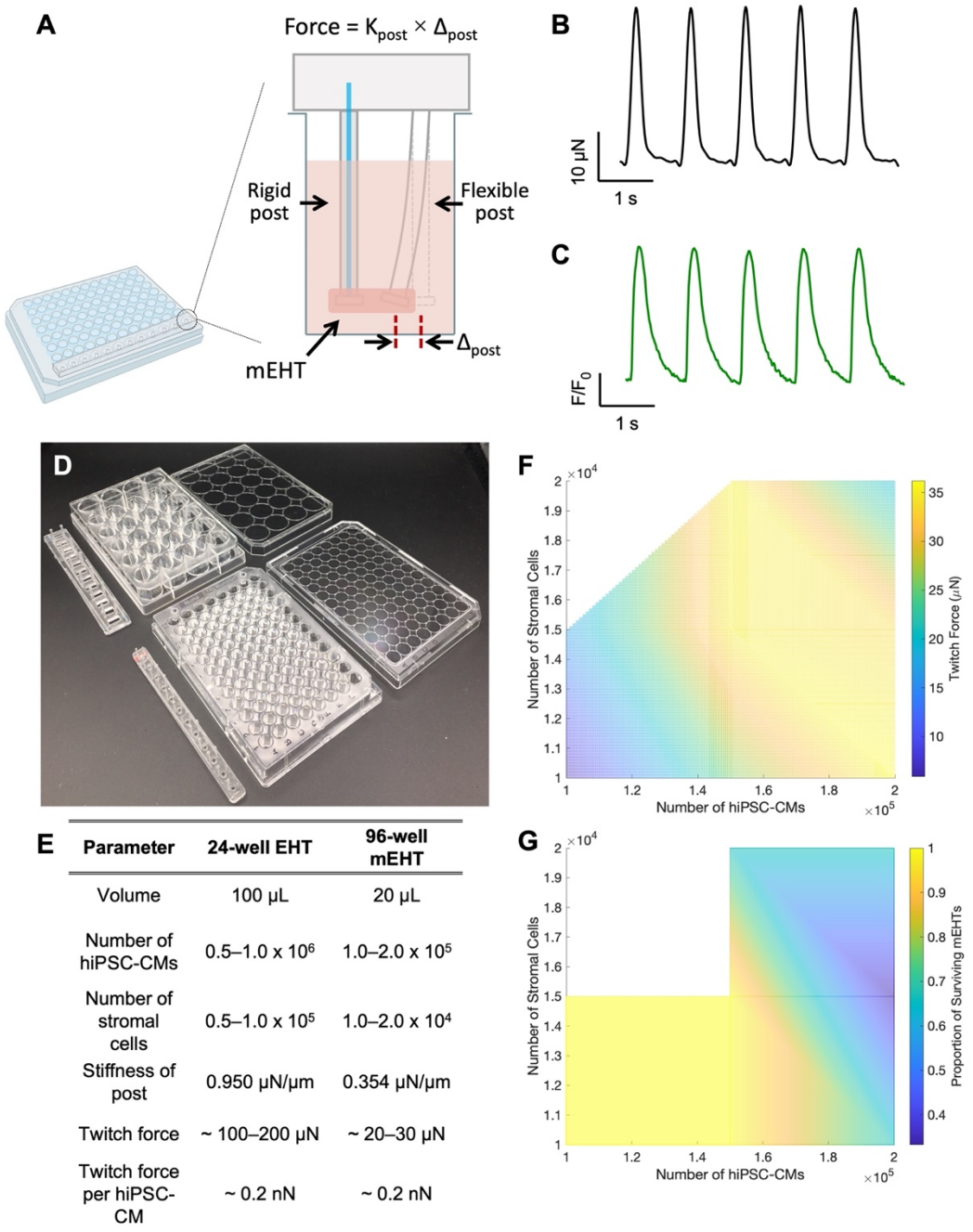

Parameter	24-well EHT	96-well mEHT
Volume	100 μL	20 μL
Number of hiPSC-CMs	0.5–1.0 x 10^6	1.0–2.0 x 10^5
Number of stromal cells	0.5–1.0 x 10^5	1.0–2.0 x 10^4
Stiffness of post	0.950 μN/μm	0.354 μN/μm
Twitch force	~ 100–200 μN	~ 20–30 μN
Twitch force per hiPSC-CM	~ 0.2 nN	~ 0.2 nN

Figure 4.1. Development of a miniaturized EHT platform. (A) Schematic of an mEHT that fits in a standard 96-well culture dish. (B) Representative mEHT twitch force trace. (C) Representative mEHT Ca^{2+} transient acquired using Fluo-4 AM. (D) Side-by-side comparison of 24-well EHT and 96-well mEHT platforms and (E) required reagents, post stiffness, and measured outputs. (F) Twitch forces produced by mEHTs with varying numbers of hiPSC-CMs and stromal cells per mEHT. (G) Proportion of mEHTs surviving after 3 weeks in culture as a function of cell density.

4.4.2 Characterization of dystrophin-null hiPSC-CMs and mEHTs

We previously generated a dystrophin-null hiPSC line (DMD) [19]. This line was generated from the control hiPSC line by a CRISPR-Cas9-targeted deletion of exon 45 and 17 bp deletion from exon 54. Exon 45 deletion is the most common deletion affecting patients and produces an out-of-frame mutation and premature stop codon [25]. The 17 bp deletion in exon 54 also produces a premature stop codon. We detected no dystrophin protein in DMD hiPSC-CMs by western blot; however, both control and DMD hiPSC-CMs express β-dystroglycan, another key member of the dystroglycan protein complex (**Fig 4.2A**). We generated mEHTs from control and DMD hiPSC-CMs, both of which formed compacted tissues that contracted synchronously (**Fig 4.2B**). We further confirmed the lack of dystrophin expression in DMD mEHTs by immunofluorescence staining of mEHT cross-sections (**Fig 4.2C**).

Functional analysis of control and DMD mEHTs after three weeks in culture revealed a similar hypocontractile phenotype as observed previously with our larger EHT platform (**Fig 4.2D**) [17]. When paced at 1 Hz, DMD mEHTs produced significantly lower twitch force and specific force as compared to isogenic controls. This resulted in significantly lower active twitch power and total twitch work in DMD mEHTs. Regarding contractile kinetics, DMD mEHTs had similar time to peak as control mEHTs, but had a lower maximum contractile velocity. mEHT relaxation was impaired as well, with DMD mEHTs trending toward a delayed time to 50% relaxation and a significantly slower time to 90% relaxation. Thus, this mEHT platform is capable of generating a hypocontractile dystrophic phenotype as previously described [17].

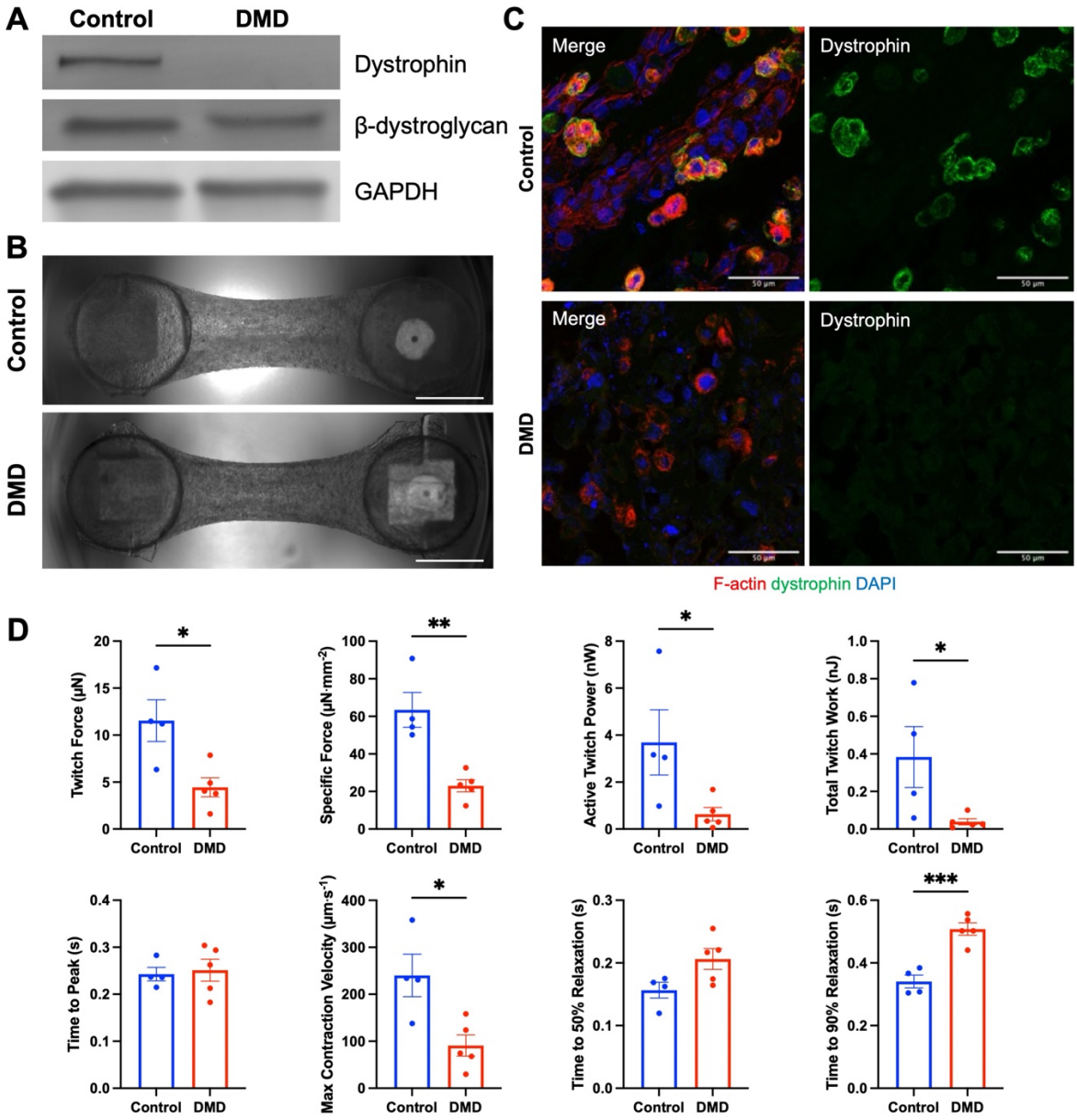

Figure 4.2. Dystrophin-null mEHTs display a hypocontractile phenotype. (A) Western blot for dystrophin, β-dystroglycan, and GAPDH expression in control and DMD hiPSC-CMs. (B) Representative images of compacted control and DMD mEHTs (scale bar = 1 mm). (C) Immunofluorescence images of cross sections of control and DMD mEHTs stained for F-actin (red), dystrophin (green), and nuclei (blue) (scale bar = 50 μm). (D) Measured metrics of control and DMD mEHT contractility derived from videos of mEHT contraction while paced at 1 Hz. Each data point represents an individual EHT. * Indicates P ≤ 0.05, ** indicates P ≤ 0.01, *** indicates P ≤ 0.001.

4.4.3 Efficient AAV transduction of hiPSC-CMs

AAV vectors have proven to be the in vivo delivery method of choice for μDys gene therapies, and previous studies have demonstrated efficient transduction of hiPSC-CMs with AAVs [26, 27]. It has also been demonstrated that EHTs can be transduced with AAV when AAV is added into the EHT reconstitution mixture prior to casting [28]. However, a thorough analysis of EHT transduction efficiency is lacking and in situ AAV transduction of intact, contracting EHTs has not been demonstrated.

We first assessed efficiency of transduction in control hiPSC-CMs in 2D culture using an AAV6 encoding a fluorescent dsRed protein under the constitutively active cytomegalovirus/chicken β-actin (CBA) hybrid promoter (AAV6-cba-dsRed). Control hiPSC-CMs were transduced with AAV-cba-dsRed during replating at three doses (MOI = 1×10^4, 1×10^5, and 1×10^6). We observed efficient transduction of hiPSC-CMs and dose-depended expression of dsRed (**Fig 4.3A-B**). AAV expression was detected as early as three days after transduction and remained for several weeks.

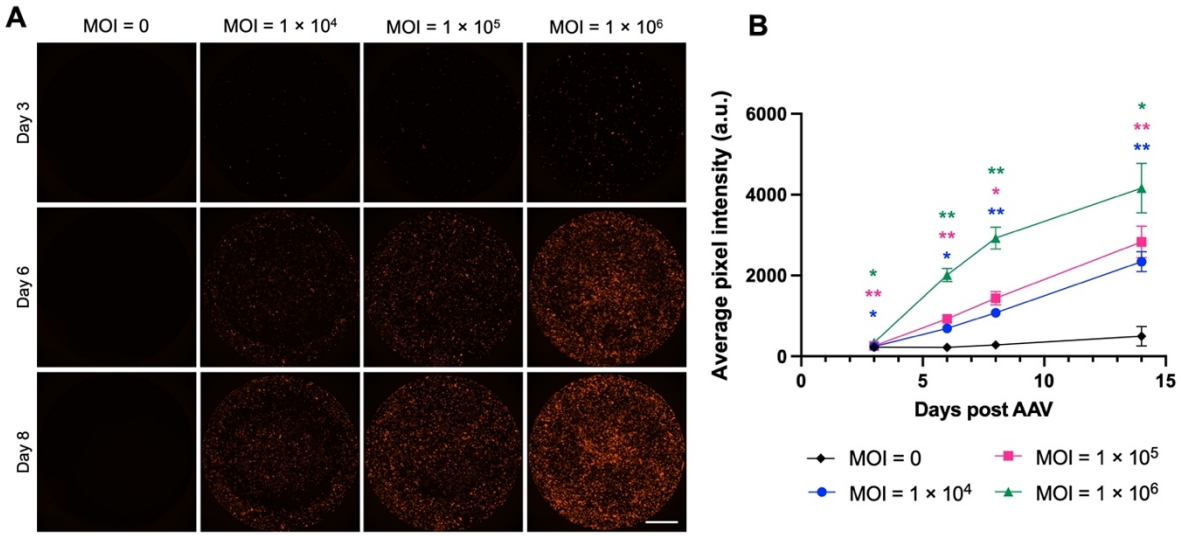

Figure 4.3. Expression of AAV-dsRed in hiPSC-CMs. (A) Representative fluorescent images of hiPSC-CMs transduced with AAV6-cba-dsRed shown 3-, 6-, and 8-days post transduction. (B) Quantification of average pixel

intensity of hiPSC-CM images as a measure of dsRed expression. Asterisks indicate statistically significant differences as compared to MOI = 0 control (n = 3, analyzed by paired two-way ANOVA and Tukey's HSD test). Scale bar = 1 mm.

4.4.4 In situ transduction of mEHTs

Next, we explored whether efficient transduction of mEHTs was feasible, as this transduction paradigm more closely recapitulates the clinical administration of AAV gene therapies. We first attempted to add AAV-cba-dsRed into the mEHT reconstitution mixture during casting as demonstrated in other studies, but while these mEHTs demonstrated robust dsRed expression, these mEHTs remained non-contractile throughout the culture period (not shown). We hypothesize that this might be due to cytotoxicity of the AAV capsid. We subsequently attempted to transduce intact mEHTs 13 days after casting that had already started to contract (MOI = 1×10^4, 1×10^5, 1×10^6). We observed robust and dose-dependent dsRed expression following transduction (**Fig 4.4A-B**). AAV-cba-dsRed was well tolerated by the cells as transduction did not have an effect on mEHT contraction force during the 3 days following transduction (**Fig 4.4C**). Transverse sections of transduced mEHTs demonstrated that AAV-cba-dsRed was able to reach the entire volume of the mEHT, and here again we observed a dose-dependent increase in transduction efficiency (**Fig 4.4D-E**). Ultimately, this in situ transduction scheme is of greater clinical relevance, as in vivo transductions are performed on fully-formed, contractile muscle tissue that has already developed a disease phenotype.

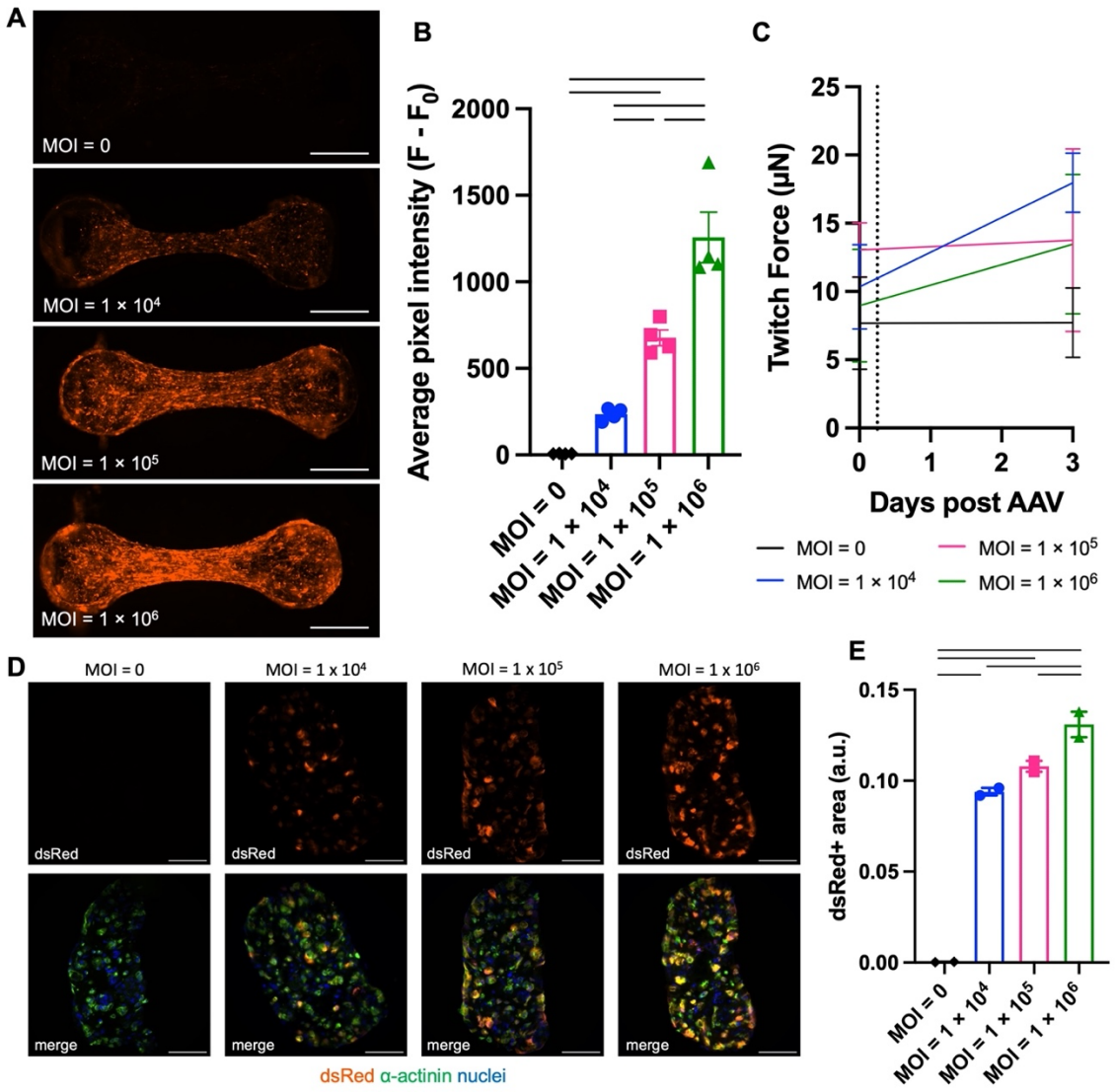

Figure 4.4. In situ AAV transduction of mEHTs. (A) Representative fluorescent images of mEHTs transduced with AAV6-cba-dsRed 3 days post transduction. Scale bar = 1 mm. (B) Quantification of average pixel intensity of mEHT images 3 days post transduction as a measure of dsRed expression. Each data point represents an individual mEHT. (C) Measured twitch forces of mEHTs before and after AAV6-cba-dsRed transduction (n = 4). No statistically significant differences between dosages were detected by a paired two-way ANOVA with Tukey's HSD test. (D) Representative cross-sectional images of dsRed-transduced mEHTs stained for α-actinin. Scale bars = 100 μm. (E) Area of mEHT cross-sections positively expressing dsRed (n = 2). Bars indicate statistical significance ($p < 0.05$) as measured by one-way ANOVA with Tukey's HSD test.

4.4.5 AAV-μDys expression in hiPSC-CMs

AAV vectors encoding μDys proteins have been used extensively in animal models and now in human clinical trials. However, μDys protein expression has not previously been demonstrated in hiPSC-CMs. DMD hiPSC-CMs were transduced with an AAV6 encoding μDys5 under a muscle-specific creatine kinase 8 (ck8e) promoter (AAV6-ck8e-μDys5) during replating at three dosages (MOI = 1×10^4, 1×10^5, and 5×10^5) [4]. In previous experiments, μDys5 expression was not observed 14 days after transduction (not shown), which is consistent with increased time to μDys expression observed in murine models. Further experiments demonstrated consistent, dose-dependent expression of AAV6-ck8e-μDys5 between 14- and 28-days post transduction (**Fig 4.4**). Of note, it appears that μDys5 protein expression exceeds the amount of full-length dystrophin expressed in the normal control.

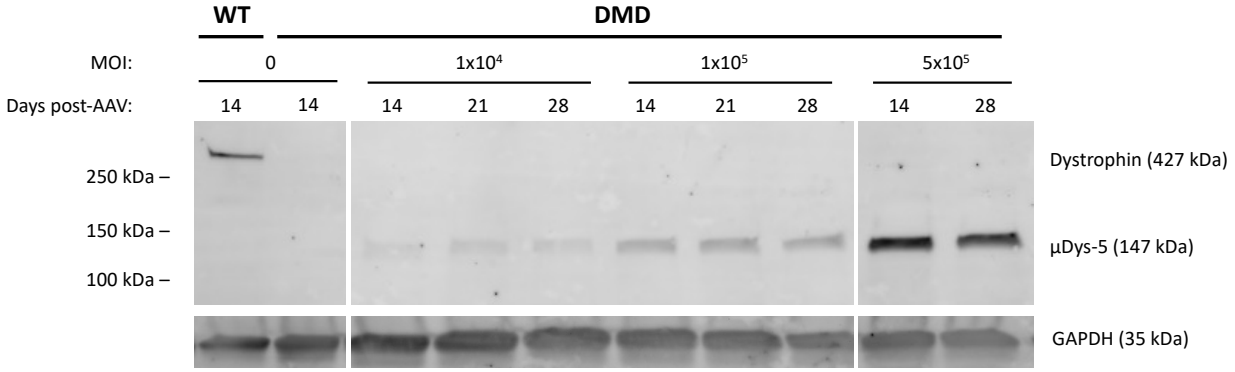

Figure 4.5. Expression of AAV-μDys in hiPSC-CMs. Western blot detecting full-length dystrophin (427 kDa) and μDys-5 (147 kDa) expressed by control (WT) or DMD hiPSCs after transduction of AAV6-ck8e-μDys5 at MOI = 0, 1×10^4, 1×10^5, and 5×10^5.

4.5 Discussion

Despite exciting advances in AAV-μDys gene therapies for the treatment of DMD and their demonstrated ability to rescue skeletal muscle function [4, 7–11], comparatively little is known of their cardioprotective effects, with some studies finding only partial rescue of cardiac function [10,

12, 13]. This is, in part, due to the lack of severe cardiac phenotypes presented by commonly used preclinical mouse models. To address this, we have developed a fully human, in 3D EHT in vitro model of dystrophic cardiomyopathy. In a previous study, we demonstrated that EHTs expressing a truncated dystrophin protein display several key phenotypes of DMD [17]. Here, we further developed a 96-well mEHT platform that is more suitable for higher throughput screening. Dystrophin-null mEHTs were shown to display a hypocontractile phenotype similar to our previous study. In the studies described herein, we validated the utility of this mEHT platform as a preclinical model for evaluation of AAV-μDys gene therapies.

Efficient transduction of hiPSC-CMs with AAV has been demonstrated previously and is currently being used extensively due to its high efficiency and relatively low toxicity [27]. In keeping with prior studies, here we demonstrated efficient and dose-dependent expression of fluorescent reporter dsRed and μDys5 delivered to hiPSC-CMs by AAV6. And while systemic AAV administration is performed clinically, AAV gene delivery to intact, beating engineered cardiac tissues had not yet been demonstrated, as previous studies have only transduced cardiomyocytes before generating EHTs or have added AAV to the cell mixture while casting EHTs [28, 29]. Here, we found that intact, beating mEHTs were easily transduced with AAV-cba-dsRed with MOI as low as 1×10^4. We hypothesize that this enhanced efficiency as compared to prior studies is due to the smaller size of the 96-well mEHTs with allows for easier diffusion throughout the tissue volume as well as the proximity of the mEHTs to the bottom of the tissue culture dish, which allows for the vector to be concentrated in 100 μL for the first 24 hours following transduction. This administration scheme improves the comparison of treated and untreated controls while also allowing for the observation of functional rescue following transgene delivery. Ultimately, this advancement further improves the utility of mEHTs as a preclinical testing platform in the gene therapy space.

Of the newly emerging DMD treatments, AAV-μDys gene replacement therapy is of great interest for its ability to restore expression of a miniaturized, yet functional, dystrophin protein, regardless of the patient's underlying mutation. At the time of this writing, there are three active AAV-μDys human clinical trials underway in the United States (Pfizer ClinicalTrials.gov identifier NCT03362502, Sarepta Therapeutics NCT03375164, and Solid Biosciences NCT03368742), each of which is using a distinct combination of AAV capsid, promoter, and μDys vector [30]. Interim data suggests that Sarepta's higher dose of SRP-9001 has yielded higher efficiencies with 81% of muscle fibers being positive for μDys, resulting in improved ambulation and reduction of serum creatine kinase [31]. While Sarepta failed to meet motor function clinical endpoints in phase 2 trials, phase 3 studies have reported significant improvements in North Star Ambulatory Assessment (NSAA) scores. Meanwhile, Pfizer has reported similar efficiencies (40-70% fiber positivity) and expression (25-30% endogenous expression) with PF-06939926, and also reported improvements in NSAA scores [32]. Solid Biosciences achieved 10-70% fiber positivity and 5-17.5% of normal dystrophin expression with their lower initial dosage, also with improvements in motor function [33]. Of note, none of these trials have yet assessed the effect of gene therapy treatment on cardiac function at these early time points.

Despite promising initial results, progress in these clinical trials has been challenged by severe adverse events (SAE), which have occurred in five patients, including one in the Sarepta trial and three in the Pfizer trial, one of which resulted in the death of a patient. Another clinical trial by Genethon in partnership with Sarepta (EudraCT Number: 2020-002093-27) was halted after a (SAE) occurred in a patient following administration of GNT-0004. Such SAEs are thought to occur due to a genotype-specific immune response to a specific region of the μDys protein, rather than to the AAV capsid or promoter or transgene sequence [34]. As a result, current studies have updated their eligibility criteria to exclude patients that put them at a higher risk of immune

response. In light of the severity of these events, it is clear that further optimization of μDys vectors is needed.

Here, we have made progress toward the use the mEHT platform for the evaluation of AAV-μDys gene therapy. We have demonstrated that hiPSC-CMs efficiently express AAV6-ck83-μDys5 and have demonstrated efficient in situ transduction of intact mEHTs. In this in vitro mEHT model with relevant output measures of cardiac function, we will be able to measure any rescue of contractile force occurring after AAV-μDys administration. Future studies will compare the newly developed AAVMYO capsid for its ability to provide enhanced transduction and expression of novel AAV serotypes as well as evaluate the cardioprotective effects of newly developed μDys designs. Ultimately, through these studies we will have demonstrated the suitability of engineered in vitro models for preclinical testing of gene therapies.

4.6 Conclusion

While AAV-μDys gene replacement therapy is currently being evaluated in three separate clinical trials, very little is known of the effect of μDys on cardiac function. Given the limited cardiac phenotype presented in the *mdx* mouse, we developed an in vitro 3D hiPSC-CM model of DMD for preclinical screening. The resulting 96-well mEHT platform uses significantly fewer cells and reagents than larger comparable platforms, increasing the statistical power of screening studies. We demonstrated that DMD mEHTs recapitulate previously observed phenotypes and achieved successful, dose-dependent AAV transduction of intact, beating mEHTs. Future studies will use the DMD mEHT platform to evaluate the efficacy of novel AAV serotypes as well as the effect of novel μDys vectors. The studies described herein are the first to examine the function of μDys in hiPSC-CMs as well as mEHTs, demonstrating its utility as a preclinical model of DMD.

4.7 References

1. Chamberlain JR, Chamberlain JS (2017) Progress toward Gene Therapy for Duchenne Muscular Dystrophy. Mol Ther 25:1125–1131

2. Elangkovan N, Dickson G (2021) Gene Therapy for Duchenne Muscular Dystrophy. J Neuromuscul Dis 8:S303–S316. https://doi.org/10.3233/JND-210678

3. Weinmann J, Weis S, Sippel J, et al (2020) Identification of a myotropic AAV by massively parallel in vivo evaluation of barcoded capsid variants. Nat Commun 11:5432. https://doi.org/10.1038/s41467-020-19230-w

4. Ramos JN, Hollinger K, Bengtsson NE, et al (2019) Development of Novel Micro-dystrophins with Enhanced Functionality. Mol Ther 27:623–635. https://doi.org/10.1016/j.ymthe.2019.01.002

5. McGreevy JW, Hakim CH, McIntosh MA, Duan D (2015) Animal models of Duchenne muscular dystrophy: from basic mechanisms to gene therapy. Dis Model Mech 8:195–213. https://doi.org/10.1242/dmm.018424

6. Pastoret C, Sebille A (1995) mdx mice show progressive weakness and muscle deterioration with age. J Neurol Sci 129:97–105. https://doi.org/10.1016/0022-510X(94)00276-T

7. Wang B, Li J, Xiao X (2000) Adeno-associated virus vector carrying human minidystrophin genes effectively ameliorates muscular dystrophy in mdx mouse model. Proc Natl Acad Sci 97:13714–13719. https://doi.org/10.1073/pnas.240335297

8. Yuasa K, Miyagoe Y, Yamamoto K, et al (1998) Effective restoration of dystrophin-associated proteins in vivo by adenovirus-mediated transfer of truncated dystrophin cDNAs. FEBS Lett 425:329–336. https://doi.org/10.1016/S0014-5793(98)00251-8

9. Sakamoto M, Yuasa K, Yoshimura M, et al (2002) Micro-dystrophin cDNA ameliorates dystrophic phenotypes when introduced into mdx mice as a transgene. Biochem Biophys Res Commun 293:1265–1272. https://doi.org/10.1016/S0006-291X(02)00362-5

10. Gregorevic P, Allen JM, Minami E, et al (2006) rAAV6-microdystrophin preserves muscle function and extends lifespan in severely dystrophic mice. Nat Med 12:787–789. https://doi.org/10.1038/nm1439

11. Hakim CH, Wasala NB, Pan X, et al (2017) A Five-Repeat Micro-Dystrophin Gene Ameliorated Dystrophic Phenotype in the Severe DBA/2J-mdx Model of Duchenne Muscular Dystrophy. Mol Ther - Methods Clin Dev 6:216–230. https://doi.org/10.1016/J.OMTM.2017.06.006

12. Townsend DW, Blankinship MJ, Allen JM, et al (2007) Systemic administration of micro-dystrophin restores cardiac geometry and prevents dobutamine-induced cardiac pump failure. Mol Ther 15:1086–1092. https://doi.org/10.1038/sj.mt.6300144

13. Bostick B, Yue Y, Long C, et al (2009) Cardiac expression of a mini-dystrophin that normalizes skeletal muscle force only partially restores heart function in aged Mdx mice. Mol Ther 17:253–261. https://doi.org/10.1038/mt.2008.264

14. Larcher T, Lafoux A, Tesson L, et al (2014) Characterization of Dystrophin Deficient Rats: A New Model for Duchenne Muscular Dystrophy. PLoS One 9:e110371. https://doi.org/10.1371/journal.pone.0110371

15. Yu X, Bao B, Echigoya Y, Yokota T (2015) Dystrophin-deficient large animal models: translational research and exon skipping. Am J Transl Res 7:1314–31

16. Pioner JM, Fornaro A, Coppini R, et al (2020) Advances in Stem Cell Modeling of Dystrophin-Associated Disease : Implications for the Wider World of Dilated Cardiomyopathy. Front Physiol 11:368. https://doi.org/10.3389/fphys.2020.00368

17. Bremner SB, Mandrycky CJ, Leonard A, et al (2022) Full-length dystrophin deficiency leads to contractile and calcium transient defects in human engineered heart tissues. J Tissue Eng 13:1–16. https://doi.org/10.1177/20417314221119628

18. Guan X, Mack DL, Moreno CM, et al (2014) Dystrophin-deficient cardiomyocytes derived from human urine: New biologic reagents for drug discovery. Stem Cell Res 12:467–480. https://doi.org/10.1016/j.scr.2013.12.004

19. Smith AS, Luttrell SM, Dupont J-B, et al (2022) High-throughput, real-time monitoring of engineered skeletal muscle function using magnetic sensing. J Tissue Eng 13:. https://doi.org/10.1177/20417314221122127

20. Leonard A, Bertero A, Powers JD, et al (2018) Afterload promotes maturation of human induced pluripotent stem cell derived cardiomyocytes in engineered heart tissues. J Mol Cell Cardiol 118:147–158. https://doi.org/10.1016/j.yjmcc.2018.03.016

21. Bielawski KS, Leonard A, Bhandari S, et al (2016) Real-rime force and frequency analysis of engineered human heart tissue derived from induced pluripotent stem cells using magnetic sensing. Tissue Eng Part C 22:932–940. https://doi.org/10.1089/ten.tec.2016.0257

22. Sniadecki NJ, Chen CS (2007) Microfabricated Silicone Elastomeric Post Arrays for Measuring Traction Forces of Adherent Cells. Methods Cell Biol 83:313–328. https://doi.org/10.1016/S0091-679X(07)83013-5

23. Bremner SB, Goldstein AJ, Higashi T, Sniadecki NJ (2022) Engineered Heart Tissues for Contractile, Structural, and Transcriptional Assessment of Human Pluripotent Stem Cell-Derived Cardiomyocytes in a Three-Dimensional, Auxotonic Environment. In: Coulombe KLK, Black LD (eds) Cardiac Tissue Engineering: Methods and Protocols, 2nd ed. Springer US, New York, NY, United States

24. Rodriguez AG, Han SJ, Regnier M, Sniadecki NJ (2011) Substrate stiffness increases twitch power of neonatal cardiomyocytes in correlation with changes in myofibril structure and intracellular calcium. Biophys J 101:2455–2464. https://doi.org/10.1016/j.bpj.2011.09.057

25. Flanigan KM, Dunn DM, von Niederhausern A, et al (2009) Mutational Spectrum of DMD Mutations in Dystrophinopathy Patients: Application of Modern Diagnostic Techniques to a Large Cohort. Hum Mutat 30:1657–1666. https://doi.org/10.1002/humu.21114

26. Guan X, Wang Z, Czerniecki S, et al (2015) Use of Adeno-Associated Virus to Enrich Cardiomyocytes Derived from Human Stem Cells. Hum Gene Ther Clin Dev 26:194–201. https://doi.org/10.1089/humc.2015.052

27. Rapti K, Stillitano F, Karakikes I, et al (2015) Effectiveness of gene delivery systems for pluripotent and differentiated cells. Mol Ther - Methods Clin Dev 2:14067. https://doi.org/10.1038/mtm.2014.67

28. Saleem U, Mannhardt I, Braren I, et al (2020) Force and Calcium Transients Analysis in Human Engineered Heart Tissues Reveals Positive Force-Frequency Relation at Physiological Frequency. Stem Cell Reports 14:312–324. https://doi.org/10.1016/j.stemcr.2019.12.011

29. Dutsch A, Wijnker PJM, Schlossarek S, et al (2019) Phosphomimetic cardiac myosin-binding protein C partially rescues a cardiomyopathy phenotype in murine engineered heart tissue. Sci Reports 2019 91 9:1–12. https://doi.org/10.1038/s41598-019-54665-2

30. Crudele JM, Chamberlain JS (2019) AAV-based gene therapies for the muscular dystrophies. Hum Mol Genet 28:R102–R107

31. Zaidman C, Proud C, McDonald C, et al (2021) EP.152 ENDEAVOR: a gene delivery study to evaluate the safety of and expression from SRP-9001 in Duchenne muscular dystrophy.

Neuromuscul Disord 31:S95. https://doi.org/10.1016/j.nmd.2021.07.177

32. Moorehead T (2018) Pfizer PF-06939926: Gene therapy safety and tolerability study in Duchenne Muscular Dystrophy (DMD). In: Parent Project Muscular Dystrophy Annual Conference

33. Rao V, Byrne B, Shieh P, et al (2021) O.2 IGNITE DMD Phase I/II ascending dose study of SGT-001 microdystrophin gene therapy for DMD: 1.5-year functional outcomes update. Neuromuscul Disord 31:S47. https://doi.org/10.1016/j.nmd.2021.07.019

34. Bonnemann CG, Belluscio BA, Braun S, et al (2022) A Collaborative Analysis by Clinical Trial Sponsors and Academic Experts of Anti-transgene SAEs in Studies of Gene Therapy for DMD [abstract]. In: ASGCT Annual Meeting

Chapter 5. Conclusions and Future Directions

The mechanisms underlying cardiac disease progression in DMD are poorly understood, despite the prevalence of cardiomyopathy as the leading cause of death. This has complicated the development of novel treatments for DMD such as microdystrophin gene replacement therapy, where the pool of potential treatment designs is increasingly large and previous studies have failed to adequately translate from preclinical studies to human patients. In no small part, this is due to the shortcomings of animal models used to study DMD, which present only mild cardiac phenotypes and lack relevant human physiology. To address this, many have turned to hiPSC-CMs as an in vitro platform with which to study cardiomyocyte-autonomous mechanisms of DMD progression. However, two-dimensional cell culture platforms are limited by fetal immaturity, which often obscures disease phenotypes. Thus, there remains a need for three-dimensional in vitro models of dystrophic cardiomyopathy to promote more physiological cell maturation and provide relevant functional output measures in order to recapitulate DMD pathology and better understand how the absence of full-length dystrophin affects tissue-level function.

In the work described herein, we have developed EHTs from hiPSC-CMs expressing a truncating dystrophin mutation as a preclinical platform for disease modeling, as described in Chapter 3. We observed that dystrophic EHTs produced lower contractile forces as compared to normal controls. These contractile deficiencies also included slower contraction kinetics. At the sarcomere level, this shortcoming was partially explained by shorter sarcomeres in dystrophic EHTs. In this platform we captured elevated Ca^{2+} levels and slowed Ca^{2+} transient kinetics for the first time in a three-dimensional in vitro model of DMD. Transcriptomic analysis EHTs revealed the dysregulation of multiple disease-relevant biological processes, including heart development, regulation of membrane potential, and Ca^{2+} homeostasis. This work was the first to fully describe

the dystrophic phenotype presented in a 3D in vitro model, demonstrating its utility as a preclinical drug screening and validation platform.

Following these successful initial studies, we were uniquely positioned to demonstrate the preclinical relevance of this EHT platform. Gene therapies utilizing AAV-delivered microdystrophins have proven successful in numerous animal studies and initial clinical trials. However, the overwhelming number of possible AAV capsid serotypes and μDys designs necessitate the development of improved in vitro preclinical models. As described in Chapter 4, we developed a smaller, 96-well mEHT platform suitable for higher throughput screening of novel gene therapy vectors. Using this platform, we demonstrated efficient transduction of intact, contracting mEHTs with AAV vectors, which had not been achieved previously. Future studies will use the mEHT platform to evaluate the ability of novel μDys vectors to rescue dystrophic mEHT function. The goal remains the same—to provide an mEHTs platform as an intermediary between high-throughput in vitro screening studies and preclinical studies in animal models.

This research provides a valuable jumping off point from which further innovations in in vitro DMD disease modeling can begin. While the EHT platform described allows for the assessment of cardiomyocyte-autonomous function as a cause of disease, a critical aspect of dystrophic cardiomyopathy that is missing from this model is fibrosis. At the organ level, excessive fibrosis in response to muscle degradation contributes significantly to both cardiac and skeletal muscle pathology [1]. As the cardiac DMD disease phenotype progresses, fibrosis contributes to electrical conduction abnormalities and arrythmias and to the decline in systolic and diastolic function as cardiac remodeling occurs. As fibrosis contributes to cardiac disease at large, there have been engineered cardiac tissue models that claim to elicit a fibrotic response in vitro, but these have mostly used suboptimal cardiac fibroblasts and required delivery of exogenous cues such as transforming growth factor beta (TGF-β) or known cardiotoxins [2–5]. Ultimately, it is likely that hiPSC-derived cardiac fibroblasts will be needed, and initial studies have demonstrated some

success in the development of differentiation protocols [6–8]. The development of dystrophic EHTs made from hiPSC-derived cardiomyocytes and cardiac fibroblasts would enable us to answer a variety of research questions crucial to advance our understanding of DMD. Specifically, we could evaluate whether dystrophic cues from hiPSC-CMs alone are sufficient to trigger a fibrotic response and whether the underlying genotype of cardiac fibroblasts affects their response to a dystrophic environment. Additionally, such a platform could be used to assess the contribution of fibrosis to cardiac disease progression and determine whether preventing fibrosis could slow disease progression. Ultimately, such developments will greatly advance the scientific and predictive power of our in vitro disease models.

Another aspect of cardiac tissue that is missing from the described EHT model is vascularization. Generating sufficient vascularization has proven to be one of the greatest challenges in engineering tissues on a larger scale, but many groups have explored various patterning techniques and endothelial cell-directed angiogenesis to recapitulate native vascular systems in vitro [9–13]. Future studies able to add vascularization to EHTs would provide the opportunity to capture key aspects of DMD pathology and treatment, including vasoconstriction and gene therapy delivery via systemic infusion.

Lastly, while this work has focused on cardiac muscle as the area most lacking suitable disease models, the advancement of skeletal muscle tissue engineering can also be applied to generate fully human in vitro models of dystrophic skeletal muscle. Multiple groups have described protocols for the generation of skeletal myotubes from hiPSCs [14–17]. These cells have previously been combined with various three-dimensional culture techniques to generate engineered skeletal muscle [18]. However, many of these platforms are technically challenging and are limited by low throughput. More recently, we have developed a high-throughput engineered skeletal model inspired by the EHT platform [17]. This platform uses previously developed magnetic tracking technology to provide real-time, longitudinal assessment of

engineered muscle function [19]. This model was used to capture a dystrophic phenotype in vitro, as it was shown that engineered muscle from dystrophin-null hiPSCs generated reduced twitch and tetanic contraction forces and altered kinetics [17]. Ultimately, this work is an exciting jumping off point from which we can further understand dystrophic myopathy and evaluate the effect of novel therapeutics on skeletal muscle function in the dish.

As we race toward new and innovative therapies for DMD, it warrants a discussion on who is most likely to benefit from these advances in care. Given the X-linked recessive nature of the disease, DMD affects males with female carriers being asymptomatic. However, it is known that some female carriers do manifest symptoms as a result of X-chromosome inactivation [20, 21]. Currently, our understanding of the pathology and treatment of DMD is skewed exclusively toward male patients, and thus, more research in to DMD carrier muscular dystrophy is needed. As roughly two-thirds of DMD cases are inherited, different rates of disease and types of mutations occur in different populations. Globally, studies have found significant regional differences in disease genotype [22, 23]. Additionally, in 2007, it was found that in the United States, prevalence among Hispanic individuals is highest at 1.53 per 10,000, compared to 1.45 for non-Hispanic white individuals and 0.63 for Black individuals [24]. In the development of mutation-specific treatments such as stop codon read-though and exon skipping therapy, it is the responsibility of researchers and drug developers to consider the genotypes prioritized and which populations they are more likely to benefit. Currently, diagnosis of DMD and access to treatment varies significantly by race. It was found that Black and Hispanic patients were more likely to be older at initial evaluation and diagnosis compared to white patients, even when familial history of DMD was controlled [25]. This delay in diagnosis thus causes a delay at initiation of treatment, which is detrimental as early intervention is critical to minimize muscle loss. As a society and a medical profession, it is a failure if these patients continue to be left behind. Given the predicted high costs of gene repair and replacement therapies (up to $750,000 per year for exon skipping drugs), it is

critical to consider who will have first access to treatment, as it will likely not be equitable unless interventions are made.

Ultimately, the studies described in this work advance our ability to model human disease in a dish. Through this engineered cardiac model of DMD, we can deepen our understanding of the mechanisms underlying dystrophic cardiomyopathy and of how dysfunction at the cellular level manifests in organ-level failure in the absence of functional dystrophin protein. As this EHT platform provides relevant outputs of cardiac function, reproduces key phenotypes of DMD, and is amenable to AAV transduction, it holds great promise to increase the throughput and accuracy of preclinical testing, ultimately increasing the speed and confidence with which we can translate findings from the lab to the clinic.

5.1 References

1. Klingler W, Jurkat-Rott K, Lehmann-Horn F, Schleip R The role of fibrosis in Duchenne muscular dystrophy

2. Larcher T, Lafoux A, Tesson L, et al (2014) Characterization of Dystrophin Deficient Rats: A New Model for Duchenne Muscular Dystrophy. PLoS One 9:e110371. https://doi.org/10.1371/journal.pone.0110371

3. Wang EY, Rafatian N, Zhao Y, et al (2019) Biowire Model of Interstitial and Focal Cardiac Fibrosis. ACS Cent Sci 5:1146–1158. https://doi.org/10.1021/acscentsci.9b00052

4. Mastikhina O, Moon BU, Williams K, et al (2020) Human cardiac fibrosis-on-a-chip model recapitulates disease hallmarks and can serve as a platform for drug testing. Biomaterials 233:. https://doi.org/10.1016/j.biomaterials.2019.119741

5. Hossein Sadeghi A, Ryon Shin S, Deddens JC, et al (2017) Engineered Three-Dimensional

Cardiac Fibrotic Tissue to Study Fibrotic Remodeling HHS Public Access Author manuscript. 6:. https://doi.org/10.1002/adhm.201601434

6. Lee MO, Jung KB, Jo SJ, et al (2019) Modelling cardiac fibrosis using three-dimensional cardiac microtissues derived from human embryonic stem cells. J Biol Eng 13:1–17. https://doi.org/10.1186/s13036-019-0139-6

7. Zhang J, Tao R, Campbell KF, et al (2019) Functional cardiac fibroblasts derived from human pluripotent stem cells via second heart field progenitors. Nat Commun 10:1–15. https://doi.org/10.1038/s41467-019-09831-5

8. Zhang H, Tian L, Shen M, et al (2019) Generation of quiescent cardiac fibroblasts from human induced pluripotent stem cells for in vitro modeling of cardiac fibrosis. Circ Res 125:552–566. https://doi.org/10.1161/CIRCRESAHA.119.315491

9. Whitehead AJ, Hocker JD, Ren B, Engler AJ (2022) Improved epicardial cardiac fibroblast generation from iPSCs. J Mol Cell Cardiol 164:58–68. https://doi.org/10.1016/j.yjmcc.2021.11.011

10. Yang G, Mahadik B, Choi JY, Fisher JP (2020) Vascularization in tissue engineering: fundamentals and state-of-art. Prog Biomed Eng 2:012002. https://doi.org/10.1088/2516-1091/ab5637

11. Novosel EC, Kleinhans C, Kluger PJ (2011) Vascularization is the key challenge in tissue engineering. Adv Drug Deliv Rev 63:300–311

12. Williams MAC, Mair DB, Lee W, et al (2021) Engineering three-dimensional vascularized cardiac tissues. Tissue Eng Part B Rev. https://doi.org/10.1089/ten.teb.2020.0343

13. Osaki T, Sivathanu V, Kamm RD (2018) Vascularized microfluidic organ-chips for drug screening, disease models and tissue engineering. Curr Opin Biotechnol 52:116–123. https://doi.org/10.1016/J.COPBIO.2018.03.011

14. Lai BFL, Huyer LD, Lu RXZ, et al (2017) InVADE: Integrated vasculature for assessing dynamic events. Adv Funct Mater 27:1703524. https://doi.org/10.1002/adfm.201703524

15. Borchin B, Chen J, Barberi T (2013) Derivation and FACS-mediated purification of PAX3+/PAX7+ skeletal muscle precursors from human pluripotent stem cells. Stem Cell Reports 1:620–631. https://doi.org/10.1016/j.stemcr.2013.10.007

16. Chal J, Al Tanoury Z, Hestin M, et al (2016) Generation of human muscle fibers and satellite-like cells from human pluripotent stem cells in vitro. Nat Protoc 11:1833–1850. https://doi.org/10.1038/nprot.2016.110

17. Hicks MR, Hiserodt J, Paras K, et al (2018) ERBB3 and NGFR mark a distinct skeletal muscle progenitor cell in human development and hPSCs. Nat Cell Biol 20:46–57. https://doi.org/10.1038/s41556-017-0010-2

18. Kang MS, Lee SH, Park WJ, et al (2020) Advanced techniques for skeletal muscle tissue engineering and regeneration. Bioengineering 7:1–14

19. Smith AS, Luttrell SM, Dupont J-B, et al (2022) High-throughput, real-time monitoring of engineered skeletal muscle function using magnetic sensing. J Tissue Eng 13:. https://doi.org/10.1177/20417314221122127

20. Neri M, Rossi R, Trabanelli C, et al (2020) The Genetic Landscape of Dystrophin Mutations in Italy: A Nationwide Study. Front Genet 11:131. https://doi.org/10.3389/fgene.2020.00131

21. Selvatici R, Rossi R, Fortunato F, et al (2021) Ethnicity-related DMD Genotype Landscapes in European and Non-European Countries. Neurol Genet 7:e536. https://doi.org/10.1212/nxg.0000000000000536

22. Centers for Disease Control and Prevention (2009) Prevalence of Duchenne/Becker Muscular Dystrophy Among Males Aged 5-24 Years – Four States, 2007. MMWR 58:1119–

1122

23. Holtzer C, Meaney FJ, Andrews J, et al (2011) Disparities in the diagnostic process of Duchenne and Becker muscular dystrophy. Genet Med 13:942–947. https://doi.org/10.1097/GIM.0b013e31822623f1

Appendix – MATLAB analysis code

This section contains MATLAB analysis scripts and functions used for EHT analysis and quantifying immunohistochemistry images. The following was developed with extensive help from Alan Levinson at the University of Washington.

A.1 Dystrophin staining intensity

```
%% Fluorescence intensity quantification
% used to quantify fluorescence intensity of dystrophin-stained EHT sections

clear all; close all; clc;

% Set path to folder containing .lif files you'd like to process

% channel names, leave empty if n/a
cNames{1} = 'DAPI';
cNames{2} = 'dystrophin';
cNames{3} = 'A-actin';
cNames{4} = '';

% Name of channel to use as mask and to quantify with, only has to be a
% unique part of the channel name (ie. cannot be shared by other channel
% names). Case sensitive
mask_cName = 'dystrophin';

%Threshold used for binarizing images, use -1 for Otsu's method:
%th = -1;
BINthresh = .04706; %VAST difference between .04706 and anything less

%Threshold used to exclude any centroids with a pixel size smaller
areaThresh = 200; %500 for more selectivity

%File pattern (will find files with matching title)
pattern = 'image*'; % use * to include any strings containing the keywork (e.g. *.nd2,
*40x*_images*, etc)

%Output file names, the first will contain values for the intensities
%separated by file, and the second will contain values for the areas,
%WILL OVERWRITE SHEETS IN FILE WITH SAME NAME IF LEFT IN CURRENT FOLDER.
outputName = 'Output';
intensitySheetName = 'Intensity';
areaSheetName = 'Area';

%Specifies the number of pixels each white pixel will be dilated in the mask.
dilationAmount = 5;

%%% You shouldn't need to change anything below here
%%% ------------------------------------------------------------

%% Choose files
% https://matlab.fandom.com/wiki/FAQ#How_can_I_process_a_sequence_of_files.3F
% Specify the folder where the files live.
PathName = pwd;

% Get a list of all files in the folder with the desired file name pattern.
```

```
filePattern = fullfile(PathName, pattern); % Change to whatever pattern you need.
theFiles = dir(filePattern);

%Create cells with file names
baseFileName = strings(length(theFiles),1);
fullFileName = strings(length(theFiles),1);
for k = 1 : length(theFiles)
  baseFileName(k) = char(theFiles(k).name);
  fullFileName(k) = char(fullfile(PathName, baseFileName(k)));
end

%%
%Find channel that is being processed (dystrophin in this case)
mask_cIndex = find(contains(cNames,mask_cName),1);


for k = 1:length(theFiles)

    %Search for file and use bfopen to load in data from file.
    [~, file_name, file_ext] = fileparts(baseFileName(k,:));
    disp(['Running file ' num2str(k) '/' num2str(length(theFiles))])
    % load image
    if strcmp(file_ext,'.lif')
        % check to ensure bioformats plugin is installed
        if ~exist('bfopen','file')
            ScriptPath = mfilename('fullpath');
            try
                addpath([ScriptPath '/bfmatlab'])
            catch
                error('CANNOT OPEN FILE: Please ensure you have the bioformats
functions installed.')
            end

            if ~exist('bfopen','file')
                error('CANNOT OPEN FILE: Please ensure you have the bioformats
functions installed.')
            end
        end
        rawdata = bfopen(char(fullFileName(k)));
        numseries = size(rawdata,1); % gets the number of rows in rawdata = number of
images
        % rawdata{1,1} = image 1, rawdata{2,1} = image2, rawdata{3,1} = image 3
        % https://ww2.mathworks.cn/mat
        series1 = rawdata{1,1};
        nChannels = size(series1,1);
    else
        error('File selected is not .lif')
    end


    for j = 1:numseries
           series = rawdata{j};
           s = series(:,2);

           %Determines whether series contains 3 or 4 channels
           if find(cellfun(@(s) contains(s, "C=1/3"), s))
               channels = {0,0,0};

               %Picks out each channel
               c1 = find(cellfun(@(s) ~isempty(strfind(s, 'C=1/3')), s));
               c2 = find(cellfun(@(s) ~isempty(strfind(s, 'C=2/3')), s));
```

```
        c3 = find(cellfun(@(s) ~isempty(strfind(s, 'C=3/3')), s));

        z = length(c1);
        for l = 1:3 %iterates once for each channel to perform Z
        %projections on all of them, stores all channels in cell.
            currChan = series(eval("c"+l));
            currChanZProj = max(cat(z, currChan{:}), [], z);
            channels{1,l} = currChanZProj;
        end

        %Determines whether series contains 4 channels, does similar
        %process as 3 channel images.
    elseif find(cellfun(@(s) contains(s, 'C=1/4'), s))
        channels = {0,0,0,0};

        c1 = find(cellfun(@(s) ~isempty(strfind(s, 'C=1/4')), s));
        c2 = find(cellfun(@(s) ~isempty(strfind(s, 'C=2/4')), s));
        c3 = find(cellfun(@(s) ~isempty(strfind(s, 'C=3/4')), s));
        c4 = find(cellfun(@(s) ~isempty(strfind(s, 'C=4/4')), s));
        z = length(c1);
        for l = 1:4
            currChan = series(eval("c"+l));
            currChanZProj = max(cat(z, currChan{:}), [], z);
            channels{1,l} = currChanZProj;
        end
    end

%Stores a grayscale version of the max-Z channel of interest
%(dystrophin in this case)
imGray = channels{1,mask_cIndex};

%Binarizes the max-z channel of interest to create a mask
if BINthresh==-1
    BW = imbinarize(imGray);
else
    BW = imbinarize(imGray,BINthresh);
end

%Finds centroids and notes their areas and pixels where they occur.
s1{j} = regionprops(BW,'Centroid','Area','PixelList');


%Exlcludes centroids smaller than areaThresh pixels (noise).
areas{j} = cat(1,s1{j}.Area);
exclude{j} = find(areas{j}<areaThresh);
areas{j}(exclude{j})=nan;
centroids{j} = cat(1,s1{j}.Centroid);
centroids{j}(exclude{j},:) = nan;
pixels{j} = [];
for l = 1:length(exclude{j})
    pixels{j} = cat(1,pixels{j},s1{j}(exclude{j}(l)).PixelList);
end

%Removes excluded pixels from binarized max-Z image
for l = 1:length(pixels{1,j})
    BW(pixels{1,j}(l,2),pixels{1,j}(l,1)) = 0;
end

%Dilates and/or fills mask
SE = strel('disk',dilationAmount);
BW = imdilate(BW,SE);
```

```
        %BW = imfill(BW,'holes');
        areaBW{k,j} = sum(sum(BW));

        %Stores image and binarized image in cell
        maskIm{j} = {imGray,BW};

        %Stores mask areas into a cell
        maskArea{k,j} = [areaBW{1,j}];

        %Applies the mask to the grayscaled image, and displays the two
        %side by side.
        if maskArea{k,j} ~= 0
            figure(j);
            imshowpair(maskIm{1,j}{1,1},maskIm{1,j}{1,2},'montage');
            maskedIm = uint8(maskIm{1,j}{1,2}).*maskIm{1,j}{1,1};
            imshowpair(maskedIm,maskIm{1,j}{1,2},'montage');
            %Stores the average intensity of pixels that passed the
            %binarized threshhold.
            averageIntensity{k,j} = mean(nonzeros(maskedIm));
        else
            disp("Image: " + file_name + " has empty series #" + int2str(j));
        end
    end
end

%Creates desired output filename
outputName = outputName+".xlsx";

%Writes all intensity and mask area cell arrays to an output excel sheet
%on different sheets for each array.
filesCell = struct2cell(theFiles);
fileNames = filesCell(1,:);
writecell(fileNames,outputName,'Range','B1','Sheet',intensitySheetName,'WriteMode','ov
erwritesheet');
writecell(averageIntensity.',outputName,'Sheet',intensitySheetName,'Range','B2');
writecell(fileNames,outputName,'Sheet',areaSheetName,'Range','B1','WriteMode','overwri
tesheet');
writecell(maskArea.',outputName,'Sheet',areaSheetName,'Range','B2');

%Generates and applies row names for both sheets of the output excel sheet.
for eachSeries = 1:length(areas)
    rowNames(eachSeries,1)="Series"+eachSeries;
end
writematrix(rowNames,outputName,'Sheet',intensitySheetName,'Range','A2');
writematrix(rowNames,outputName,'Sheet',areaSheetName,'Range','A2');
```

A.2 Quantification of AAV-dsRed transduction

```
%% Used to quantify dsRed+ and alpha-actinin+ areas for transduction
% quantification
clear all ; close all ; %clc ;
PathName = pwd;
outputFilename = "aactOutput";
pattern = '*16bit*';%Pattern for what folders images are in
imName{1} = 'dsRed'; %Pattern for dsRed stain max-Z projections
imName{2} = 'hoescht'; %Pattern for nuclei stain max-Z projections
imName{3} = 'aact'; %Pattern for a-actinin stain max-Z projections
nucleiOverlapThresh = 0;%Minimum amount of nuclei overlap with dsRed
                        %any less overlap causes the cell not to be dsRed+
```

```
intensThresh = 1000; %Low intensity threshold to cut out any
                     %ambient light contamination
areaThresh = 100; %Area threshold for smallest allowable area
                  %Both nuclei and dsRed.
filePattern = fullfile(PathName, pattern);
theFiles = dir(filePattern);
baseFileName = strings(length(theFiles),1);
fullFileName = strings(length(theFiles),1);
for k = 1 : length(theFiles)
 baseFileName(k) = char(theFiles(k).name);
 fullFileName(k) = char(fullfile(PathName, baseFileName(k)));
end
for i = 1:length(baseFileName)
  disp([num2str(i) '/' num2str(length(baseFileName))])
  cd(baseFileName(i))
  theImages = dir(fullFileName(i));
  numFile1 = 0;
  numFile2 = 0;
  numFile3 = 0;
  for k = 1 : length(theImages)
    if contains(theImages(k).name,imName{1})
      numFile1 = numFile1+1;
      Stain1Names{numFile1} = theImages(k).name;
    elseif contains(theImages(k).name,imName{2})
      numFile2 = numFile2+1;
      Stain2Names{numFile2} = theImages(k).name;
    elseif contains(theImages(k).name,imName{3})
      numFile3 = numFile3+1;
      Stain3Names{numFile3} = theImages(k).name;
    end
  end
  for k = 1:length(Stain1Names)
        stain1 = Stain1Names{k};
        stain2 = Stain2Names{k};
        stain3 = Stain3Names{k};
        % load original images
        ims{1} = imread(stain1);
        ims{2} = imread(stain2);
        ims{3} = imread(stain3);

        % Segment images
        Seg{1} = cellSeg2(stain1,areaThresh);
        Seg{2} = cellSeg2(stain2,areaThresh);
        Seg{3} = cellSeg2(stain3,areaThresh);

        for j = 1:length(Seg)
            masks{j}=Seg{1,j}{3};
        end
        figure(1)
        masks{1} = masks{1}.*(ims{1}>intensThresh);
        imshowpair(masks{2},masks{1})
        title("Mask 1 vs Mask 2")

        masksum12 = masks{1}+masks{2};
        intersect12 = masksum12==2;
        nucArea = sum(sum(masks{2}));
        totalIntersect12 = sum(sum(intersect12))./nucArea;

        masksum13 = masks{1}+masks{3};
        intersect13 = masksum13==2;
        actArea = sum(sum(masks{3}));
```

```
        totalIntersect13 = sum(sum(intersect13))./actArea;

        figure(2)
        imshowpair(masks{1},masks{3})
        title("Mask 1 vs Mask 3")

        for j = 1:length(Seg)
            maskedIm{j} = uint16(masks{j}).*ims{j};
            averageIntensity{j} = mean(nonzeros(maskedIm{j}));
        end

        nucleiInfo = regionprops(masks{2},'PixelList');
        nucleiCount(i) = length(nucleiInfo); % # nuclei detected
        dsRedArea(i) = sum(sum(masks{1}))./numel(masks{1}); % # dsRed+ pixels/ # total
pixels
        if dsRedArea(i)>0.5
            dsRedArea(i)=0;
        end

        %Following loop calculates whether nuclei is within overlap threshold
        %and deletes it if not.
        redNuclei = masks{2};
        for k = 1:nucleiCount(i)
            nucPixels = nucleiInfo(k).PixelList;
            intersectPix = 0;
            dimPixel = size(nucPixels);
            nucPix2 = [];
            nucPix1 = [];
            for l = 1:dimPixel(1)
                if intersect12(nucPixels(l,2),nucPixels(l,1))==1
                    intersectPix = intersectPix+1;
                end
            end
            if intersectPix/length(nucPixels)<=nucleiOverlapThresh
                for m = 1:dimPixel(1)
                    redNuclei(nucPixels(m,2),nucPixels(m,1))=0;
                end
            end
        end
        figure(3)
        redCellProps = regionprops(redNuclei,'PixelList');
        %dsRed+ nuclei are pink, - nuclei are green
        imshowpair(masks{2}-redNuclei,redNuclei)
        TotalRedNuclei(i) = length(redCellProps);
        pseudoEfficiency(i) = TotalRedNuclei(i)/nucleiCount(i);
        bitmax = intmax(class(ims{1}));
        dsRedIntensity(i) = double(averageIntensity{1})/double(bitmax);
        aactRedOverlap(i) = totalIntersect13;
  end
  cd(PathName)
end
OUTPUT =
table(dsRedArea',dsRedIntensity',TotalRedNuclei',nucleiCount',pseudoEfficiency',...
      aactRedOverlap','VariableNames',["dsRed Area","dsRed Intensity", ...
      "Total dsRed+ Nuclei","Total Nuclei", "Pseudo-efficiency","a-Actinin dsRed
Overlap"])
save(outputFilename,'OUTPUT');
```

A.3 Cell Segmentation Function

```
function boundary = cellSeg2(image,areaThresh,threshold)
%CELLSEG Takes in an RGB or grayscale image and returns a 1x2 cell
%that contains the boundaries of significant cell regions, and the
%threshold used to binarize the image.
%   image     = RGB or grayscale image to process.
%   areaThresh= Minimum number of pixels an area can have without being
%               ignored.
%   threshold = Threshold to generate binarized mask that highlights
%               important cell regions, if -1, will open a GUI to
%               determine threshold manually. If missing, will autogenerate
%               a threshold using canny edge detection.

%Read and filter initial image (turns RGB to grayscale if RGB)
image = imread(image);
if(length(size(image))==3)
    I1 = image(:,:,1)+image(:,:,2)+image(:,:,3);
else
    I1 = image;
end
I1 = medfilt2(I1);

%% Determine threshold
%If missing, use sobel gradient edge detection.
if(~exist('threshold','var'))
    [~,threshold] = edge(I1,'sobel');
    threshold = threshold(1);
    gradientFactor = 4; %controls gradient over which threshold is
                        %fine tuned, may need to be changed for
                        %different stains, 4-10 works for DAPI
    [~,threshold] = edge(I1,'sobel',threshold * gradientFactor);
end

%If -1, manually determine using UI
if(threshold == -1)
    fig = figure
    sldr = uicontrol(fig,'Style','slider');
    sldr.Position = [100 70 200 30];
    sldr.Min = 0;
    sldr.Max = .2;
    btn = uicontrol(fig,'Style','togglebutton');
    btn.Position = [100,200, 100, 20];
    btn.Value = false;
    btn.String = "Done";
    while(btn.Value == false)
        figure(2);
        imshow(imbinarize(I1,sldr.Value),'Border','Tight')
    end
    threshold = sldr.Value;
end

if(~exist('areaThresh','var'))
    areaThresh = 50;
end
%% Generate boundary mask
I2 = imbinarize(I1,threshold);
%Ignores area less than areaThresh
I3 = bwareaopen(I2,areaThresh);
I4 = imdilate(I3,ones(3));
I5 = imerode(I4,ones(3));
```

```
I6 = imfill(I5,'holes');
I7 = medfilt2(I6,[5 5]);

perim = bwperim(I7);
figure(3)
imshowpair(image,perim);
boundary{1} = bwboundaries(I7);
boundary{2} = threshold;
boundary{3} = I7;
end
```